Development of a ZnO nanowire-array biosensor for the detection and quantification of immunoglobulins

by
Deon Pieter Neveling

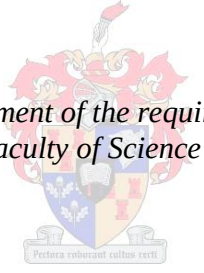

Thesis presented in fulfilment of the requirements for the degree of Master of Science in the Faculty of Science at Stellenbosch University

Supervisor: Prof L.M.T. Dicks
Co-supervisor: Prof W.J. Perold

December 2013

Declaration

By submitting this thesis electronically, I declare that the entirety of the work contained therein is my own, original work, that I am the sole author thereof (save to the extent explicitly otherwise stated), that reproduction and publication thereof by Stellenbosch University will not infringe any third party rights and that I have not previously in its entirety or in part submitted it for obtaining any qualification.

December 2013

Summary

The aim of this study was to develop a ZnO nanowire-array biosensor that would detect immunoglobulins and record changes in the concentration of an antibody. Early detection of disease-causing agents is essential for an early response. In contrast to conventional methods, biosensors may detect disease-associated agents much faster and more accurate, which holds specific benefits to rural communities. The development of such a biosensor would be favourable for diagnostics in underprivileged communities without infrastructure. The hypothesis was that binding of antibodies to the surface of ZnO nanowires would result in the generation of a piezoelectric potential that, when channelled through a Schottky barrier, would produce a constant voltage reading. Piezoelectricty would be generated due to the bending of the nanowires, or tensile stress applied to the nanowires due to binding of the antibodies. The performance of such a device largely depends on the methods used to construct the ZnO nanowires and methods used to funtionalize the sensor surface. The biggest challenge was thus to chemically modify the self-assembled monolayers (SAMs) and create intermediate monolayers that would react to primary amino groups of lysozyme and form a covalent amide bond. Lysozyme was selected as model antigen, since its structure and reaction with antibodies has been well studied.

Alkanethiol and dialkyl disulphides were used to form SAMs. Different SAMs were compared to select the absorbate that would bind the highest concentration of lysozyme. Lysozyme was best immobilized onto Au film layers in the presence of SAM 3-mercaptopropionic acid. Weakest immobilization was in the presence of combined SAM 11-mercaptoundecanoic acid/1-nonanethiol. The sensitivity of the constructed ZnO nanowire biosensor was tested *in vitro*, in the presence of different concentrations of lysozyme antibodies.

An increase in the dimension of the ZnO seed layer led to an increase in the mean diameter of the ZnO seed grains, and subsequently an increase in the mean diameter of the synthesized ZnO nanowires. Deposition of the ZnO seed layer, using the RF cylindrical magnetron sputtering technique, improved the c-axis alignment of the nanowires and produced nanowires with similar dimensions. However, deposition of the ZnO seed layer using the sol-gel spin coating technique, produced nanowires with irregular c-axis alignments

and irregular diameters. An increase in the Au film thickness led to a decrease in the mean diameter of the synthesized ZnO nanowires and worsening of the c-axis alignment. In contrast to single crystalline Au (111) film layers, polycrystalline Au layers increased the mean diameter of the synthesized nanowires. The crystal orientation of the Au film layer had no effect on the c-axis alignment.

Increased voltage readings were recorded with an increase in antibody binding, indicating that the ZnO nanosensor may be used to record changes in immunoglobulin levels. Antibody concentrations ranging from 10 ng/ml to 20 μg/ml were sensed.

This is the first study showing that ZnO nanowires, conformed into piezoelectric transducers, may be used in the detection of antibodies. The current size of the chip with ZnO nanowires is approximately 1 cm^2, which is too big to incorporate into a compact monitoring device. Apart from the challenge to produce smaller nanowire-arrays, highly sensitive sensors and miniature amplifiers will have to be developed to increase the strength of the signals generated by the nanowires. The biosensor will also have to be optimised to detect a variety of immunoglobulins.

Opsomming

Die doel van hierdie studie was om ‘n ZnO nanodraad biosensor te ontwikkel wat immunoglobuliene kan opspoor en veranderinge in konsentrasies van die teenliggaampies sal reflekteer. Vroë deteksie van siekte veroorsaakende agente is belangrik vir n vroeg tydige respons. In teenstelling tot konvensionele metodes, kan biosensors siekte veroorsaakende agente vining en akkuraat opspoor, wat veral voordele vir gemeenskappe in landelike gebiede inhou. Die hipotese was dat binding van teenliggaampies aan die ZnO nanodrade ‘n piëzo-elektriese potensiaal sal skep, wat dan ‘n konstante leesbare spanningspotensiaal sal lewer nadat dit deur ‘n Schottky versperring gestuur is. Piëzo-elektrisiteit word gegenereer deur die buiging van die nanodrade, of deur spanning wat op die nanodrade geplaas word deur binding van die teenliggaampies. Die sukses van die ontwerp hang grootliks af van die metode wat gebruik word om die ZnO nanodrade te konstrueer en metodes wat gebruik word om die sensor oppervlak te funksionaliseer. Die grootste uitdaging was dus om die monolae wat outomaties saam groepeer (SAMs) chemies so te verander dat intermediêre monolae vorm wat aan primêre aminogroepe van lisosiem bind ten einde kovalente amied-bindings te vorm. Lisosiem is as model antigeen geselekteer omdat die struktuur en reaksie daarvan met teenliggaampies reeds goed bestudeer is.

Alkaantiol en di-alkiel disulfied is gebruik om SAMs te vorm. ‘n Verskeidenheid SAMs is vergelyk ten einde die anker te selekteer waaraan die hoogste konsentrasie lisosiem sal bind. Lisosiem is die effektiefste aan Au film lae ge-immobiliseer in die teenwoordigheid van SAM 3-merkapto-propanoësuur. Die swakste immobilisasie is in die teenwoordigheid van kombineerde SAM 11-merkapto-dekanoësuur/1-nanotiol waargeneem. Die sensitiwiteit van die ZnO nanodrade is *in vitro* getoets, in die teenwoordigheid van verskillende konsentrasies van lisosiem teenliggaampies.

‘n Toename in die dimensie van die ZnO grondlaag het die gemiddelde deursnit van die ZnO grein verhoog en so ook die gemiddelde deursnit van die gesintetiseerde ZnO nanodrade. Toediening van die ZnO grondlaag deur gebruik te maak van die RF silindriese mikrogolf-verstuiwings tegniek het die orientasie van die c-aslyn van die nanodrade verbeter. Toediening met die sol-gel draai-bedekkings tegniek het ‘n onreëlmatige orientasie van die c-aslyn teweeg gebring, asook ‘n variasie in die afmetings van die nanodrade. ‘n Toename in

die Au laag het ‘n afname in die gemiddelde afmetings van die nanodrade en ook ‘n onreelmatige oriëntasie van die c-aslyn veroorsaak. In teenstelling met enkel-kristallyne Au (111) het poli-kristallyne Au lagies ‘n toename in die gemiddelde deursnit van die nanodrade veroorsaak. Die kristal-oriëntasie van die Au laag het geen effek op die belyning van die nanodrade gehad nie.

Die spanningspotensiaal het verhoog met ‘n toename in teenliggaampie binding. Hiervolgens kan die ZnO nanosensor gebruik word om veranderinge in immunoglobulien vlakke te monitor. Teenliggaampie konsentrasies wat wissel van 10 ng/ml tot 20 µg/ml is opgespoor.

Hierdie is die eerste studie wat toon dat ZnO nanodrade, omskep tot piëzo-elektriese transduseerders, gebruik kan word in die opsporing van teenliggaampies. Die grootte van die skyfie met die ZnO nanodrade is tans ongeveer 1 cm^2 en is te groot om in ‘n kompakte biosensor in te bou. Benewens die uitdaging om kleiner nanodraad skyfies te ontwikkel, sal hoogs sensitiewe sensors en seinversterkers ontwikkel moet word om die sein afkomstig van die nanodrade te versterk. Die biosensor sal ook ge-optimiseer moet word om ‘n verskeidenheid immunoglobuliene op te spoor.

Biographical sketch

Deon Pieter Neveling was born in Durban, South Africa, on the 14th of November, 1988. He matriculated at Port Natal High School, South Africa, in 2006. In 2007 he enrolled as B.Sc. student in Molecular Biology and Biotechnology at the University of Stellenbosch and obtained the degree in 2009. In 2011 he obtained his B.Sc (Hons) degree in Microbiology at the University of Stellenbosch. In January 2012 he enrolled as M.Sc. student in Microbiology.

Preface

All chapters have been written according to the instructions for the journal of Biosensors and Bioelectronics.

Acknowledgements

I sincerely would like to thank:

Prof. L.M.T. Dicks (Department of Microbiology, University of Stellenbosch) for giving me the opportunity to be part of his research group and for all the support and guidance.

Dr. Carol van Reenen (Department of Microbiology, University of Stellenbosch) for her valuable advice and support.

Stanley van der Heever (Department of Electric and Electronic Engineering, Stellenbosch University) for sharing his insight into ZnO nanowire synthesis and electronics.

Prof. Willie Perold (Department of Electric and Electronic Engineering, Stellenbosch University) for his insight into ZnO nanowire synthesis, and giving me the opportunity to perform some of the experiments in his laboratory.

Prof. Basil Julies (Department of Physics, University of the Western Cape), for use of the sputter coater.

Dr. Remy Bucher (Materials Research Division, iThemba LABs), for sharing his insight in crystallography and XRD analysis.

Dr. Miranda Waldron (Department of Astronomy; University of Cape Town) for sharing her insight into SEM analysis.

Contents

CHAPTER 1

Introduction

Introduction

Bacterial and viral infections are responsible for millions of deaths and non-fatal infections world-wide. Rapid detection and accurate identification of microbial cells, antigens, metabolic compounds, nucleic acids, proteins and antibodies are important in making the correct diagnosis. This is, however, difficult to achieve in third-world countries with little or no infrastructure. Many scientists are of the opinion that nano biosensors may provide a rapid and cost-effective alternative to current diagnostic techniques. Developing a portable and self-powered biosensor would improve the health of millions of people in underprivileged communities, especially in rural areas with a lack of infrastructure and electricity.

Most biosensors have a biologically active molecule in direct contact with a transducer element, sensitive enough to detect changes in concentration, or activity, of other biomolecules they interact with (Strehlitz et al., 2008). The utilization of zinc oxide nanostructures as transducers for biosensors are one of the most promising materials for their development (Ahmad and Zhu, 2011). Zinc oxide nanostructures have several advantages over other nanostrucutures (i.e. graphite, carbon, gold), which includes the presence of polar surfaces and the lack of centre symmetry (Wang, 2008). The interaction of polar surfaces makes the growth of diverse ZnO nanostructures possible (Wang et al., 2004), whereas the lack of centre symmetry provides ZnO with piezoelectric properties (Wang, 2007 and 2008).

Numerous factors need to be taken into account when synthesizing ZnO nanowires. Performance of the biosensors is improved by growing highly-oriented ZnO nanowires with identical dimensions (Song and Lim, 2007). It is thus important to control the growth, orientation, position and size of the ZnO nanowires to increase the sensitivity and reproducibility of the biosensor (Liu et al., 2008). The most challenging step in the construction of a biosensor is the immobilization of biomolecules close to the surface of the nanowires without losing biological activity (Fransconi et al., 2010; Gooding and Hibbert, 1999; Rusmini et al., 2007; Wong et al., 2009). Immobilized denatured proteins, for instance, lowers the sensitivity of a biosensor.

In this study, a nanoforce ZnO nanowire-array biosensor was developed to detect immunoglobulins. ZnO nanowire-arrays were synthesized by using the hydrothermal growth method. The RF cylindrical magnetron sputtering and sol-gel spin coating methods were

compared to determine which deposition technique resulted in nanowires with the best c-axis orientation and similar dimensions. The effect of an Au film layer, thickness and crystal orientation, on the growth of ZnO nanowires were also determined. Deposited ZnO seed layers were characterized by atomic force microscopy (AFM) and ellipsometry. Synthesized ZnO nanowires were characterized by scanning electron microscopy (SEM), energy dispersive spectroscopy (EDS), transmission electron microscopy (TEM) and X-ray diffraction (XRD).

Immobilization of lysozyme onto Au films was accomplished by using self-assembled monolayers (SAMs). The SAMs were chemically modified to create intermediate monolayers that would react to primary amino groups of proteins. Different SAMs were tested to identify the absorbate that would support the highest concentration of immobilized lysozyme. Alkanethiol and dialkyl disulphides were used to form SAMs. The SAMs and their chemical modifications were studied by AFM and fourier-transform infrared (FTIR) spectroscopy. Immobilized lysozyme was studied by AFM, FTIR spectroscopy, fluorescence microscopy and BacLight^{TM}, a staining technique that differentiates between viable and dead cells.

Construction of the nanoforce sensor was studied by AFM, SEM, TEM, and XRD. Immobilization of lysozyme to the sensor surface was characterized by AFM, FTIR spectroscopy, and fluorescence microscopy. *In vitro* tests were conducted to determine whether different concentrations of antibody binding would produce different voltage readings. In theory, increased binding of antibodies to the surface of the biosensor would disturb the ZnO molecules in the nanowires. These disturbances displace Zn^{2+} and O^{2-} in the ZnO crystal, resulting in the generation of piezoelectricity. This piezoelectric potential when channelled through a Schottky barrier produces a voltage.

References

Ahmad, M., Zhu, J., 2011. ZnO based advanced functional nanostructures: synthesis, properties and applications. J. Mater. Chem. 21, 599-614.

Fransconi, M., Mazzei, F., Ferri, T., 2010. Protein immobilization at gold-thiol surfaces and potential for biosensing. Anal. Bioanal. Chem. 398(4), 1545-1564.

Gooding, J.J., Hibbert, D.B., 1999. The application of alkanethiol self-assembled monolayers to enzyme electrodes. Trends in Analytical Chem. 18(8), 525-533.

Liu, J., Fei, P., Zhou, J., Tummala, R., Wang, Z.L., 2008. Toward high output-power nanogenerator. Appl. Phys. Lett. 92(17), 173105.

Rusmini, F., Zhong, Z., Feijen, J., 2007. Protein immobilization strategies for protein biochips. Biomacromoleucles 8(6), 1775-1789.

Song, J., Lim, S., 2007. Effect of seed layer on the growth of ZnO nanorods. J. Phys. Chem. C 111(2), 596-600.

Strehlitz, B., Nikolaus, N., Stoltenburg, R., 2008. Protein detection with aptamer biosensors. Sensors 8, 4296-4307.

Wang, Z.L., 2007. Oxide nanobelts and nanowires-growth, properties and applications. J. Nanosci. Nanotechnol. 8, 27-55.

Wang, Z.L., 2008. Towards self-powered nanosystems: from nanogenerators to nanopiezotronics. Adv. Funct. Mater. 18, 3553-3567.

Wang, Z.L., Kong, X.Y., Ding, Y., Gao, P., Hughes, W.L., Yang, R., Zhang, Y., 2004. Semiconducting and piezoelectric oxide nanostructures induced by polar surfaces. Adv. Funct. Mater. 14, 943-956.

Wong, L.S., Khan, F., Mickfield, J., 2009. Selective covalent protein immobilization: strategies and applications. Chem. Rev. 109(9), 4025-4053.

CHAPTER 2

Literature review

Literature review

1. Introduction

Research on nanostructures gained considerable interest over the past decade, mostly due to the demand for smaller components in electrical, mechanical and optical devices (Baruah and Dutta, 2009). Nanostructures are incorporated in a number of electronic, optical and photonic equipment (Ahmad and Zhu, 2011; Arya et al., 2012; Wei et al., 2011). Biosensors are nanosensors used in mechanical, electrical and optical devices in which a biologically active molecule is directly attached to the sensor that is in contact with a highly sensitive transducer element (Strehlitz et al., 2008). The nanosensor has to be sensitive enough to detect changes in the activity or concentration of molecules. Most of the research on biosensors focussed on increasing the sensitivity through the incorporation of unique nano-material (Ansari et al., 2008; Hrapovic et al., 2004; Lin et al., 2004; Rout et al., 2006; Wang et al., 2008; Zhang et al., 2008).

Several methods have been designed to synthesise ZnO nanostructures. These include vapour-liquid-solid (VLS) growth, with the use of a catalyst (Huang et al., 2001b); pulsed laser deposition (Choi et al., 2001); electrochemical deposition in porous membranes (Liu et al., 2003); metal vapour transport, using Zn sources (Lyu et al., 2002); physical vapour transport, using ZnO and graphite powder (Yao et al., 2002); chemical vapour deposition, using zinc acetylacetonate hydrate (Wu and Liu, 2002); metal organic chemical vapour deposition, using diethylzinc and O_2/N_2O as precursor (Kim et al., 2003); and hydrothermal growth (Vayssiers et al., 2001). Of all these methods, hydrothermal growth is used the most on industrial scale (Yousefi and Zak, 2011). Special care should be taken to grow highly oriented ZnO nanowires. This increases the surface per unit area of the biosensor and improves the overall performance (Song and Lim, 2007).

The most challenging part in developing a biosensor is controlling the growth of the nanostructures and immobilizing the biomolecules to the sensor surface without losing biological activity (Fransconi et al., 2010; Gooding and Hibbert, 1999; Rusmini et al., 2007; Wong et al., 2009). Proteins are easily denatured or inactivated during immobilization, mostly due to changes in their tertiary structure (Jonkheijm et al., 2008; Rusmini et al., 2007; Sarma et al., 2009; Wong et al., 2009). Moreover, proteins adhere to surfaces through non-

specific interactions, i.e. electrostatic interactions, hydrogen bonding and hydrophobic interactions (Mrksich, 2005). Immobilization of biomolecules to sensor surfaces need to be consistent, as variations would have a major effect on the overall performance of the biosensor.

Electrochemical devices using ZnO which have been developed include field-effect transistors (FET) (Hagen et al., 2011; Kim et al., 2006), gas sensors (Lupan et al., 2007), pH sensors (Al-Hilli et al., 2007) and humidity sensors (Fang et al., 2009; Park et al., 2010; Zhang et al., 2005). Electromechanical devices that have been developed include acoustic wave based sensors (Talbi et al., 2006), nanogenerators (Chang et al., 2010; Wang and Song, 2006; Wang et al., 2007b; Xu et al., 2010), piezoelectric-FETs (Rocha-Gaso et al., 2009) and piezodiodes. Optoelectronic devices include UV detectors (Bai et al., 2011), UV lasers, solar cells (Law et al., 2005) and field emission devices (Hwang et al., 2011; Zhao et al., 2011).

This paper reviews the properties of ZnO and the different nanostructures that have been synthesized. Synthesis of ZnO nanowires by the two most popular methods, i.e. vapour phase synthesis and the hydrothermal solution method, are discussed. The immobilization of proteins is discussed, with special emphasis on methods used in non-specific immobilization. Self-assembled monolayers (SAMs) and their role in covalent binding of biomolecules are discussed in detail. ZnO nanowire devices developed are also reviewed.

2. ZnO nanostructures

Nanostructures are classified as 0-dimensional, 1-dimensional and 2-dimensional structures. Zero-dimensional structures include quantum dots and nanoparticles. Two-dimensional nanostructures are thin films, while 1-dimesional nanostructures refer to nanowires, nanobelts and nanotubes (Zhang et al., 2012). The interaction of polar surfaces makes the growth of diverse ZnO nanostructures possible (Wang et al., 2004). ZnO exhibits a variety of novel structures. These structures can be grown by tuning the growth rates along three fast growing directions: [2-1-10] (± [-12-10], ± [2-1-10], ± [-1-120]); [01-10] (± [01-10], ± [10-10], ± [1-100]) and ± [0001]. The relative growth rate of the various facets determines the surface morphology of the synthesized nanostructures (Baruah and Dutta, 2009).

Nanostructures such as nanobelts (Gao et al., 2005; Pan et al., 2001), nanosprings (Kong and Wang, 2003), nanorings (Kong and Wang, 2003), nanohelixes (Gao et al., 2005), nanobows (Hughes and Wang, 2004), nanowires (Huang et al., 2001b), nanotubes (Sun et al.,

2005), nanocages (Snure and Ashutosh, 2007), nanoshells (Leung et al., 2005), nanospheres (Zhang et al., 2009b), nanofibers (Fang et al., 2006), nano-tetrapods (Newton and Warburton, 2007), nanonails and nanobridges (Lao et al., 2003) have been synthesized. Of all the 1-dimensional ZnO nanostructures, ZnO nanowires have been studied extensively. Examples of ZnO nanostructures are shown in Fig. 1.

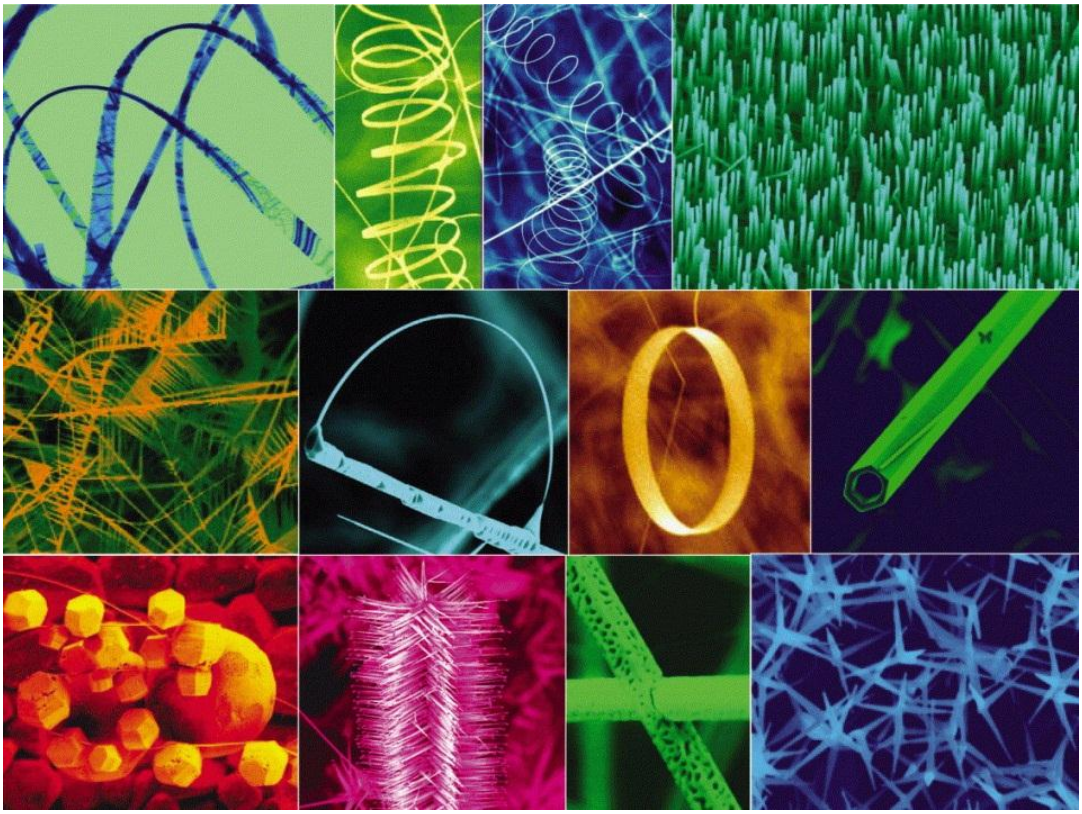

Fig. 1. Examples of ZnO nanostructures that have been synthesized (Wang, 2004a and b).

3 Properties of ZnO

The ZnO crystal has a hexagonal wurtzite structure and exhibits partial polar characteristics (Wang, 2004a), with lattice parameters a = 0.3296 nm and c = 0.52065 nm. The best description for a structure composed of ZnO is a number of alternately planes composed of tetrahedrally coordinated O^{2-} and Zn^{2+}, stacked alternatively along the c-axis (Fig. 2). The tetrahedral coordination in ZnO gives rise to the piezoelectric and pyroelectric properties, which is due to the absence of inversion symmetry (Wang, 2004a; Zhang et al., 2012). Another important characteristic of ZnO is the presence of polar surfaces. The most common polar surface is the basal plane (0001). One end of the basal plane terminates in partially positive Zn lattice sites and the other end in partially negative oxygen lattice sites. The

oppositely charged ions produce positively charged Zn-(0001) and negatively charged O-(000-1) surfaces, resulting in a normal dipole moment and spontaneous polarization along the c-axis, as well as variations in surface energy (Wang, 2004a).

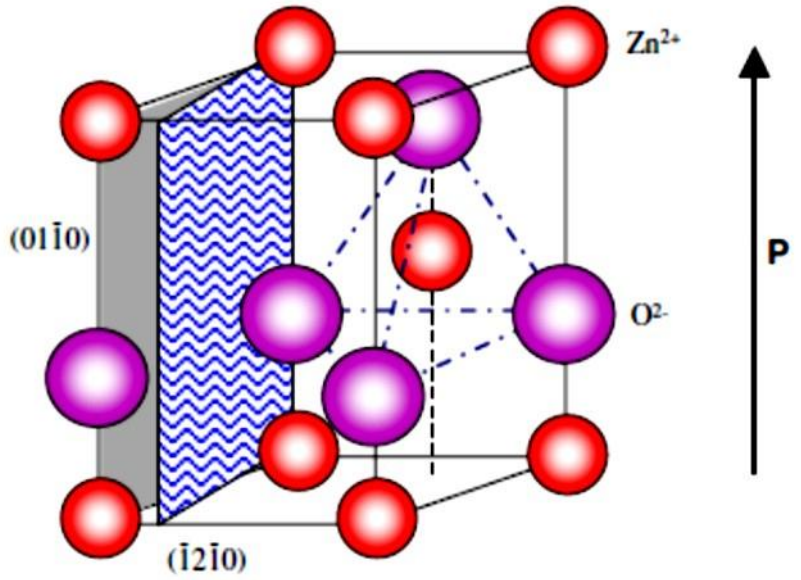

Fig. 2. Schematic representation of the wurtzite structure of ZnO, showing the tetrahedral coordination (Wang, 2004a).

To maintain a stable structure, the polar surfaces have facets or exhibit massive surface reconstructions. However, ZnO ± (0001) surfaces are exceptions in that they are atomically flat, stable and exhibit no reconstruction (Chen et al., 2000b; Emanetoglu et al., 1999). Understanding the superior stability of the ZnO ± (0001) polar surfaces are at the forefront of research (Lee et al., 2002a; Liang et al., 2001; Saito et al., 2002).

The other two most commonly observed facets for ZnO are (2-1-10) and (01-10), which are non-polar with lower surface energy than (0001) facets. Some typical growth morphologies of 1-dimensional ZnO nanostructures are shown in Fig. 3. These structures tend to maximize the areas of the (2-1-10) and (01-10) facets because of lower energy. The morphology shown in Figure 3 (b) is dominated by polar surfaces, which can be grown by introducing planar defects parallel to these surfaces. Occasional planar defects and twins can be observed parallel to the (0001) plane, but dislocations are hardly seen (Wang, 2007).

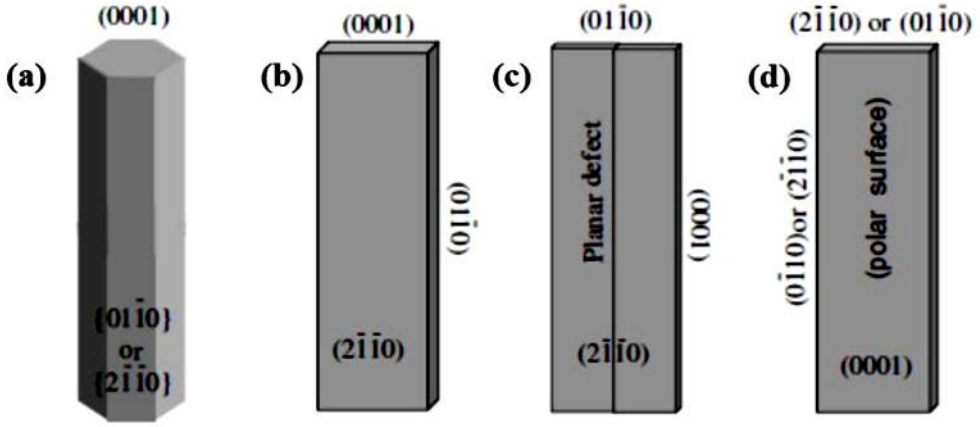

Fig. 3. Growth morphologies of one-dimensional ZnO nanostructures (**a**) nanowire, (**b**) nanobelts type I, (**c**) nanobelts type II, and (**d**) polar-nanobelts with corresponding facets (Wang, 2004a and b).

ZnO crystal possesses two important characteristics, i.e. the presence of polar surfaces and the lack of centre symmetry (Wang, 2008). The interaction of polar surfaces makes the growth of unique ZnO nanostructures possible. The lack in centre symmetry gives ZnO its piezoelectric and pyroelectric properties (Wang, 2008). Piezoelectricity is generated when pressure applied to the nanostructure causing displacement of Zn cations and O anions in the crystal. Numerous materials exhibit piezoelectric properties, e.g. quartz, wurtzite structured crystals, Rochelle salt, lead zirconate titanate ceramics, barium titanate and polyvinylidene fluoride (Wang, 2007). Another characteristic of ZnO is that it is a semiconductor with high bandgap energy of 3.37 eV (Zhao et al., 2007; Zhou et al., 2008). ZnO structures are biocompatible (Li et al., 2008), chemically stable, non-toxic, biomimetic and possess high electron communication features (Rodriquez et al., 2000; Sberveglieri et al., 1995; Tian et al., 2002), all of which renders these structures excellent transducers for biosensors.

4. Synthesis of ZnO nanowires

Because wurtzite structure has no centre of inversion, an inherent asymmetry along the c-axis is present which allows the preferential growth of the crystals along the [0001] direction (perpendicular to the surface) to form ZnO nanowires. The [0001] direction of ZnO crystals has the fastest growth velocity, and the growth rate under thermodynamic equilibrium for the hydrothermal approach is $V_{[0001]} > V_{[0110]} > V_{[1000]}$ (Baruah and Dutta, 2009).

Synthesis of ZnO nanostructures is broadly classified as either a solution phase or vapour phase approach. In the case of solution phase synthesis, the growth of ZnO nanowires is conducted in liquid. If aqueous solutions are used, the process is referred to as hydrothermal growth. Numerous solution phase methods have been developed to synthesize ZnO nanostructures. These include zinc acetate hydrate derived nano-colloidel sol-gel route (Spanhel, 2006), zinc acetate hydrate in alcoholic solutions with sodium hydroxide (NaOH) or tetra-methyl-ammonium-hydroxide (Kohls et al., 2002; Ma et al., 2005; Xu et al., 2003), template assisted growth (Shingubara, 2003), spray pyrolysis for growth of thin films (Ayouchi et al., 2003; Krunks and Mellikov, 1995) and electrophoresis (Wang et al., 2006b).

Vapour phase synthesis uses a gaseous environment in closed chambers to control the synthesis of ZnO nanowires. Synthesis is carried out at high temperatures ranging from 500 ° to 1500 °C (Dalal et al., 2006). Numerous gas phase methods for the synthesis of ZnO nanostructures have been developed. These include vapour phase transport, i.e. either vapour phase solid or vapour liquid solid growth (Miao et al., 2007; Pan et al., 2001; Wang and Li, 2002); physical vapour deposition (Dalal et al., 2006; Protasova et al., 2011); chemical vapour deposition (Satoh et al., 2005); metal organic chemical vapour deposition (Ashraf et al., 2011; Yasuda and Segawa, 2004); thermal oxidation of pure Zn and condensation (Li and Gao, 2007); microwave assisted thermal decomposition (Lagashetty et al., 2007); molecular beam epitaxy (Wang, 2009); pulsed laser deposition (Tien et al., 2008) and metal organic vapour phase epitaxy (Kitamura et al., 2008).

The most common techniques for the synthesis of ZnO nanowires, hydrothermal growth and the vapour-liquid-solid (VLS) phase synthesis, is further discussed in detail, with special emphasis on thermodynamic kinetics.

4.1 Vapour-liquid-solid (VLS) phase synthesis

Vapour-liquid-solid phase synthesis of ZnO nanowires involves the evaporation and condensation of zinc vapour onto a substrate in the presence of oxygen (Fig. 4). Zinc vapour is produced by evaporation, chemical reduction, and gaseous reactions, after which the evaporated Zn is transferred and condensed onto a substrate to form ZnO nanowires. The vapour phase approach is differentiated as a catalyst-free vapour-solid (VS) process and catalyst-assisted VLS process. During the VS approach, nanowires are synthesized by direct

condensation of Zn vapour. This approach provides less control over the dimension and orientation of the synthesized ZnO nanowires. Controlled growth of ZnO nanowires is achieved by the VLS approach (Li et al., 2003b; Sberveglieri, 1995; Yang et al., 2002), using catalysts such as Au, Cu, Co or Sn (Chang et al., 2004; Gao et al., 2003; Lee et al., 2002a). Formation of eutectic alloy droplets occur at each catalytic site, followed by the nucleation and growth of ZnO nanowires as each droplet super saturates. Incremental growth of ZnO crystals takes place at the droplet interface, which constantly pushes the catalyst upwards resulting in synthesized nanowires with a catalytic tip at the end of the structure.

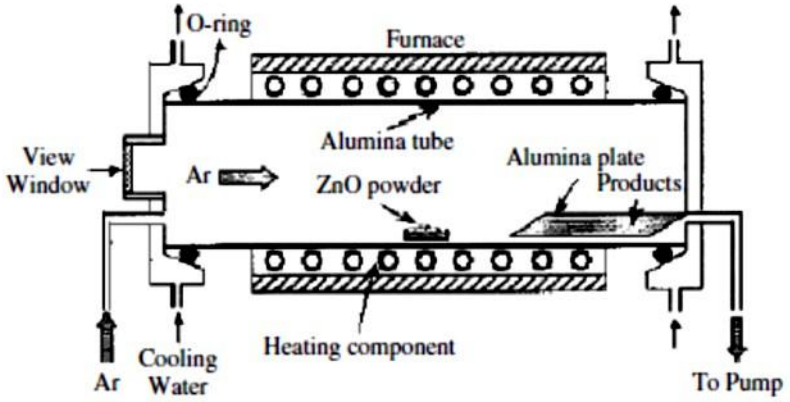

Fig.4. A schematic diagram of the growth of ZnO nanostructures by using the solid-vapour phase process (Wang, 2004a).

Kinetics of the carbothermal reduction and reoxidation of Zn vapour, which leads to the formation of ZnO nanowires, is complex and involves controlling several interdependent variables. The growth of ZnO nanowires are affected by the chamber pressure, oxygen partial pressure, chamber temperature, and thickness of the catalytic layer (Song et al., 2005; Wang et al., 2006b).

Control of the Zn reoxidation and condensation kinetics seems to be key to achieving controllable well-aligned growth. The thermodynamic equation is described as follows:

$$ZnO_{(solid)} + C_{(solid)} \leftrightarrow Zn_{(vapour)} + CO_{(gas)} \ (T > 970\ ^\circ C) \quad (1)$$

$$2C + O_2 = 2CO \quad (2)$$

$$2CO + O_2 = 2CO_2 \quad (3)$$

$$2Zn + O_2 = 2ZnO \quad (4)$$

Chamber pressure has the most profound effect on the morphology of the nanowires. Varying the pressure changes not only the diameter, length and density, but also the morphology of the ZnO nanostructures. Chamber pressure affects the supersaturation level of the vapour, which is critical in determining the type of growth that occurs (Yang et al., 2002). Supersaturation is higher at low pressures and decreases at higher pressures (Menzel et al., 2012). Variation in the oxygen partial pressure directly affects the process of reoxidation of the Zn vapour and thus also the growth rate (Yang et al., 2002).

Chamber temperature affects the growth in three ways: temperature affects the size of the catalytic droplet, i.e. it determines how much the vapour would condense. This in turn determines the length of surface diffusion of the absorbed vapour (Dalal et al., 2006). Higher deposition temperatures results in the formation of smaller catalytic-Zn droplets which in turn results in thinner and denser ZnO nanowires (Wang, 2004b). With the decrease in chamber temperature, the nanowires become wider and shorter. Surface diffusion and condensation of vapour yield differences at different temperatures. Higher chamber temperatures results in shorter nanowires with smaller diameters, whereas lower temperatures results in diameter and height increases (Lyu et al., 2003).

The thickness of the catalytic layer affects the diameter and density of the synthesized nanowires (Dalal et al., 2006). Due to minimization of free energy (Hu et al., 1999), the diameter of the nanowires is related to the size of the catalytic droplet. When the droplet reaches supersaturation, ZnO precipitates as nanowires, with diameters equal to that of the catalytic-Zn islands (Li et al., 2009). Dense areas of nanowires can be reached when thinner catalytic films are used. An SEM image of ZnO nanowires synthesized by the VLS approach is shown in Fig. 5. The catalytic tip at the end of each nanowire is clearly visible.

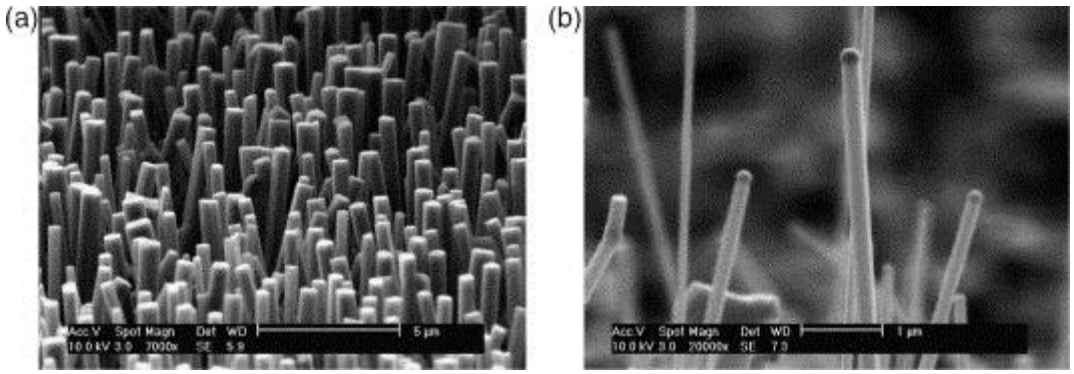

Fig. 5. (**a**) ZnO nanowires grown by using the VLS method, (**b**) ZnO nanowires with gold particles on their tips (Xing et al., 2006).

4.2 Hydrothermal method

This method involves an aqueous mixture of soluble metal salts (metal and/or metal-organic compounds) which is placed in an oven under elevated temperatures (70-90 °C) to form ZnO nanowires (Fig. 6). The method is preferred in the synthesis of ZnO nanowires, due to lower synthesis temperatures as opposed to the VLS method (Guo et al., 2005; Liu and Zeng, 2003; Wang and Gao, 2003).

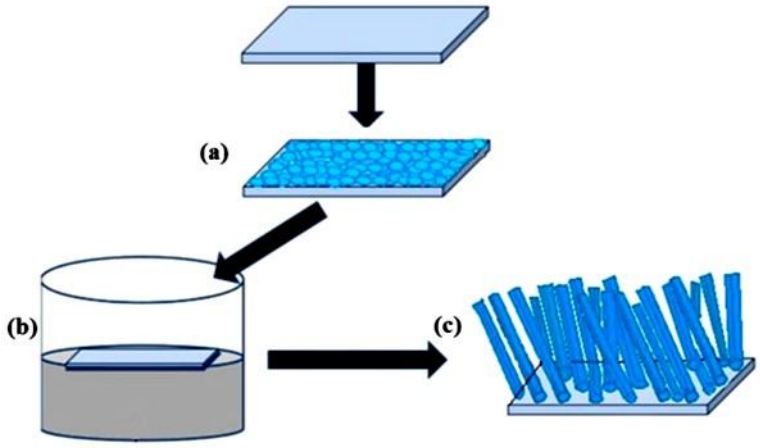

Fig. 6. Schematic diagram of the hydrothermal growth approach. A substrate (**a**) is coated with a ZnO seed layer, which is placed in a aqueous solution containing equimolar amounts of zinc nitrate hexahydrate and hexamethylenetetramine at 90 °C (**b**), resulting in the growth of ZnO nanowires (**c**).

Growth of ZnO nanowires in aqueous solutions requires controlled precipitation of ZnO on a substrate through hydrolysis/condensation reactions of metal ions and their complexes (Baruah and Dutta, 2009). Hexamethylenetetramine (HMTA) added to the reaction acts as a pH buffer and supplies OH^-, HMTA hydrolysis forms formaldehyde which is converted to ammonia. Ammonia reacts with water to form OH^- which drives the crystallization of ZnO (McPeack et al., 2011). Ammonia and ammonium salts are added to the reaction. The lone-pair electrons on the nitrogen then react with empty orbitals of metal ions, generating metal-ammonium complexes. These complexes stabilize the structural units that modify, promote and direct the formation of nanostructures (Wen et al., 2008).

The growth of ZnO nanowires is controlled by controlling the supersaturation of the reactants. High supersaturation levels favour nucleation and low supersaturation levels favour crystal growth (Weintraub et al., 2010). If high levels of OH^- are produced in a short period, the Zn^{2+} ions in the solution precipitates rapidly and nanowires do not form (Xu et al., 2008b). It is thus important to control the concentration of OH^- in the solution to ensure low levels of supersaturation. Growth of ZnO nanowires by the hydrothermal growth approach is expressed by the following reactions (Wang et al., 2008).

$$(CH_2)_6N_4 + 6H_2O \rightarrow 6HCHO + 4NH_3 \quad (1)$$

$$NH_3 + H_2O \leftrightarrow NH_4^+ + OH^- \quad (2)$$

$$2OH^- + Zn^{2+} \rightarrow Zn(OH)_2 \quad (3)$$

$$Zn(OH)_2 \rightarrow ZnO + H_2O \quad (4)$$

Numerous factors need to be taken into consideration when synthesizing nanowires by the hydrothermal growth method. These factors includes the type of zinc salt precursor, concentration of the precursor (Li et al., 2005), pH of the growth solution (Baruah and Dutta, 2009), growth temperature and time (Wang et al., 2012), presence of impurities (Wang et al., 2012), substrate onto which nanowires are grown (Yousefi and Zak, 2011), the addition of chelating agents (Wen et al., 2008), and the presence of a ZnO seed layer (Wang, 2004a).

Low ZnO precursor concentrations decrease the diameter and length of nanowires (Hirano et al., 2005; Li et al., 2005). Morphology and growth rate can be controlled by controlling the pH of the reaction (Pal and Santiago, 2005). During the initial growth stage, the pH and the concentration of Zn^{2+} ions is such that ZnO growth occurs through $Zn(OH)_2$ formation. With a gradual increase in the pH of the reaction solution (due to increased hydrolysis of HMTA) and a decrease in the concentration of Zn ions, $Zn(OH)_2$ becomes thermodynamically unstable and the $Zn(OH)_2$ formed on the substrate dissolves (Baruah and Dutta, 2009).

Growth temperature affects nucleation and the growth rate of nanowires, and therefore plays a significant role in shaping the synthesized nanowires. ZnO nanowires do not form at low temperatures (48 °C). Higher temperatures (58-88 °C) results in thicker films and better nanowires alignment (Wang et al., 2012). However, when the temperature is too high (95 °C) the reaction occurs inside the solution, which consumes the reactants to produce ZnO

nanoparticles, leading to slower nanowire growth and bush-like bundles. This is possibly due to the presence of impurities in the solution. When the growth temperature increases from 60 to 90 °C, the average diameter of the synthesized ZnO nanowires decreases (Guo et al., 2005). The increase in temperature causes evaporation of ammonia. Left long enough, there may not be enough base left in the solution to react with the Zn precursor, thus restricting nanowire growth. The length of the nanowires can be tailored by adjusting the growth time, although the growth rate decreases with time. An increase in time results in longer and intertwined nanowires (Li et al., 2005). Growth time does, however, not influence the average diameter of the synthesized ZnO nanowires (Kenanakis et al., 2009).

The presence of impurities (i.e. dust, undissolved chemicals) on the surface and in solution results in more favourable nucleation sites for growth of nanowires, as these impurities have larger grain sizes than those of the deposited ZnO seed layer nuclei. The ZnO nanowires grow radically outwards from the larger grains and form bush-like nanowire bundles which are disoriented (Wang et al., 2012).

The morphology and alignment of the ZnO nanowires are also affected by the substrate onto which the nanowires are synthesized. As lattice mismatches between the substrate and the ZnO nanowires (Yousefi and Zak, 2011) influences the dimensions and aligment of the synthesized ZnO nanowires. Surface atoms in a Si (100) substrate are arranged in a square pattern, whilst they follow a hexagonal pattern for a Si (111) substrate. This is also seen in ZnO crystal structures. The Si (111) surface has a better matching lattice with the ZnO lattice, compared to that of Si (100). ZnO nanowires grown on Si (111) substrates have larger diameters than those grown on Si (100) and are more crystalline than amorphous (Yousefi and Zak, 2011).

The HMTA chelating agent supplies OH^- ions for ZnO growth through a process called thermal decomposition (Govender et al., 2004; McPeak et al., 2011; Schmidt-Mende and MacManus-Driscoll, 2007). Compared to strong bases such as NaOH, HMTA releases OH^- groups much slower and control crystallization more accurately (Xu et al., 2010). ZnO crystallization is therefore under thermodynamic control, which promotes heterogeneous nucleation and growth over homogeneous nucleation (McPeak et al., 2011). HMTA acts as a shape-inducing surfactant (Fig. 7) and attaches to the non-polar facets of ZnO, thereby restricting the access of Zn^{2+} ions leaving only the polar (0001) facets open for epitaxial growth (Sugunan et al., 2006). Addition of ethylenediamine (EDA) as a chelating agent

inhibits the radial enlargement of nanowires (Wen et al., 2008). Cetyl trimethylammonium bromide (CTAB) addition has a profound effect on the final morphology of the synthesized nanostructures. The chelating agent binds to positive polar plane rich in Zn^{2+}, thus retarding growth of ZnO nanowires (Wen et al., 2008). Polyethylenimine (PEI) affects nanowire growth by inhibiting crystal growth along the *a* and *b* directions, thus increasing the aspect ratio of the synthesized ZnO nanowires (Xu et al., 2010). Addition of ammonia ($NH_3 \cdot H_2O$) suppresses the homogeneous nucleation of ZnO in solution by forming zinc amine complexes (Greene et al., 2006).

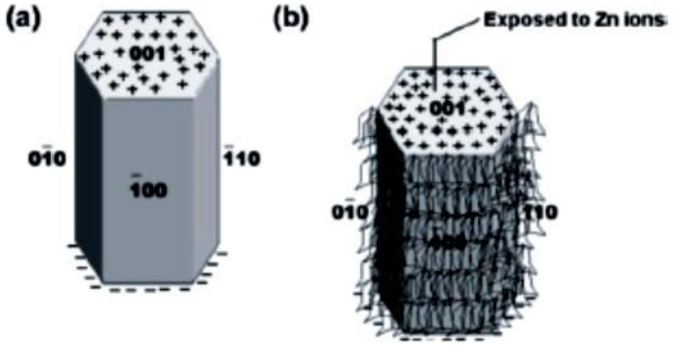

Fig. 7. Attachment of hexamine to the non-polar facets of the ZnO crystals, allowing the growth of crystals in a (0001) direction. (**a**) A hexagonal ZnO crystal and (**b**) possible attachment of hexamine onto the non-polar facets, leaving the polar facets exposed allowing further crystal growth along the c-axis (Sugunan et al., 2006).

Presence of a ZnO seed layer affects the dimensions and orientation of the synthesized ZnO nanowires. Several methods have been developed to deposit ZnO seed layer films, i.e. chemical vapour deposition (Hu and Gordon, 1992), reactive evaporation (Swamy and Reddy, 1990), pulsed laser ablation (Ardakani, 1996), sputtering (Yoon et al., 1997), spray pyrolysis (De le Olvera et al., 1993), hydrothermal evaporation (Nishizawa and Yuasa, 1998) and sol-gel spin coating (Ohyama et al., 1997).

The most important role of ZnO seed layers is to align the synthesized nanowires. This is achieved due to matching lattice structures and the polar nature of the ZnO surface (Wang, 2004a). The ZnO surface is either positively charged or negatively charged. In either case the surface will attract ions of opposite charges (OH^- or Zn^{2+}) to form ZnO (Li et al., 2005). Thus, the ZnO seed layer initiates nanowire growth, layer by layer, to form the correct alignment. In addition, ZnO nanowires grow intrusively along the [0001] direction. This is

due to a dipole charge that ZnO has along this direction. This dipole charge will align itself with charged surfaces of the ZnO thin film to minimize energy (Wang, 2004a and b). The ubiquitous surface roughness formed from the seed layer serves as nucleation sites for nanowire growth (Wen et al., 2008). Introducing the seed layer effectively lowers the interfacial energy between the crystal nuclei and the substrate, hence decreasing the nucleation barrier and facilitating the growth of ZnO nanowires. The size of the ZnO seed grains also determines the size of the synthesized ZnO nanowires (Cui et al., 2005). The ZnO seed layer grains and surface roughness increase with the increase in deposition, which subsequently increases the diameter of the synthesized ZnO nanowires (Kenanakis et al., 2009). Nanowires synthesized on less oriented seed layers reduce the c-axis alignment and forms random crystallographic orientation (Erdélyi et al., 2011).

With the increase in the ZnO seed layer grain and film thickness the mean diameter of the synthesized ZnO nanowires increases (Tak and Yong, 2005). Deposition of ZnO seed layers by the sol-gel spin coating technique requires controlling factors such as baking temperature and time, sintering temperature and time, and concentration of the Zn precursor. The speed at which the organic solvent evaporates should be similar to that of ZnO crystallization (200 °C). Too high temperatures (350 °C) results in fast-growing grains with random orientation. This worsens the ZnO nanowire orientation. If the temperature is too low (150 °C), organic compounds are deposited and the seed layer shrinks (Xiao and Kuwabara, 2005). At low sintering temperatures (500 °C), the grain sizes are small and the boundaries unclear. At 700 °C the grains are larger and clear, whereas too high temperatures (900 °C) results in a discontinuous seed layers (Xiao and Kuwabara, 2005). For a high Zn sol-gel precursor concentration the seed layer results in closely packed ZnO nanowires, as compared to lower concentrations which result in less densely packed ZnO nanowires (Ghosh et al., 2007). Higher concentration also produces nanowires with a smaller diameters, opposed to lower concentrations (Ghosh et al., 2007). Factors that need to be controlled during ZnO seed layer deposition by sputtering techniques are sputtering time and power, as these influences the diameter of the ZnO grains, and subsequently the diameter of the synthesized ZnO nanowires. The ZnO grain diameters decrease with an increase in sputtering power, which in turn leads to a decrease in the mean nanowire diameter (Wang et al., 2012). A SEM image of ZnO nanowires synthesized by the hydrothermal growth approach is shown in Fig. 8.

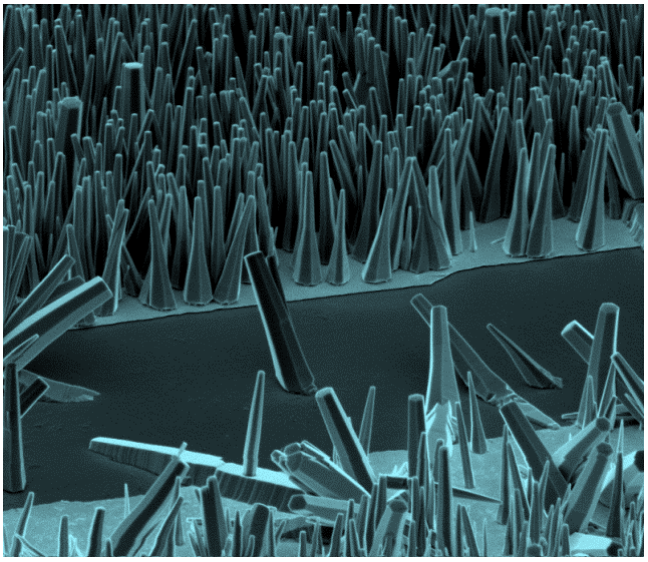

Fig. 8. ZnO nanowires synthesized by the hydrothermal growth approach.

5. Protein immobilization strategies

Protein immobilization can be defined as the attachment of biomolecules to a surface with the reduction or loss of mobility. The immobilization strategy may lead to the partial/complete loss of protein activity, which is attributed to random orientations and structural deformations induced. To fully retain biological activity of the immobilized protein, proteins should be attached onto surfaces without affecting conformation or active sites. The immobilization strategy is choosen based on the physicochemical and chemical properties of the surface and biomolecule to be immobilized. Numerous immobilization strategies have been developed and are broably classified as physical, covalent, and bioaffinity immobilization (Rusmini et al., 2007). This paper focusses on physical and covalent immobilization strategies, as they do not require engineering of the biomolecule to be immobilized. Biomolecules have their own characteristic and functional properties. It is thus not possible to use the same strategy for different proteins. The physical and chemical stability of adsorbed proteins and the retention of the biological activity are general requirements for protein immobilization (Brinkley, 1992; Johnson and Martin, 2005; Karyakin et al., 2000; O'Shannessy et al., 1992; Tsang et al., 1995).

The most challenging step during the development of biosensors is the immobilization of biomolecules in such a manner that they are positioned close to the surface, whilst retaining biological activity. Furthermore, the immobilization strategy has to render the

biomolecule enhanced stability and robustness, be applicable to many different biological molecules, has to be resistant to the reagents and metablic compounds and control the distribution and orientation of the immobilized biomolecule (Gooding and Hibbert, 1999). Covalent immobilization using linkers (coupling agents) has gained considerable attention as an alternative method (Brinkley, 1992; Karyakin et al., 2000; O'Shannessy et al., 1992). This strategy provides direct and robust coupling to solid substrates via the formation of physical and chemical stable covalent bonds by using various linkers on substrates (Kim et al., 2010).

Self-assembled monolayers (SAMs) can provide reproducible and robust immobilization, as some control over the orientation and distribution is afforded, due to the targeting of selected amino acid functional groups. Furthermore, the affinity thiols have for some metal surfaces, particularly gold, renders alkanethiols SAM ideal for the immobilization of biomolecules (Gooding and Hibbert, 1999). Despite many advantages of covalent conjugation, the orientation of immobilized proteins are significantly affected by the choice of linkers used and the corresponding conjugation sites targeted for covalent bonding (Karyakin et al., 2000). Physical and covalent immobilization strategies do not require alterations to the protein structures for immobilization to occur, as opposed to bioaffinity immobilization. These immobilization strategies will be discussed in more detail.

5.1 Physical immobilization

Proteins can adsorb onto surfaces via intermolecular forces, mainly ionic bonds and hydrophobic and polar interactions (Wong et al., 2009). The intermolecular forces that participates in the interaction depends on the particular biomolecule and surface. The resulting layer is likely to be heterogeneous and randomly oriented, since each molecule can form many contacts in different orientations for minimizing repulsive interactions with the substrate (Rusmini et al., 2007). The adsorption capacity is limited by the geometric size of the immobilized biomolecule (Khan et al., 2006).

The advantage of using such a strategy for protein immobilization is that neither coupling reagents nor modifications to the biomolecule is required for immobilization to occur. Physical immobilization strategies involve relatively weak and reversible interactions, that result in desorption of the biomolecule and loss of activity over time (Khan et al., 2006). This has reproducibility implications, particularly when used in analytical assays and

biosensors. Additionally, immobilization of biomolecules to surfaces through physical strategies often results in conformational changes and denaturation of the biomolecule, resulting in loss of biological activity (Butler, 2000). Furthermore, since there is no control over the packing density of immobilization by this strategy, the biological activity may be further reduced by steric hindrance (Kusnezow and Hoheisel, 2003).

5.2 Covalent immobilization

Biomolecules are often covalently bound to surfaces through accessible functional groups of exposed amino acids. During this strategy covalent bonds are formed between side-chain functional groups of biomolecules with suitably modified surfaces, resulting in an irreversible bond and high surface coverage.

Table 1 shows the functional groups in biomolecules targeted for immobilization and the required surface properties for covalent bonding to occur. Amino acid side chain groups targeted for chemical conjugation should not be in high abundance (> 10%), as attachment through several residues may form simultaneously, thereby restricting the conformational freedom and also increasing heterogeneity in the population of immobilized biomolecules (Fransconi et al., 2010).

Covalent immobilization using amino acid side chains are often random, since it is based upon residues typically present on the exterior of the protein. The attachment may thus occur simultaneously at many residues. This approach lacks regiospecificity and an immobilized biomolecule may not be correctly oriented. The reactive site of the biomolecule may also be blocked, resulting in a reduction or loss of biological activity (Fransconi et al., 2010). To ensure retention of biological structure and activity, a homogeneous surface orientation on modified surface should be sought (Fransconi et al., 2010).

Table 1. Functional groups available in biomolecules for immobilization and surface properties required for covalent bonding (Rusmini et al., 2007).

Side chain groups	Amino acid	Surface property
$-NH_2$	Lys, hydroxyl-Lys	carboxylic acid
		active ester (NHS)
		epoxy
		aldehyde
−SH	Cys	maleimide
		pyridyil disulfide
		vinyl sulfone
−COOH	Asp, Glu	amine

The most common method to covalently bind biomolecules to surfaces involves the functionalization of self-assembled monolayer (SAM) surfaces, which is then conjugated to a biomolecule. Different classes of chemical reactions have been explored for modifying surfaces, e.g. nucleophilic substitution, esterification, acylation and nucleophilic addition (Sullivan and Huck, 2003).

One of the simplest and most applicable methods used to modify SAMs exploits the formation of amide linkages via an interchain anhydride intermediate (Ducker et al., 2008; Sun et al., 2006). Trifluoroacetic anhydride dehydrates, when exposed to amine groups of amino acid side chain groups, form an amide bond (Fig. 9 a). However, one disadvantage of using NHS esters is that they are unstable in aqueous conditions. The attachment of proteins in aqueous buffers will thus compete with ester hydrolysis, resulting in only modest levels of immobilization. Aldehyde functional surfaces can be coupled with exposed amines of biomolecules to produce an imine that is reduced by sodium cyanoborohydride to form a stable secondary amine linkage (Hahn et al., 2007; MacBeath and Schreiber, 2000) (Fig. 9 b). SAMs containing maleimide terminal functional groups may react with cysteine residues of biomolecules (Houseman et al., 2003) to form stable covalent bonds (Fig. 9 c). Proteins generally have very few surface-exposed Cys residues and it is thus possible to achieve site-selective immobilization. If the protein of interest can be engineered to remove all but one surface Cys residue, or to insert a single Cys on the surface where none previously existed,

site-specific immobilization can be achieved (Cheung et al., 2003; Ferrero et al., 2008). The nucleophilicity of the amine groups also allows reaction with epoxide functionalized materials (Reynolds et al., 2007) to form a covalent bond (Fig. 9 d).

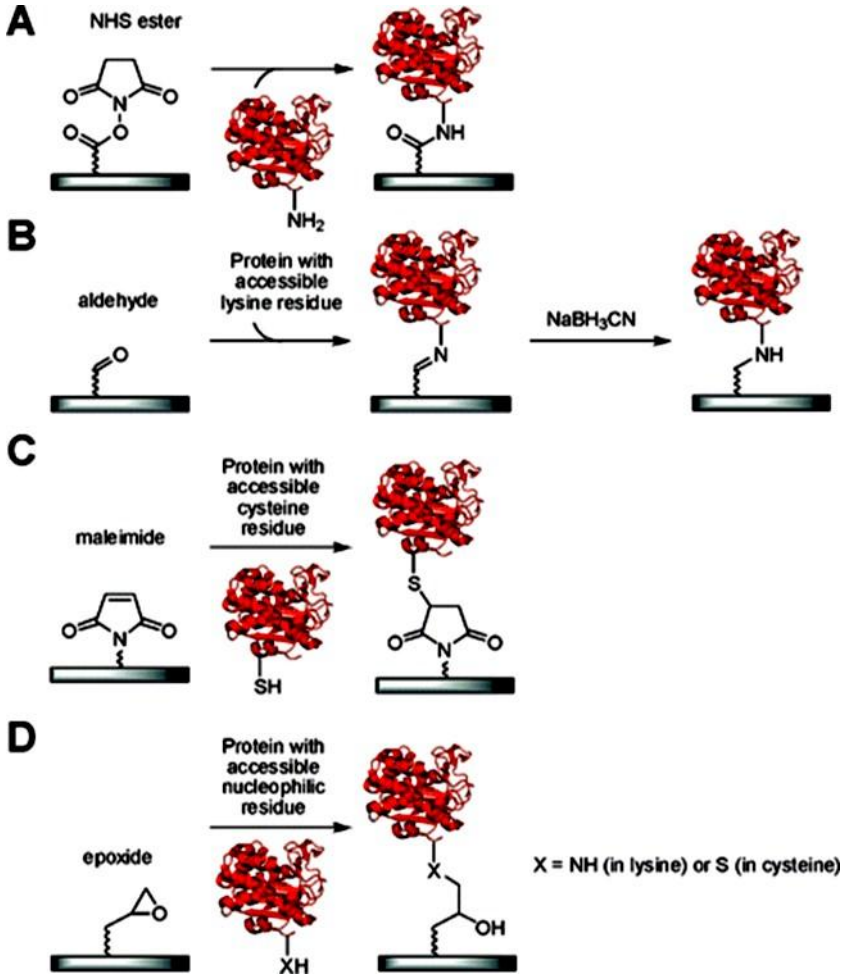

Fig. 9. Schematic representation of chemoligation methods for immobilization with nucleophilic residues of biomolecules. The reaction of lysine residues to NHS esters (**a**) or aldehydes (**b**) and cysteine residue bonding to maleimide groups (**c**). Epoxides may react with either of the nucleophilic residues (**d**) (Wong et al., 2009).

Aspartate (Asp) and glutamate (Glu) residues of biomolecules can also be targeted for immobilization by converting them to active esters with a carbodiimide coupling agent and an auxiliary nucleophile (Fig. 10). The most commonly used coupling agent is N-ethyl-N-(3-dimethylaminopropyl) carbodiimide (EDC), whereas N-hydroxysuccinimide (NHS) is widely used as the auxiliary to generate the NHS ester on biomolecules (Liu et al., 2006; Subramanian et al., 2006a and b; Yam et al., 2006; Wong et al., 2009). These active esters react with an amine bearing surfaces to form a covalent bond. Immobilization efficiency with

using this strategy dependents on several factors, such as the pH of the solution, concentration of coupling reagents, and the reaction time (Fransconi et al., 2010). Advantages of using this covalent immobilization strategy, is that the reagents are water-soluble, although the instability of carbodiimides and the active esters subsequently generated under these conditions means that the reaction yields are low (Wong et al., 2009). NHS-esters formed on the biomolecules may, however, interact with each other to form poorly defined polymers.

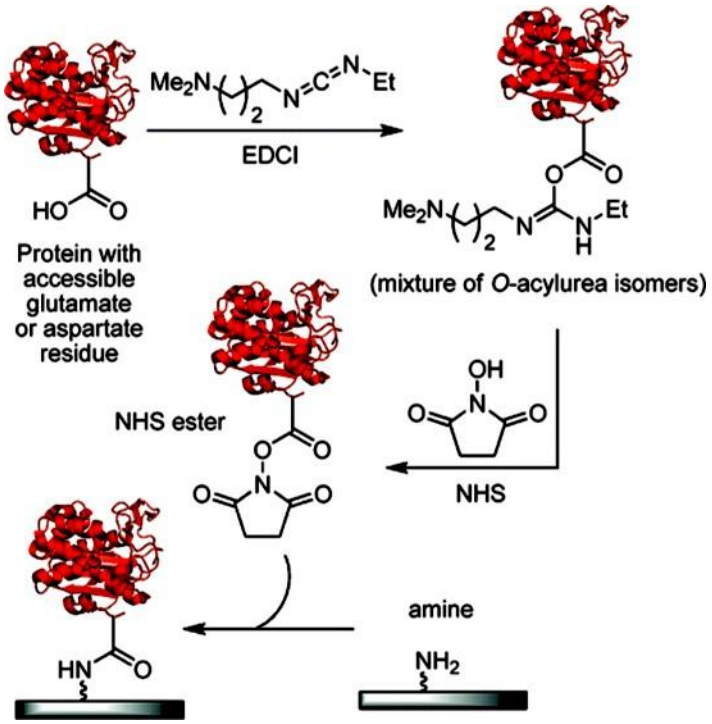

Fig. 10. Carbodiimide-mediated chemoligation of Glu and Asp residues of biomolecules to amine-functionalized surfaces via the generation of active NHS esters (Wong et al., 2009).

6. Self-assembled monolayers (SAMs)

Self-assembly is a process which involves the spontaneous arrangement of atoms and molecules in an ordered functional structure which is a strategy used in nature to create life from basic building blocks (Samanta and Sakar, 2011). Biological membranes, cellular structures and viruses can be regarded as sophisticated self-assembly systems (Vericat et al., 2010). Among various self-assembly processes, the formation of a self-assembled monolayer (SAM) is the most elegant way for creating an organic thin film with specific surface properties onto which biomolecules can be immobilized (Flink et al., 2000; Gooding and Hibbert, 1999; Love et al., 2005; Ulman, 1996).

Some control over the orientation and distribution of the immobilized protein is afforded by this approach, which is due to the reactivity of the SAM functional groups towards specific functional groups of the biomolecule. The affinity of thiols for some metal surfaces (i.e. Au, Ag, Pt and Cu), particularly gold, makes alkanethiols ideal absorbates for the formation of SAMs (Gooding and Hibbert, 1999). Numerous surface-active organosulphur compounds have been studied for SAM formation on gold. These include alkanethiols, arenethiols, alkanedithiols, arenedithiols, dialkyl disulphides and dialkyl sulphides. Alkanethiols and dialkyl disulphides for similar SAMs (Biebuyck et al., 1994; Noh et al., 2000), however, disulphides have solubility issues which could lead to the formation of multilayers, whereas dialkyl sulphides form a weaker bond with gold in comparison to thiols and disulphides (Fransconi et al., 2010; Jung et al., 1998).

SAMs are formed by attaching organic compounds from solution or gas phase onto a solid surface. The absorbates organize spontaneously into crystalline/semicrystalline structures. A thiol SAM consists of three parts: the sulphur head, the hydrocarbon chain (of variable length), and the terminal group (different functionalities) (Fig. 11). The headgroups guides the self-assembly process, linking the hydrocarbon chain to the metal surface through a strong semi-covalent bond.

Interactions among backbone hydrocarbon chains (involving van der Waals and hydrophobic forces) ensure an efficient packing of the monolayer and contribute to stabilization. The terminal group confers specific properties to the surface (hydrophilic, hydrophobic), and can be used to anchor different biomolecules by weak interactions or covalent bonds (Dubois and Nuzzo, 1992; Love et al., 2005). The energy related to each part of the molecule has a different order of magnitude: 50 kcal mol^{-1} for the interaction between the S head and the substrate (a thiolate bond); 1–2 kcal mol^{-1} per methylene for the van der Waals interactions between hydrocarbon chains; and only a few kT for energies related to the terminal groups (Ulman, 1996). However, all three parts of the molecule contribute to the structure and to the physical and chemical properties of the SAM (Vericat et al., 2005).

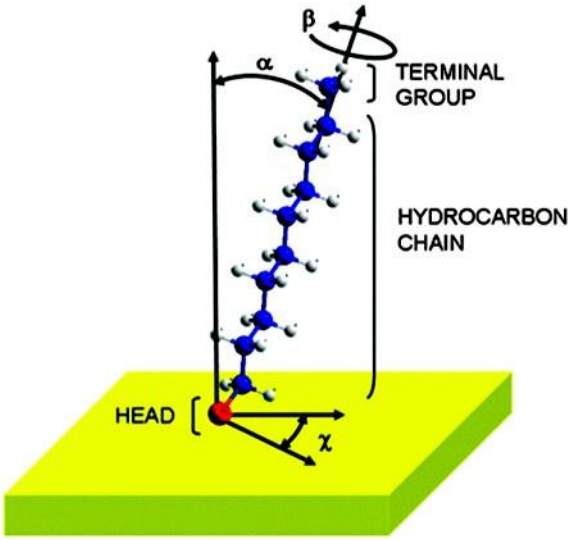

Fig. 11. Schematic representation of an alkanethiolate molecule adsorbed on Au (111) in a standing up configuration (stable phase). The angles are α = 30˚, β = 55˚ and x = 14˚ (Vericat et al., 2010).

Combined SAMs (Fig. 12) are useful for controlling the degree of biomolecule immobilization (Mrksich, 2009). They are formed from the co-adsorption of two different absorbates of similar dimension, but possessing different terminal functional groups (one reactive and one inert). Combined SAMs provides a method for incorporating molecular species with physical dimensions that would normally prevent a well-organized assembly (Gooding et al., 2003). By varying the composition of a combined SAM, the density of attachment points can be controlled and hence also the surface loading of the biomolecule (Gooding and Hibbert, 1999). The ratio of the two dissimilar molecules is usually proportional to the ratio of the initial concentration of the absorbates (Bain et al., 1989a; Wasserman et al., 1989).

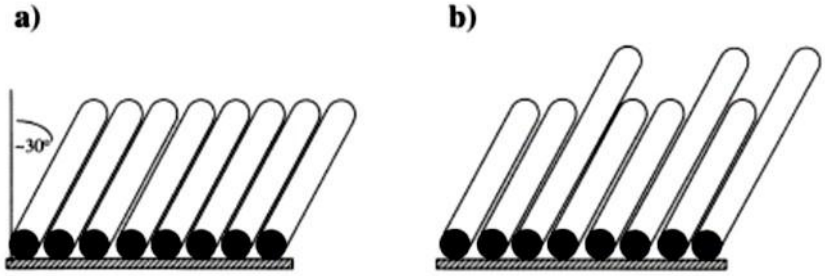

Fig. 12. Schematic representation of self-assembled monolayers of alkanethiols on gold. (**a**) A pure monolayer and (**b**) a mixed monolayer (Gooding and Hibbert, 1999).

Dithiolated SAMs contain two identical alkyl thiol substituents attached to a phenyl ring through phenolate bridges, providing two attachment points on the surface (Subramanian et al., 2006b). This generates monolayers which are more stable than monothiols. Furthermore, it provides more adequate spacing, thus allowing improved mobility and flexibility at the recognition terminus (Gobi et al., 2007).

6.1 SAM kinetics

Alkanethiols adsorb spontaneously on metal surfaces (i.e. gold, silver, platinum and copper). Gold is the most frequently used, because it does not have a stable oxide under ambient conditions. The thiol groups absorb onto the metal surface via a metal-thiol bond (Li et al., 1992; Ulman, 1996). The alkyl chains bound to the surface is in a trans-conformation, tilted at an angle of 20-30° to the surface, resulting in the formation of densely packed highly ordered monolayers (Gooding et al., 2003). Van der Waals forces between the alkyl chains enhance the stability and order of the SAM (Bain et al., 1989b). Therefore, long-chain alkanethiols produce more ordered SAMs than shorter chains. The order of monolayer is also adversely affected by the roughness of the surface (Creager et al., 1992).

Many controversies still exist about the kinetics of the assembly process and the structural characteristics of the alkanethiol SAM–metal surface interface, such as the head-group bonding structure, the packing configuration and the nature of the adsorption site (Li et al., 2003a; Torrelles et al., 2006). It is nevertheless clear that the process involves a subtle interplay of the energetics of the metal–sulphur bonds and non-covalent lateral interactions among the organic groups (Love et al., 2005).

The specific ordering of the sulphur moieties on the metal lattice defines the free space available to the organic components. The lateral interactions between alkyl chains (van der Waals, hydrogen bonding) determine the organization of the monolayer (Love et al., 2005). The metal–sulphur interaction drives the assembly. The lateral interactions of alkyl chains promote the secondary organization, resulting in a superlattice structure (Fransconi et al., 2010). Typical defects observed for SAMs on metal surfaces include, missing rows, vacancy Au islands, molecular defects, and disorder (Vericat et al., 2005) (Fig. 13).

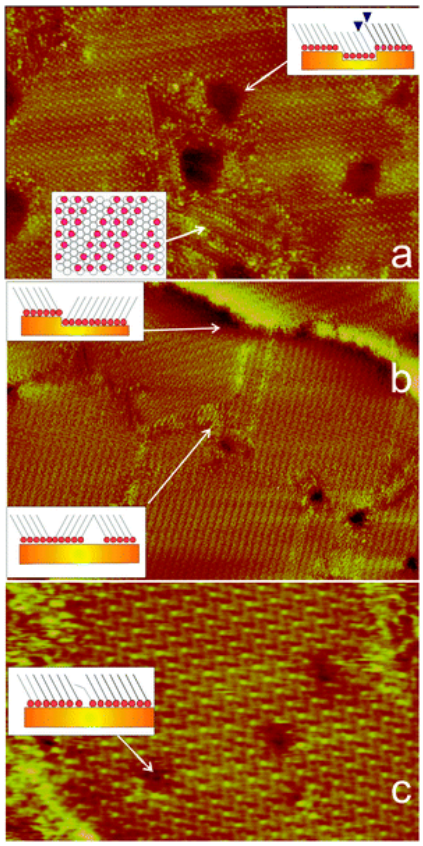

Fig. 13 STM images of alkanethiolate SAMs on Au (111) showing different types of surface defects (sketched in the insets) (**a**) vacancy islands and missing rows (48 × 32 nm^2 image), (**b**) domain boundaries and step edges (46 × 33 nm^2 image) (**c**) molecular defects (pinholes) (19 × 12 nm^2 image) (Vericat et al., 2010).

SAM formation occurs in two steps; an initial fast step of absorption, followed by a slower step of monolayer organization (Godin et al., 2004; Schwartz, 2001). Initially, a small molecular density binds to the surface (Fig. 14 i) and forms either an ordered two dimensional lying down phase (Fig. 14 ii), or a disordered mass of vertically orientated molecules (Fig. 14 iii) (Schreiber, 2000; Schwartz, 2001). As more molecules absorb to the surface, the molecules form a three dimensional crystalline or semi-crystalline structure on the surface (Fig. 14 iv) (Schwartz, 2001; Vos et al., 2003). The head groups assemble together, while the tail groups assemble far from the surface. Areas of close-packed molecules nucleate and grow until the surface of the substrate is covered in a single monolayer.

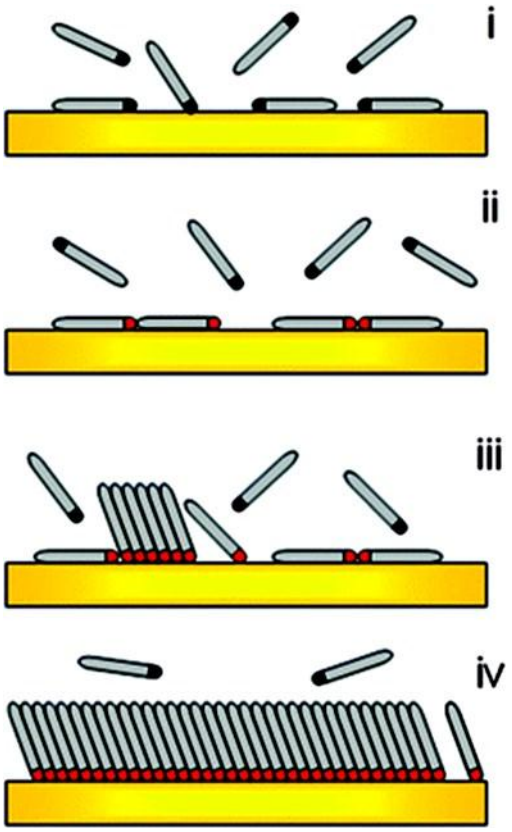

Fig. 14. Schematic representation of the different steps during the self-assembly of alkanethiol on Au (111): (**i**) physiorption, (**ii**) lying down phase formation, (**iii**) nucleation of standing up phase, (**iv**) completion of the standing phase (Vericat et al., 2010).

6.2 Factors affecting SAM formation

Several experimental factors need to be controlled during the formation of SAMs by the solution phase method. These factors include the cleanliness of the substrate (Hoogvliet et al., 2000), solvent used during assembly (Dannenberger et al., 1998), incubation temperature and immersion time (Chen et al., 2000a; Kim et al., 1993; Yamada et al., 2000), concentration and nature of the absorbate (Kim et al., 1993), the chain length (Vericat et al., 2006) and the presence of oxygen (Lee et al., 1998).

Cleanliness and crystallinity of the substrate plays an important role in determining the compactness of the monolayer, as bare metal tends to absorb organic substances which results in monolayer defects (Creager et al., 1992; Guo et al., 1994; Lee et al., 1998; Ron and Rubinstein, 1998; Tsuneda et al., 1999; Yang et al., 1995). Well-defined, smooth substrates like Au (111) bind alkanethiols stronger than Au (100), which results in higher SAM density

and regularity (Hou et al., 1998; Lee et al., 1998). For smoother substrates, the density of defects are lower due to fewer grain boundaries, step edges and other surface features that are known to cause defects in SAMs (Leopold and Bowden, 2002).

Various solvents can be used for SAM formation. However, monolayers formed by low polar solvents have poor orientation compared to that formed in high polar solvents such as ethanol (Bain et al., 1989b; Dannenberger et al., 1998; Mamum and Hahn, 2012; Schneider and Buttry, 1993; Yamada et al., 1999). Ethanol is most commonly used for SAM formation. The use of polar solvents other than ethanol (i.e. tetrahydrofuran, dimethylformamide, acetonitrile, cyclooctane, and toluene) form monolayers of similar quality (Bain et al., 1989a). The effects of the solvent on the kinetics of formation and the mechanism of assembly are complex and poorly understood (Schwartz, 2001). The presence of a solvent adds additional parameters to the dynamic equilibrium governing the adsorption of thiols. Solvent-substrate and solvent-adsorbate interactions complicate the thermodynamics and kinetics of assembly (Love et al., 2005). Solvent-substrate interactions can hinder the rate of adsorption of thiols from solution because the solvent molecules must first be displaced from the surface prior to the adsorption of thiols (Love et al., 2005). It has been shown that the rate at which SAMs are formed from alkanethiolates is faster in certain nonpolar solvents (heptane, hexanes) than in ethanol (Dannenberger et al., 1998; Peterlinz and Georgiadis, 1996).

Increasing the reaction temperature results in less monolayer defects, compared to SAMs formed at room temperature (Kang et al., 2010; Korolkov et al., 2010). However, the size of the SAM domain and the vacancy islands are larger and the numbers of vacancy islands are smaller when the temperature of the reaction solution is higher (Mamun and Hahn, 2012; Yamada et al., 2000). Forming SAMs at temperatures above 25 °C can improve the kinetics of formation and reduce the number of defects in them (Kawasaki et al., 2000; Yamada et al., 2000). Elevated temperatures increases the rate of SAM desorption allowing for chain reorganization and lateral rearrangements (Mamun and Hahn, 2012).

A reaction solution with a lower concentration requires longer immersion time for complete formation. Low concentrations and longer immersion time results in more regular SAMs, compared to high concentrations and shorter immersion times (Bain et al., 1989b; Bensebaa et al., 1997). Dense coverage of absorbates occurs fast, but the reorganization process requires time to maximize the density of molecules and minimize the defects in the

SAM. Formation of well-assembled monolayers also depends on the purity of the absorbate, as thiolated precursor impurities lack functional head groups and compete with the molecule of interest for available surface binding sites.

Van der Waals forces between the alkyl chains enhance the stability and order of the absorbates. Thus, more alkyl chains in the absorbate [$HS(CH_2)_nX$, where $n \geq 10$] enhances the stability and regularity of the monolayer, whereas short chain lengths results in more molecular disorder (De Groot et al., 2007; Hong and Park, 2001; Nuzzo et al., 1987; Yue et al., 2008). Additionally, the length of the aliphatic chain also significantly influences the rate and extent of oxidation and desorption, as longer alkyl chain SAMs are more susceptible to oxidation (Wang et al., 2003). The presence of oxygen and the absence of light oxidizes thiolates and forms sulfonates ($-SO^{3-}$) and sulfinates ($-SO^{2-}$) which results in desorption of the SAM from the surface (Ron and Rubinstein, 1998; Wang et al., 2003). SAMs formed in the presence of inert gasses, results in the improvement of the SAMs quality (Laibinis et al., 1991; Love et al., 2003). By reducing the concentration of oxygen in the reaction solution, oxidation of the thiols to sulfonates and other oxygenated species can be limited.

7.1 Biosensors

Detection of specific metabolites, nucleic acids, proteins and pathogens are essential in the diagnosis of diseases. Infectious diseases are responsible for approximately 40 % of the 50 million deaths recorded world-wide (Ivnitski et al., 1999). Waterborne pathogens cause 10-20 million of these deaths. Per annum more than 200 million people suffer from non-fatal infections. Many of these cases could have been treated if the diagnosis had been made sooner. With the advances in nanotechnology, it should be possible to develop a rapid, sensitive and portable, but power-efficient and low cost biosensor.

The detection of biological and chemical species at their earliest stage has become ever important (Liu et al., 2008b). The early detection of these compounds is essential for early response. The established methods for detecting biological species require radioactive material (Wolf et al., 1987), biotin (McInnes et al., 1989), digoxigen (Girotti et al., 1991), fluorescent dye (Abel et al., 1996; Chehab and Kan, 1989), labelled probes, and large quantities of probe and analyte molecules. These methods are cumbersome and are unable to achieve a rapid detection at low levels of concentration. Portable, reliable, and cost effective

bioelectronics systems are in demand to overcome the draw backs of conventional approaches (Liu et al., 2008b).

A schematic representation of the principle of a biosensor shown in Fig. 15, indicates that sensing biomolecules need to be integrated into the system on a solid support. The type of solid support that holds the sensing biomolecule (receptor) is known as a matrix. A suitable matrix enhances signal transduction and helps to immobilize biomolecules with retained or enhanced activity. The physico-chemical properties of the matrix dictate the method of immobilization and the operational stability of the biosensor (Fransconi et al., 2009). Moreover, the matrix alters the resistance of the biomolecule to various physical and chemical changes, such as pH, temperature and chemical composition changes.

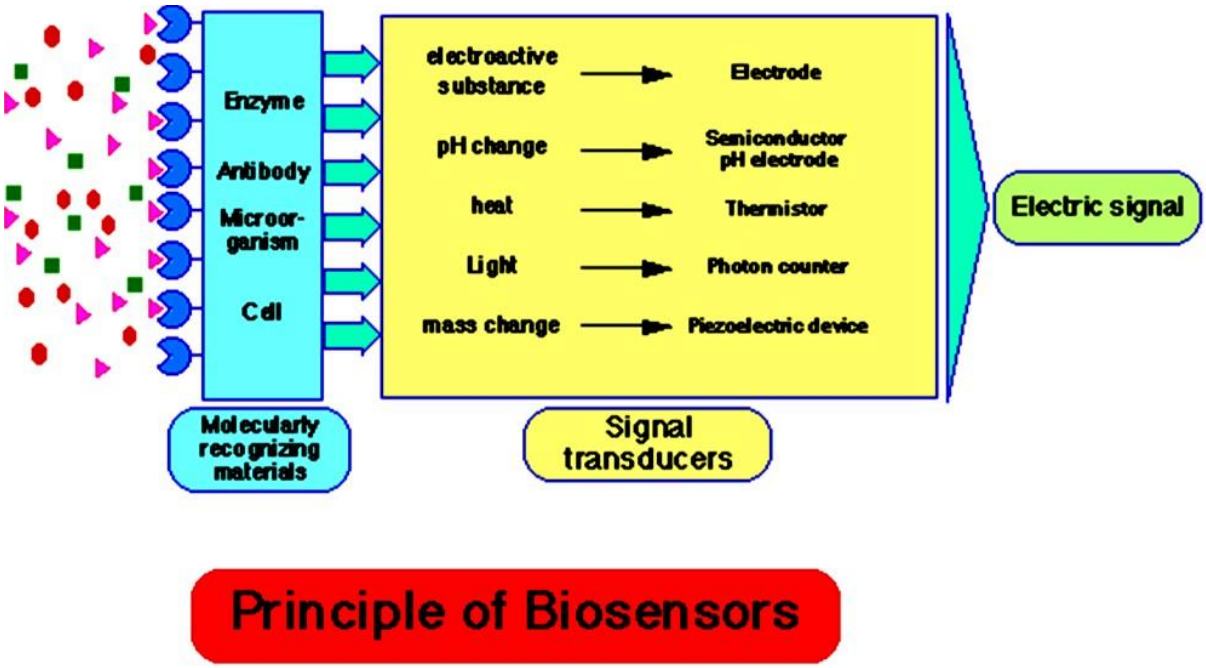

Fig. 15. Schematic diagram of a typical biosensor sensing process (Arya et al., 2012).

The biosensor has to be sensitive enough to provide quantitative, or at least semi-quantitative, data. This means the device has to detect small changes in the concentration of molecules that react with a transducer (Strehlitz et al., 2008). Major developments have been made to increase the performance of biosensors by incorporating various nanostructured material (Ansari et al., 2008; Hrapovic et al., 2004; Lin et al., 2004, Rout et al., 2006; Wang et al., 2008; Zhang et al., 2008).

7.2 ZnO devices developed

ZnO nanostructures have enormous applications in electrochemical, electromechanical and optoelectronic devices, but also as photocatalysts. ZnO electrochemical devices that have been developed include field-effect transistors (FET), gas sensors, pH sensors and humidity sensors. In FETs, the ZnO nanostructures are laterally bonded on a substrate that serves as a gate electrode. Current transported from the drain to the source along the nanowire is controlled by applied gate voltage.

ZnO nanowire field-effect transistors have been developed for sensing of oxygen (Fan et al., 2004), carbon monoxide gas (Khoang et al., 2013), riboflavin (Hagen et al., 2011) and streptavidin (Kim et al., 2006) amongst others. Gas sensors have been developed for the detection of H_2 (Lupan et al., 2007), CO (Wang et al., 2007a), H_2S (Wang et al., 2006a), NH_3 (Wen et al., 2005), CH_4 (Gruber et al., 2003), NO_2 (Fan and Lu, 2005), NO (Farmakis et al., 2008), O_3 (Martins et al., 2004), and O_2 (Li et al., 2004) amongst others.

Gas sensors are divided into reductive or oxidative gas sensors. For reductive gas sensors absorption of gases would results in the release of electrons to the ZnO nanostructures. The gained electrons will increase the carrier concentration, resulting in a thinner depletion layer, and a decrease in the ZnO nanowire resistance (Fig. 16). For oxidative gas sensors the mechanism is opposite, resulting in the release of electrons from the ZnO nanostructures and a thicker depletion layer due to the decrease in the carrier concentration (Fig. 17). A thicker depletion layer results in the increase in resistances of the ZnO nanostructures.

pH sensors using ZnO nanostructures have also been developed. Exposure to electrolytic solutions results in the formation of a surface charge which alters the ZnO nanostructure conductive properties (Al-Hilli et al., 2007). ZnO nanostructures have also been proposed as humidity sensors. With the increase in the relative humidity, the resistance of some sensors decreased (Fang et al., 2009; Park et al., 2010; Zhang et al., 2005).

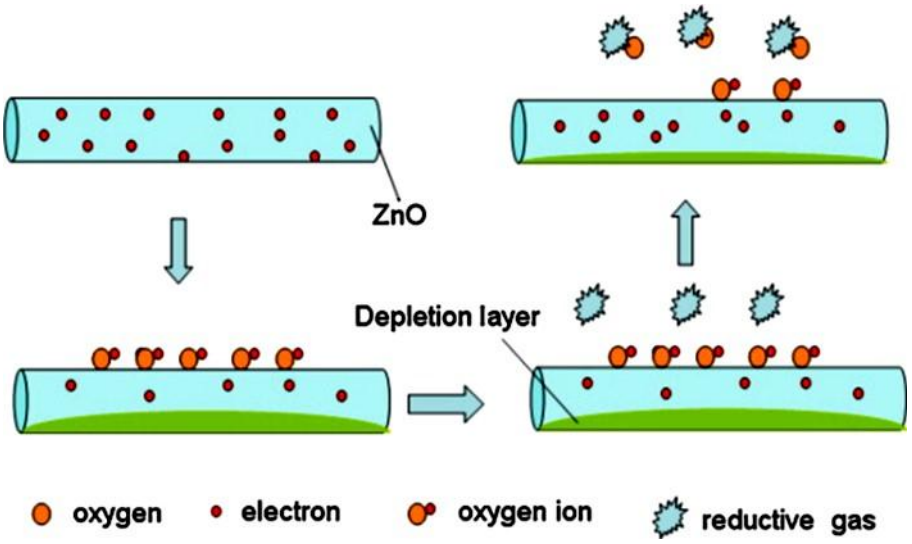

Fig. 16. Schematic diagram of a reductive gas sensor (Wei et al., 2011).

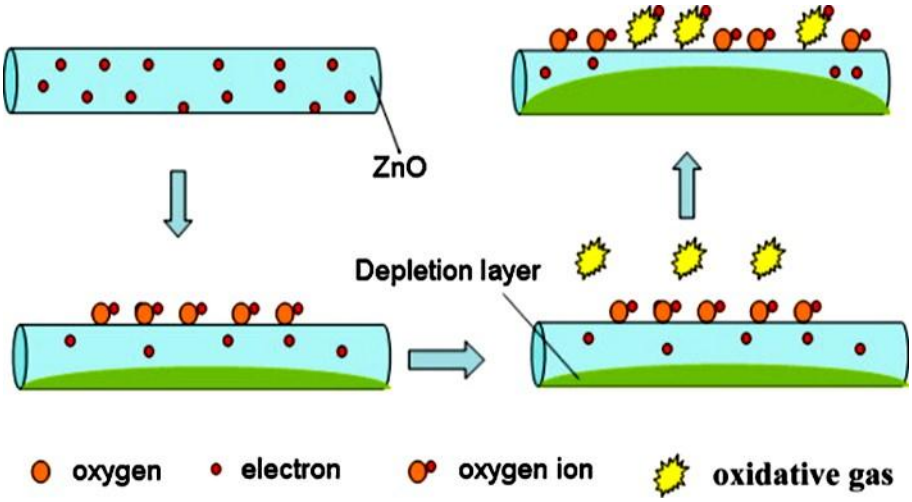

Fig. 17. Schematic diagram of an oxidative gas sensor (Wei et al., 2011).

Electromechanical devices that have been developed include acoustic wave based sensors, nanogenerators, piezoelectric-FETs (PE-FET), and piezodiodes (Lee et al., 2002b). Acoustic wave biosensors are mass sensors which operate with mechanical acoustic waves as their transduction signal (Rocha-Gaso et al., 2009). Interaction at the surface interface causes changes in the acoustic wave properties (i.e. wave propagation, velocity, amplitude, or resonant frequency). Surface acoustic wave (SAW) pressure sensors (Talbi et al., 2006), film bulk acoustic resonators (FBAR) (Chen et al., 2009b) and lateral extensional mode (LEM) piezoelectric resonators (Pang et al., 2006) based on ZnO nanostructures have been used to detect changes in mass or pressure. Electroacoustic devices used in biosensors are based on the detection of a change of mass density, elastic, viscoelastic, electric, or dielectric

properties of a membrane made of chemically interactive materials in contact with a piezoelectric material. A schematic representation of a surface acoustic wave sensor is shown in Fig. 18.

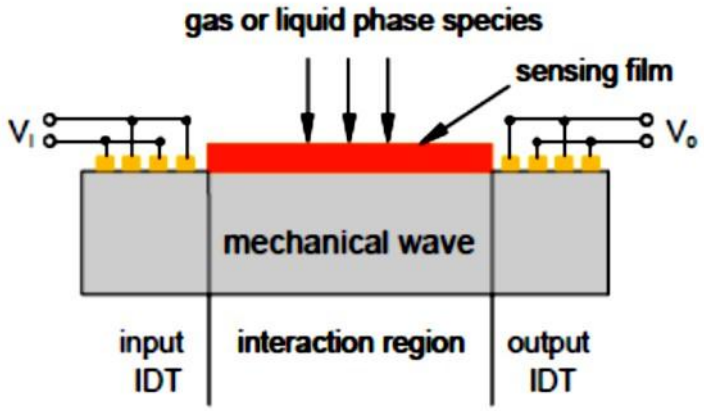

Fig. 18. Schematic representation of a surface generated acoustic wave sensor (Rocha-Gaso et al., 2009).

Nanogenerators have been developed by utilizing the piezoelectric effect of ZnO nanowires (Chang et al., 2010; Wang and Song, 2006; Wang et al., 2007b; Xu et al., 2010). The combination of the piezoelectric and semiconducting properties of ZnO, and the gating effect of a Schottky barrier, transforms the mechanical displacement to an electrical signal. Piezoelectric-FET (PE-FET) has been developed by coupling the semiconductive and piezoelectric properties of ZnO, which is defined as the piezotronic effect (Gao et al., 2009; Kwon et al., 2008; Wang et al., 2006b). The working principle of PE-FET relies on the piezoelectric potential of the nanowire under straining and serves as the gate voltage for controlling the current flow from the drain to source (Fei et al., 2009; Wang et al., 2006a).

Optoelectronic devices with ZnO nanostructures as transducers are UV detectors, UV lasers (Huang et al., 2001a), solar cells and field emission devices. UV detectors rely on changes in electric potential of the ZnO nanostructures when irradiated with UV (Bai et al., 2011; Chen et al., 2009a; Fang et al., 2009; Lu et al., 2009). ZnO nanostructure-based light emitting diodes (LEDs) have also been developed (Chen et al., 2011; Djurišić et al., 2010; Hsu et al., 2008; Sadaf et al., 2011; Willander et al., 2009; Yang et al., 2008). ZnO-based dye-sensitized solar cells (DSSCs) have been developed using ZnO nanostructures which transports electrons fasters, with less recombination loss (Law et al., 2005). ZnO

nanostructures are also considered good candidates for field emitters due to their high melting point and high stability under oxygen environments (Hwang et al., 2011; Zhao et al., 2011).

ZnO nanostructures as photocatalysts have been reported (Kenanakis and Katsarakis, 2010; Ma et al., 2011; Sugunan et al., 2010), and exhibit high photocatalytic efficiency for dye degradation (Hariharan, 2006). Photocatalytic dye degradation by ZnO occurs due to the production of charge transferred photogenerated carriers and reactive oxygen species (ROS) due to UV illumination of the nanostructures (Guo et al., 2011). Photocatalysis utilizes semiconductor photocatalysts to carry out a photo-induced oxidation process to break down organic contaminants and inactivate bacteria and viruses (Fig. 19). When photons with energies greater than the band gap energy of the photocatalyst are absorbed, the valence band (VB) electrons are excited to the conduction band to facilitate a number of possible photoreactions. The photocatalytic surface with sufficient photo energy leads to the formation of a positive hole (h^+) in the valence band and an electron (e^+) in the conduction band (CB) (Zhang et al., 2012). The positive hole could either oxidize organic contaminants directly or produce very reactive hydroxyl radicals (OH^-) which acts as the primary oxidants in the photocatalytic system, which oxidizes the organic compounds (Zhang et al., 2012).

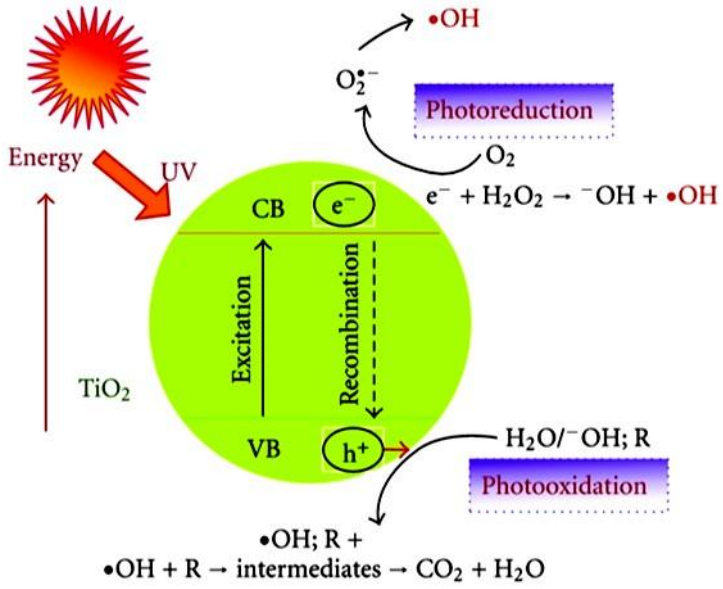

Fig. 19. A schematic representation of the principle of photocatalysis (Ahmed et al., 2010).

References

Abel, A.P., Weller, M.G., Duveneck, G.L., Ehrat, M., Widmer, H.M., 1996. Fiber-optic evanescent wave biosensor for the detection of oligonucleotides. Anal. Chem. 68(17), 2905-2912.

Ahmad, M., Zhu, J., 2011. ZnO based advanced functional nanostructures: synthesis, properties and applications. J. Mater. Chem. 21, 599-614.

Ahmed, S., Rasul, M.G., Martens, W.N., Brown, R., Hashib, M.A., 2010. Heterogeneous photocatalytic degradation of phenols in wastewater: a review on current status and development. Desalination 261(1-2), 3-18.

Al-Hilli, S.M., Willander, M., Öst, A., Stralfors, P., 2007. ZnO nanorods as an intracellular sensor for pH measurements. J. Appl. Phys. 102, 084304.

Ansari, A.A., Solanki, P.R., Malhotra, D.B., 2008. Sol-gel derived nanostructured cerium oxide film for glucose sensor. Appl. Phys. Lett. 92, 263901-263903.

Ardakani, H.G., 1996. Electrical conductivity of in situ "hydrogen-reduced" and structural properties of zinc oxide thin films deposited in different ambients by pulsed excimer laser ablation. Thin Solid Films 287, 280-283.

Arya, S.K., Saha, S., Ramirez-Vick, J.E., Gupta, V., Bhansali, S., Singh, S.P., 2012. Recent advances in ZnO nanostructures and thin films for biosensor applications: Review. Analytica Chimica Acta 737, 1-21.

Ashraf, S., Jones, A.C., Bacsa, J., Steiner, A., Chalker, P.R., Beahan, P., Hindley, S., Odedra, R., Williams, P.A., Heys, P.N., 2011. MOCVD of vertically aligned ZnO nanowires using bidentate ether adducts of dimethylzinc. Chemical Vapor Deposition 17(1-3), 45-53.

Ayouchi, R., Martin, F., Leinen, D., Ramos-Barrado, J.R., 2003. Growth of pure ZnO thin films prepared by chemical spray pyrolysis on silicon. J. Cryst. Growth 247(3-4), 497-504.

Bai, S., Wu, S., 2011. Synthesis of ZnO nanowires by the hydrothermal method, using the sol-gel prepared ZnO seed films. J. Mater. Sci: Mater. Electron. 22(4), 339-344.

Bai, S., Wu, W., Qin, Y., Cui, N., Bayerl, D.J., Wang, X., 2011. High-performance integrated ZnO nanowire UV sensors on rigid and flexible substrates. Adv. Funct. Mater. 21, 4464-4469.

Bain, C.D., Evall, J., Whitesides, G.M., 1989a. Formation of monolayers by the coadsorption of thiols on gold: variation in the head group, tail group, and solvent. J. Am. Chem. Soc. 111(18), 7155-7164.

Bain, C.D., Troughton, E.B., Tao, Y.T., Evall, J., Whitesides, G.M., Nuzzo, R.G., 1989b. Formation of monolayer films by the spontaneous assembly of organic thiols from solution onto gold. J. Am. Chem. Soc. 111(1), 321-335.

Baruah, S., Dutta, J., 2009. Hydrothermal growth of ZnO nanostructures. Sci. Technol. Adv. Mater. 10, 013001.

Bensebaa, F., Voicu, R., Huron, L., Ellis, T.H., Kruus, E., 1997. Kinetics of formation of long-chain n-alkanethiolate monolayers on polycrystalline gold. Langmuir 13(20), 5335-5340.

Biebuyck, H.A., Bain, C.D., Whitesides, G.M., 1994. Comparison of organic monolayers on polycrystalline gold spontaneously assembled from solutions containing dialkyl disulfides or alkanethiols. Langmuir 10(6), 1825–1833.

Brinkley, M., 1992. A brief survey of methods for preparing protein conjugate with dyes, haptens and crosslinking reagents. Bioconjugate Chem. 3(1), 2–13.

Butler, J.E., 2000. Solid supports in enzyme-linked immunosorbent assay and other solid-phase immunoassays. Methods 22(1), 4-23.

Chang, C., Tran, V.H., Wang, J., Fuh, Y., Lin, L., 2010. Direct-write piezoelectric polymeric nanogenerators with high energy conversion efficiency. Nano Lett. 10, 726-731.

Chang, P., Fan, Z., Tseng, W., Wang, D., Chiou, W., Hong, J., Lu, J.G., 2004. ZnO nanowires synthesized by vapor trapping CVD method. Chem. Mater. 16(24), 5133-5137.

Chehab, F.F., Kan, Y.W., 1989. Detection of specific DNA sequences by fluorescence amplification: A color complementation assay. Proc. Natl. Acad. Sci. USA 86(23), 9178-9182.

Chen, K.J., Hung, F.Y., Chang, S.J., Young, S.J., 2009a. Optoelectronic characteristics of UV photodetector based on ZnO nanowire thin films. J. Alloys Compd. 479, 674-677.

Chen, S., Li, L., Boozer, C.L., Jiang, S., 2000a. Controlled chemical and structural properties of mixed self-assembled monolayers of alkanethiols on Au(111). Langmuir 16(24), 9287-9293.

Chen, X., Ng, A.M.C., Fang, F., Ng, Y.H., Djurišić, A.B., Tam, H.L., Cheah, K.W., Gwo, S., Chan, W.K., Fong, P.W.K., Lui, H.F., Surya, C., 2011. ZnO nanorod/GaN light-emitting diodes: The origin of yellow and violet emission bands under reverse and forward bias. J. Appl. Phys. 110, 094513.

Chen, Y., Bagnall, D., Yao, T., 2000b. ZnO as a novel photonic material for the UV region. Mater. Sci. Eng.: B 75(2-3), 190-198.

Chen, Y., Reyes, P.I., Duan, Z., Saraf, G., Wittstruck, R., Lu, Y., Taratula, O, Galoppini, E., 2009b. Multifunctional ZnO-based thin-film bulk acoustic resonator for biosensors. J. Electron. Mater. 38, 1605-1611.

Cheung, C.L., Camarero, J.A., Woods, B.W., Lin, T., Johnson, J.E., De Yoreo, J.J., 2003. Fabrication of assembled virus nanostructures on templates of chemoselective linkers formed by scanning probe nanolithography. J. Am. Chem. Soc. 125(23), 6848-6849.

Choi, J.H., Tabata H., Kawai, T., 2001. Initial preferred growth in zinc oxide thin films on Si and amorphous substrates by a pulsed laser deposition. J. Cryst. Growth 226(4), 493-500.

Creager, S.E., Hocket, L.A., Rowe, G.K., 1992. Consequences of microscopic surface roughness for molecular self-assembly. Langmuir 8(3), 854-861.

Cui, J.B., Daghlian, C.P., Gibson, U.J., Püsche, R., Geithner, P., Ley, L., 2005. Low-temperature growth and field emission of ZnO nanowire arrays. J. Appl. Phys. 97(4), 044315.

Dalal, S.H., Baptista, D.L., Teo, K.B.K., Lacerda, R.G., Jefferson, D.A., Milne, W.I., 2006. Controllable growth of vertically aligned zinc oxide nanowires using vapour deposition. Nanotechnol. 17(19), 4811-4818.

Dannenberger, O., Wolff, J.J., Buck, M., 1998. Solvent dependence of the self-assembly process of an endgroup-modified alkanethiol. Langmuir 14(17), 4679-4682.

De Groot, M.T., Evers, T.H., Merkx, M., Koper, M.T.M., 2007. Electron transfer and ligand binding to cytochrome c immobilized on self-assembled monolayers. Langmuir 23(2), 729-736.

De la Olvera, M.L., Maldonado, A., Asomoza, R., Konagai, M., Asomoza, M., 1993. Growth of textured ZnO: In thin films by chemical spray deposition. Thin Solid Films 229(2), 196-200.

Djurišić, A.B., Ng, A.M.C., Chen, X.Y., 2010. ZnO nanostructures for optoelectronics: Material properties and device applications. Prog. Quantum Electron. 34, 191-259.

Dubois, L.H., Nuzzo, R.G., 1992. Synthesis, structure, and properties of model organic surfaces. Annu. Rev. Phys. Chem. 43, 437–463.

Ducker, R.E., Montague, M.T., Leggett, G.J., 2008. A comparative investigation of methods for protein immobilization on self-assembled monolayers using glutaraldehyde, carbodiimide, and anhydride reagents. Biointerphases 3(3), 59–65.

Emanetoglu, N.W., Gorla, C., Liu, Y., Liang, S., Lu, Y., 1999. Epitaxial ZnO piezoelectric thin films for saw filters. Mater. Sci. Semicond. Process. 2(3), 247-252.

Erdélyi, R., Nagata, T., Rogers, D.J., Teherani, F.H., Horváth, Z.E., Lábadi, Z., Baji, Z., Wakayama, Y., Volk, J., 2011. Investigations into the impact of the template layer on ZnO nanowire arrays made using low temperature wet chemical growth. Cryst. Growth Des. 11(6), 2515-2519.

Fan, Z.Y., Lu, J.G., 2005. Gate-refreshable nanowire chemical sensors. Appl. Phys. Lett. 86(12), 123510.

Fan, Z.Y., Wang, D.W., Chang, P.C., Tseng, W.Y., Lu, J.G., 2004. ZnO nanowire field-effect transistor and oxygen sensing property. Appl. Phys. Lett. 85, 5923.

Fang, F., Futter, J., Markwitz, A., Kennedy, J., 2009. UV and humidity sensing properties of ZnO nanorods prepared by the arc discharge method. Nanotechnology 20(24), 245502.

Fang, Y., Pang, Q., Wen, X., Wang, J., Yang, S., 2006. Synthesis of ultrathin ZnO nanofibers aligned on a zinc substrate. Small 2, 612-615.

Farmakis, F.V., Speliotis, T., Alexandrou, K.P., Tsamis, C., Kompitsas, M., Fasaki, I., Jedrasik, P., Petersson, G., Nilsson, B., 2008. Field-effect transistors with thin ZnO as active layer for gas sensor applications. Microelectron. Eng. 85, 1035-1038.

Fei, P., Yeh, P., Zhou, J., Xu, S., Gao, Y., Song, J., Gu, Y., Huang, Y., Wang, Z.L., 2009. Piezoelectric potential gated field-effect transistor based on a free-standing ZnO wire. Nano Lett. 9, 3435-3439.

Ferrero, V.E.V., Andolfi, L., Di Nardo, G., Sadeghi, S.J., Fantuzzi, A., Cannistraro, S., Gilardi, G., 2008. Protein and electrode engineering for the covalent immobilization of P450 BMP on gold. Anal. Chem. 80(22), 8438-8446.

Flink, S., van Veggel, F.C.J.M., Reinhoudt, D.N., 2000. Sensor functionalities in self-assembled monolayers. Adv. Mater. 12(18), 1315-1328.

Fransconi, M., Mazzei, F., Ferri, T., 2010. Protein immobilization at gold-thiol surfaces and potential for biosensing. Anal. Bioanal. Chem. 398, 1545-1564.

Frasconi, M., Favero, G., Di Fusco, M., Mazzei, F., 2009. Polyazetidine-based immobilization of redox proteins for electron-transfer-based biosensors. Biosens. Bioelectron. 24(5), 1424-1430.

Gao, P.X., Ding, Y., Mai, W., Hughes, W.L., Lao, C., Wang, Z.L., 2005. Conversion of zinc oxide nanobelts into superlattice-structured nanohelices. Science 309, 1700-1704.

Gao, P.X., Ding, Y., Wang, Z.L., 2003. Crystallographic orientation-aligned ZnO nanorods grown by a tin catalyst. Nano Lett. 3(9), 1315-1320.

Gao, Z., Zhou, J., Gu, Y., Fei, P., Hao, Y., Bao, G., Wang, Z.L., 2009. Effects of piezoelectric potential on the transport characteristics of metal-ZnO nanowire-metal field effect transistor. J. Appl. Phys. 105, 113707.

Ghosh, R., Dutta, M., Basak, D., 2007. Self-seeded growth and ultraviolet photoresponse properties of ZnO nanowire arrays. Appl. Phys. Lett. 91(7), 073108.

Girotti, S., Ferri, E., Ghini, S., Musiani, M., Zerbini, M.L., Gibellini, D., Gentilomi, G., 1991. Direct quantitative chemiluminescent assays for the detection of viral DNA. Analytica Chimica Acta 255(2), 387-394.

Gobi, K.V., Iwasaka, H., Miura, N., 2007. Self-assembled PEG monolayer based SPR immunosensor for label-free detection of insulin. Biosens. Bioelectron. 22(7), 1382–1389.

Godin, M., Williams, P.J., Tobard-Cossa, V., Laroche, O., Beaulieu, L.Y., Lennox, R.B., Grütter, P., 2004. Surface stress, kinetics, and structure of alkanethiol self-assembled monolayers. Langmuir 20(17), 7090-7096.

Gooding, J.J., Hibbert, D.B., 1999. The application of alkanethiol self-assembled monolayers to enzyme electrodes. Trends in Analytical Chem. 18(8), 525-533.

Gooding, J.J., Mearns, F., Yang, W., Liu, J., 2003. Self-assembled monolayers into the 21st century: recent advances and applications. Electroanalysis 15(2), 81-96.

Govender, K., Boyle, D.S., Kenway, P.B., O'Brien, P.J., 2004. Understanding the factors that govern the deposition and morphology of thin films of ZnO from aqueous solution. J. Mater. Chem. 14, 2575-2591.

Greene, L.E., Yuhas, B.D., Law, M., Zitoun, D., Yang, P.D., 2006. Solution-grown zinc oxide nanowires. Inorg. Chem. 45(19), 7535-7543.

Gruber, D., Kraus, F., Müller, J., 2003. A novel gas sensor design based on $CH_4/H_2/H_2O$ plasma etched ZnO thin films. Sens. Actuators B: Chem. 92, 81-89.

Guo, L., Facci, J.S., McLendon, G., Mosher, R., 1994. Effect of gold topography and surface pretreatment on the self-assembly of alkanethiol monolayers. Langmuir 10(12), 4588-4593.

Guo, M., Diao, P., Cai, S., 2005. Hydrothermal growth of well-aligned ZnO nanorod arrays: Dependence of morphology and alignment ordering upon preparing conditions. J. Solid State Chem. 178(6), 1864-1873.

Guo, M.Y., Ng, A.M.C., Liu, F., Djurišić, A.B., Chan, W.K., 2011. Photocatalytic activity of metal oxides- the role of holes and OH radicals. Appl. Catal. B 107, 150-157.

Hagen, J.A., Kim, S.N., Bayraktaroglu, B., Leedy, K., Chávez, J.L., Kelley-Loughnane, N., Naik, R.R., Stone, M.O., 2011. Biofunctionalized zinc oxide field effect transistors for selective sensing of riboflavin with current modulation. Sensors 11(7), 6645-6655.

Hahn, C.D., Leitner, C., Weinbrenner, T., Schlapak, R., Tinazli, A., Tampe, R., Lackner, B., Steindl, C., Hinterdorfer, P., Gruber, H.J., Holzl, M., 2007. Self-assembled monolayers with latent aldehydes for protein immobilization. Bioconjug. Chem. 18(1), 247–253.

Hariharan, A., 2006. Photocatalytic degradation of organic contaminants in water by ZnO nanoparticles: revisted. Appl. Catal. A 304, 55-61.

Hirano, S., Takeuchi, N., Shimada, S., Masuya, K., Ibe, K., Ysunakawa, H., Kuwubara, M., 2005. Room-temperature nanowire ultraviolet lasers: An aqueous pathway for zinc oxide nanowires with low defect densiy. J. Appl. Phys. 98, 094305.

Hong, H., Park, W., 2001. Electrochemical characteristics of hydroquinone-terminated self-assembled monolayers on gold. Langmuir 17(8), 2485-2492.

Hoogvliet, J.C., Dijksma, M., Kamp, B., van Bennekom, W.P., 2000. Electrochemical pretreatment of polycrystalline gold electrodes to produce a reproducible surface roughness for self-assembly: a study in phosphate buffer pH 7.4. Anal. Chem. 72(9), 2016-2021.

Hou, Z., Abbott, N.L., Stroeve, P., 1998. Electroless gold as a substrate for self-assembled monolayers. Langmuir 14(12), 3287-3297.

Houseman, B.T., Gawalt, E.S., Mrksich, M., 2003. Maleimide-functionalized self-assembled monolayers for the preparation of peptide and carbohydrate biochips. Langmuir 19(5), 1522–1529.

Hrapovic, S., Liu, Y., Male, K.B., Luong, J.H.T., 2004. Electrochemical biosensing platforms using platinum nanoparticles and carbon nanotubes. Anal. Chem. 76, 1083-1088.

Hsu, Y.F., Xi, Y.Y., Tam, K.H., Djurišić, A.B., Luo, J., Ling, C.C., Cheung, C.K., Ng, A.M.C., Chan, W.K., Deng, X., Beling, C.D., Fung, S., Cheah, K.W., Fong, P.W.K., Surya, C.C., 2008. Undoped p-type ZnO nanorods synthesized by a hydrothermal method. Adv. Funct. Mater. 18, 1020-1030.

Hu, J., Gordon, R.G., 1992. Textured aluminium-doped zinc oxide thin films from atmospheric pressure chemical-vapor deposition. J. Appl. Phys. 71(2), 880-891.

Hu, J.T., Odom, T.W., Lieber, C.M., 1999. Chemistry and physics in one dimension: Synthesis and properties of nanowires and nanotubes. Acc. Chem. Res. 32(5), 435-445.

Huang, H., Mao, S., Feick, H., Yan, H., Wu, Y., Kind, H., Tran, N., Weber, E., Ruso, R., Yang, P., 2001a. Room-temperature ultraviolet nanowire nanolasers. Science 292(5523), 1897.

Huang, M.H., Wu, Y., Feick, H., Tran, N., Weber, E., Yang, P., 2001b. Catalytic growth of zinc oxide nanowires by vapour transport. Adv. Mater. 13(2), 113-116.

Hughes, W.L., Wang, Z.L., 2004. Formation of piezoelectric single-crystal nanorings and nanobows. J. Am. Chem. Soc. 126(21), 6703-6709.

Hwang, J.O., Lee, D.H., Kim, J.Y., Han, T.H., Kim, B.H., Park, M., No, K., Kim, S.O., 2011. Vertical ZnO nanowires/grapheme hybrids for transparent and flexible field emission. J. Mater. Chem. 21, 3432-3437.

Ivnitski, D., Abdel-Hamid, I., Atanasov, P., Wilkins, E., 1999. Biosensors for detection of pathogenic bacteria. Biosens. Bioelectron. 14(7), 599-624.

Johnson, D.L., Martin, L.L.J., 2005. Controlling protein orientation at interfaces using histidine tags: An alternative to Ni/NTA. J. Am. Chem. Soc. 127(7), 2018–2019.

Jonkheijm, P., Weinrich, D., Schröder, H., Niemeyer, C.M., Waldmann, H., 2008. Chemical strategies for generating protein biochips. Angew. Chem. Int. Ed. 47(50), 9618-9647.

Jung, C., Dannenberger, O., Xu, Y., Buck, M., Grunze, M., 1998. Self-assembled monolayers from organosulfur compounds: A comparison between sulphides, disulfides, and thiols. Langmuir 14(5), 1103–1107.

Kang, H., Lee, N., Ito, E., Hara, M., Noh, J., 2010. Formation and superlattice of long-range-ordered self-assembled monolayers of pentafluorobenzenethiols on Au(111). Langmuir 26(5), 2983-2985.

Karyakin, A.A., Presnova, G.V., Rubtsova, M.Y., Egorov, A.M., 2000. Oriented immobilization of antibodies onto the gold surfaces via their native thiol groups. Anal. Chem. 72(16), 3805–3811.

Kawasaki, M., Sato, T., Tanaka, T., Takao, K., 2000. Rapid self-assembly of alkanethiol monolayers on sputter-grown Au(111). Langmuir 16(4), 1719-1728.

Kenanakis, G., Katsarakis, N., 2010. Light-induced photocatalytic degradation of stearic acid by c-axis oriented ZnO nanowires. Appl. Catal. A: Gen. 378(2), 227-233.

Kenanakis, G., Vernardou, D., Koudoumas, E., Katsarakis, N., 2009. Growth of c-axis oriented ZnO nanowires from aqueous solution: The decisive role of a seed layer for controlling the wires' diameter. J. Crystal Growth 311(23-24), 4799-4804.

Khan, F., He, M., Taussig, M.J., 2006. Double-hexahistidine tag with high-affinity binding for protein immobilization, purification, and detection on Ni-Nitrilotriacetic acid surfaces. Anal. Chem. 78(9), 3072-3079.

Khoang, N.D., Hong, H.S., Trung, D.D., Duy, N.V., Hoa, N.D., Thinh, D.D., Hieu, N.V., 2013. On-chip growth of wafer-scale planar-type ZnO nanorod sensors for effective detection of CO gas. Sensors Actuat. B: Chem. 181, 529-536.

Kim, J., Cho, J., Seidler, P.M., Kurland, N.E., Yadavalli, V.K., 2010. Investigations of chemical modifications of amino-terminated organic films on silicon substrates and controlled protein immobilization. Langmuir 26(4), 2599-2608.

Kim, J.S., Park, W.I., Lee, C.H., Yi, G.C., 2006. ZnO nanorod biosensor for highly sensitive detection of specific protein binding. J. Korean Phys. Soc. 49, 1635-1639.

Kim, S.W., Fujita, Sz., Fujita, Sg., 2003. Self-organized ZnO quantum dots on SiO_2/Si substrates by metalorganic chemical vapour deposition. Appl. Phys. Lett. 81, 5036-5038.

Kim, Y.T., McCarley, R.L., Bard, A.J., 1993. Observation of n-octadecanethiol multilayer formation from solution onto gold. Langmuir 9(8), 1941-1944.

Kitamura, K., Yatsui, T., Ohtsu, M., Yi, G.C., 2008. Fabrication of vertically aligned ultrafine ZnO nanorods using metal-organic vapour phase epitaxy with a two-temperature growth method. Nanotechnology 19(17), 175305.

Kohls, M., Bonnani, M., Spanhel, L., Su, D., Giersig, M., 2002. Green Er^{III} luminescence in fractal ZnO nanolattices. Appl. Phys. Lett. 81, 3858-3860.

Kong, X.Y., Wang, Z.L., 2003. Spontaneous polarization-induced nanohelixes, nanosprings, and nanorings of piezoelectric nanobelts. Nano Lett. 3(12), 1625-1631.

Korolkov, V.V., Allen, S., Roberts, C.J., Tendler, S.J.B., 2010. Subsecond self-assembled monolayer formation. J. Phys. Chem. C. 114(45), 19373-19377.

Krunks, M., Mellikov, E., 1995. Zinc oxide thin films by the spray pyrolysis method. Thin Solid Films 270(1-2), 33-36.

Kusnezow, W., Hoheisel, J.D., 2003. Solid supports for microarray immunoassays. J. Mol. Recognit. 16(4), 165-176.

Kwon, S., Hong, W., Jo, G., Maeng, J., Kim, T., Song, S., Lee, T., 2008. Piezoelectric effect on the electronic transport characteristics of ZnO nanowire field-effect transistors on bent flexible substrates. Adv. Mater. 20, 4557-4562.

Lagashetty, A., Havanoor, V., Basavaraja, S., Balaji, S.D., Venkataraman, A., 2007. Microwave-assisted route for synthesis of nanosized metal oxides. Sci. Technol. Adv. Mater. 8(6), 484-493.

Laibinis, P.E., Whitesides, G.M., Allara, D.L., Tao, Y.T., Parikh, A.N., Nuzzo, R.G., 1991. Comparison of the structures and wetting properties of self-assembled monolayers of n-alkanethiols on the coinage metal surfaces, copper, silver, and gold. J. Am. Chem. Soc. 113(19), 7152-7167.

Lao, J.Y., Huang, J.Y., Wang, D.Z., Ren, Z.F., 2003. ZnO nanobridges and nanonails. Nano. Lett. 3(2), 235-238.

Law, M., Greene, L.E., Johnson, J.C., Saykally, R., Yang, P., 2005. Nanowire dye-sensitized solar cells. Nat. Mat. 4, 455-459.

Lee, C.J., Lee, T.J., Lyu, S.C., Zhang, Y., Ruh, H., Lee, H.J., 2002a. Field emission from well-aligned zinc oxide nanowires grown at low temperature. Appl. Phys. Lett. 81, 3648-3650.

Lee, J.Y., Choi, Y.S., Kim, J.H., Park, M.O., Im, S., 2002b. Optimizing n-ZnO/p-Si heterojunctions for photodiode applications. Thin Solid Films 403-404, 533-557.

Lee, M., Hsueh, C., Freund, M.S., Ferguson, G.S., 1998. Air oxidation of self-assembled monolayers on polycrystalline gold: the role of the gold substrate. Langmuir 14(22), 6419-6423.

Leopold, M.C., Bowden, E.F., 2002. Influence of gold substrate topography on the voltammetry of cytochrome c absorbed on carboxylic acid terminated self-assembled monolayers. Langmuir 18(6), 2239-2245.

Leung, Y.H., Tam, K.H., Djurišić, A.B., Xie, M.H., Chan, W.K., Lu, D., Ge, W.K., 2005. ZnO nanoshells: Synthesis, structure, and optical properties. J. Cryst. Growth 283(1-2), 134-140.

Li, B., Zeng, C., Li, Q., Wang, B., Yuan, L., Wang, H., Yang, J., Hou, J.G., Zhu, Q., 2003a. First-principle simulation of scanning tunnelling microscopy images of individual molecules in alkanethiol self-assembled monolayers on Au(111). J. Phys. Chem. B 107(4), 972–984.

Li, J., Zhang, Q., Peng, H., Everitt, H.O., Qin, L., Liu, J., 2009. Diameter-controlled vapour-solid epitaxial growth and properties of aligned ZnO nanowire arrays. J. Phys. Chem. C 113(10), 3950-3954.

Li, Q., Kumar, V., Li, Y., Zhang, H., Marks, T.J., Chang, R.P.H., 2005. Fabrication of ZnO nanorods and nanotubes in aqueous solutions. Chem. Mater. 17(5), 1001-1006.

Li, Q.H., Liang, Y.X., Wan, Q., Wang, T.H., 2004. Oxygen sensing characteristics of individual ZnO nanowire transistors. Appl. Phys. Lett. 85, 6389-6391.

Li, S.Y., Lee, C.Y., Tseng, T.Y., 2003b. Copper-catalyzed ZnO nanowires on silicon (100) grown by vapour-liquid-solid process. J. Cryst. Growth 247(3-4), 357-362.

Li, Y., Huang, J., McIver Jr, R.T., Hemminger, J.C., 1992. Characterization of thiol self-assembled films by laser desorption Fourier transform mass spectroscopy. J. Am. Chem. Soc. 114(7), 2428-2432.

Li, Z., Yang, R., Yu, M., Bai, F., Li, C., Wang, Z.L., 2008. Cellular level biocompatibility and biosafety of ZnO nanowires. J. Phys. Chem. C 112(51), 20114-20117.

Li, Z.W., Gao, W., 2007. Growth of zinc oxide thin films and nanostructures by wet oxidation. Thin Solid Films 515(7-8), 3323-3329.

Liang, S., Sheng, H., Liu, Y., Hio, Z., Lu, Y., Chen, H., 2001. ZnO Schottky ultraviolet photodetectors. J. Cryst. Growth 225(2-4), 110-113.

Lin, Y., Lu, F., Tu, Y., Ren, Z., 2004. Glucose biosensors based on carbon nanotube nanoelectrode ensembles. Nano Lett. 4, 191-195.

Liu, B., Zeng, H.C., 2003. Hydrothermal synthesis of ZnO nanorods in the diameter regime of 50 nm. J. Am. Chem. Soc. 125(15), 4430-4431.

Liu, C., Zapien, J.A., Yao, Y., Meng, X., Lee, C.S., Fan, S., Lifshitz, Y., Lee, S.T., 2003. High-density, ordered ultraviolet light-emitting ZnO nanowire arrays. Adv. Mater. 15(10), 838-841.

Liu, J., Fei, P., Zhou, J., Tummala, R., Wang, Z.L., 2008a. Toward high output-power nanogenerators. Appl. Phys. Lett. 9(17), 2173105.

Liu, J., Goud, J., Raj, M., Iyer, M., Wang, Z.L., Tummala, R.R., 2008b. Real-time protein detection using ZnO nanowire/thin film bio-sensor integrated with microfluidic system. Electric Components and Technology Conference 2008, 1317-1322.

Liu, J., Row, M.N.P., Gooding, J.J., 2006. Surface reconstitution of glucose oxidase onto a norbornylogous bridge self-assembled monolayer. Chem. Phys. 324(1-2), 226–235.

Love, J.C., Estroff, L.A., Kriebel, J.K., Nuzzo, R.G., Whitesides, G.M., 2005. Self-assembled monolayers of thiolates on metals as a form of nanotechnology. Chem. Rev. 105(4), 1103-1170.

Love, J.C., Wolfe, D.B., Haasch, R., Chabinyc, M.L., Paul, K.E., Whitesides, G.M., Nuzzo, R.G., 2003. Formation and structure of self-assembled monolayers of alkanethiolates on palladium. J. Am. Chem. Soc. 125(9), 2597–2604.

Lu, C., Chang, S., Chang, S., Hsueh, T., Hsu, C., Chiou, Y., Chen, I., 2009. A lateral ZnO nanowire UV photodetector prepared on a ZnO:Ga/glass template. Semicond. Sci. Technol. 24(7), 075005.

Lupan, O., Chai, G., Chow, L., 2007. Fabrication of ZnO nanorod-based hydrogen gas nanosensor. Microelectron. J. 38(12), 1211-1216.

Lyu, S.C., Zhang, Y., Lee, C.J., 2003. Low-temperature growth of ZnO nanowire array by a simple physical vapour-deposition method. Chem. Mater. 15(17), 3294-3299.

Lyu, S.C., Zhang, Y., Ruh, H., Lee, H.J., Shim, H.W., Suh, E.K., Lee, C.J., 2002. Low temperature growth and photoluminescence of well-aligned zinc oxide nanowires. Chem. Phys. Lett. 363(1-2), 134-138.

Ma, C., Zhou, Z., Wei, H., Yang, Z., Wang, Z., Zhang, Y., 2011. Rapid large-scale preparation of ZnO nanowires for photocatalytic application. Nanoscale Res. Lett. 6, 536-540.

Ma, X., Zhang, H., Ji, Y., Xu, J., Yang, D., 2005. Sequential occurrence of ZnO nanoparticles, nanorods, and nanotips during hydrothermal process in a dilute aqueous solution. Matter. Lett. 59(27), 3393-3397.

MacBeath, G., Schreiber, S.L., 2000. Printing proteins as microarrays for high-throughput function determination. Science 289, 1760-1764.

Mamun, A.H.A., Hahn, J.R., 2012. Effects of immersion temperature on self-assembled monolayers of octanethiol on Au(111). Surface Science 606(5-6), 664-669.

Martins, R., Fortunato, E., Nunes, P., Ferreira, I., Marques, A., Bender, M., Katsarakis, N., Cimalla, V., Kiriakidis, G., 2004. Zinc oxide as an ozone sensor. J. Appl. Phys. 96(3), 1398-1408.

McInnes, J.L., Habili, L., Symons, R.H., 1989. Nonradioactive, photobiotin-labelled DNA probes for routine diagnosis of viroids in plant extracts. Journal of Virological Methods 23(3), 299-312.

McPeak, K.M., Le, T., Britton, N.G., Nickolov, Z.S., Elabd, Y.A., Baxter, J.B., 2011. Chemical bath deposition of ZnO nanowires at near-neutral pH conditions without hexamethylenetetramine (HMTA): Understanding the role of HMTA in ZnO nanowire growth. Langmuir 27(7), 3672-3677.

Menzel, A., Goldberg, R., Burshtein, G., Lumelsky, V., Subannajui, K., Zacharias, M., Lifshitz, Y., 2012. Role of carrier gas flow and species diffusion in nanowire growth from thermal CVD. J. Phys. Chem. C 116(9), 5524-5530.

Miao, L., Ieda, Y., Tanemura, S., Cao, Y.G., Tanemura, M., Hayashi, Y., Toh, S., Kaneko, K., 2007. Synthesis, microstructure and photoluminescence of well-aligned ZnO nanorods on Si substrate. Sci. Technol. Adv. Mater. 8(6), 443-447.

Mrksich, M., 2005. Dynamic substrates for cell biology. MRS Bull. 30(3), 180-184.

Mrksich, M., 2009. Using self-assembled monolayers to model the extracellular matrix. Acta. Biomater. 5(3), 832–841.

Newton, M.C., Warburton, P.A., 2007. ZnO tetrapod nanocrystals. Mater. Today 10(5), 50-54.

Nishizawa, H., Yuasa, K., 1998. Preparation of highly oriented ZnO thin film under hydrothermal conditions. J. Mater. Sci. Lett. 17(12), 985-987.

Noh, J., Murase, T., Nakajima, K., Lee, H., Hara, M., 2000. Nanoscopic investigation of the self-assembly processes of dialkyl disulfides and dialkyl sulphides on Au (111). J. Phys. Chem. B 104(31), 7411–7418.

Nuzzo, R.G., Zegarski, B.R., Dubois, L.H., 1987. Fundamental studies of the chemisorption of organosulfur compounds on gold(111), implications for molecular self-assembly on gold surfaces. J. Am. Chem. Soc. 109(3), 733-740.

O'Shannessy, D.J., Brigham-Burke, M., Peck, K., 1992. Immobilization chemistries suitable for use in the BIAcore surface plasmon resonance detector. Anal. Biochem. 205, 132–136.

Ohyama, M., Kozuka, H., Yoko, T., 1997. Sol-gel preparation of ZnO films with extremely preferred orientation along (002) plane from zinc acetate solution. Thin Solid Films 306(1), 78-85.

Pal, U., Santiago, P., 2005. Controlling the morphology of ZnO nanostructures in a low-temperature hydrothermal process. J. Phys. Chem. B 109(32), 15317-15321.

Pan, Z.W., Dai, Z.R., Wang, Z.L., 2001. Nanobelts of semiconducting oxides. Science 291, 1947-1949.

Pang, W., Yan, L., Zhang, H., Yu, H., Kim, E.S., Tang, W.C., 2006. Femtogram mass sensing platform based on lateral extensional mode piezoelectric resonator. Appl. Phys. Lett. 88, 243503-243505.

Park, S., Wang, Y., Yeow, J.T.W., Yin, Y., Chen, L., 2010. Humidity sensing characteristics of ZnO nanowires aligned by dielectrophoresis method. Proceedings of 10th IEEE International Conference on Nanotechnology Joint Symposium with Nano Korea, August, 17-20.

Peterlinz, K. A., Georgiadis, R., 1996. In Situ of self-assembly by surface plasmon resonance spectroscopy. Langmuir 12(20), 4731-4740.

Protasova, L.N., Rebrov, E.V., Choy, K.L., Pung, S.Y., Engels, V., Cabaj, M., Wheatley, A.E.H., Schouten, J.C., 2011. ZnO based nanowires grown by chemical vapour deposition for

selective hydrogenation of acetylene alcohols. Catalysis Science and Technology 1(5), 768-777.

Reynolds, N.P., Janusz, S., Escalante-Marun, M., Timney, J., Ducker, R.E., Olsen, J.D., Otto, C., Subramaniam, V., Leggett, G.J., Hunter, C.N., 2007. Directed formation of micro- and nanoscale patterns of functional light-harvesting LH2 complexes. J. Am. Chem. Soc. 129, 14625–14631.

Rocha-Gaso, M., March-Iborra, C., Montoya-Baides, A., Arnau-Vives, A., 2009. Surface generated acoustic wave biosensors for the detection of pathogens: A review. Sensors 9, 5740-5769.

Rodriquez, J.A., Jirsak, T., Dvorak, J., Sambasivan, S., Fischer, D., 2000. Reaction of NO_2 with Zn and ZnO: Photoemission, XANES, and density functional studies on the formation of NO_3. J. Phys. Chem. B 104, 319-328.

Ron, H., Rubinstein, I., 1998. Self-assembled monolayers on oxidized metals, alkylthiol and dialkyl disulphide assembly on gold under electrochemical conditions. J. Am. Chem. Soc. 120(51), 13444-13452.

Rout, C.S., Govindaraj, A., Rao, C.N.R., 2006. High-sensitivity hydrocarbon sensors based on tungsten oxide nanowires. J. Mater. Chem. 16, 3936-3941.

Rusmini, F., Zhong, Z., Feijen, J., 2007. Protein immobilization strategies for protein biochips. Biomacromoleucles 8(6), 1775-1789.

Sadaf, J.R., Israr, M.Q., Kishwar, S., Nur, O., Willander, M., 2011. Forward- and reverse-biased electroluminescence behaviour of chemically fabricated ZnO nanotubes/GaN interface. Semicond. Sci. Technol. 26(7), 075003.

Saito, N., Haneda, H., Sekiguchi, T., Ohashi, N., Sakaguchi, I., Koumoto, K., 2002. Low-temperature fabrication of light-emitting zinc oxide micropatterns using self-assembled monolayers. Adv. Mater. 14(6), 418-421.

Samanta, D., Sarkar, A., 2011. Immobilization of bio-macromolecules on self-assembled monolayers: methods and sensor applications. Chem. Soc. Rev. 40, 2567-2592.

Sarma, A.K., Vatsyayan, P., Goswami, P., Minteer, S.D., 2009. Recent advances in material science for developing enzyme electrodes. Biosens. Bioelectron. 24(8), 2313-2322.

Satoh, Y., Ohshio, S., Saitoh, H., 2005. Photoluminescence spectroscopy of higly oriented Y_2O_3:Tb crystalline whiskers. Sci. Technol. Adv. Mater. 6, 215-218.

Sberveglieri, G., 1995. Recent developments in semiconducting thin-film gas sensors. Sens. Actuator. B 23(2-3), 103-109.

Sberveglieri, G., Groppelli, S., Nelli, P., Tintinelli, A., Giunta, G., 1995. A novel method for the preparation of NH_3 sensors based on ZnO-In thin films. Sens. Actuat. B: Chem. 25(1-3), 588-590.

Schmidt-Mende, L., MacManus-Driscoll, J.L., 2007. ZnO-nanostructures, defects, and devices. Mater. Today 10(5), 40-48.

Schneider, T.W., Buttry, D.A., 1993. Electrochemical quartz crystal microbalance studies of adsorption and desorption of self-assembled monolayers of alkyl thiols on gold. J. Am. Chem. Soc. 115(26), 12391-12397.

Schreiber, F., 2000. Structure and growth of self-assembling monolayers. Prog. Surf. Sci. 65(5-8), 151-257.

Schwartz, D.K., 2001. Mechanisms and kinetics of self-assembled monolayer formation. Annu. Rev. Phys. Chem. 52, 107-137.

Shingubara, S., 2003. Fabrication of nanomaterials using porous alumina templates. J. Nanoparticle Res. 5(1-2), 17-30.

Snure, M., Ashutosh, T., 2007. Synthesis, characterization, and green luminescence in ZnO nanocages. J. Nanosci. Nanotechnol. 7, 481-485.

Song, J., Lim, S., 2007. Effect of seed layer on the growth of ZnO nanorods. J. Phys. Chem. C 111, 596-600.

Song, J., Wang, X., Riedo, E., Wang, Z.L., 2005. Systematic study on experimental conditions for large-scale growth of aligned ZnO nanowires on nitrides. J. Phys. Chem. B 109(20), 9869-9872.

Spanhel, L., 2006. Colloidal ZnO nanostructured and functional coatings: A survey. J. Sol-Gel Sci. Technol. 39(1), 7-24.

Strehlitz, B., Nikolaus, N., Stoltenburg, R., 2008. Protein detection with aptamer biosensors. Sensors 8, 4296–4307.

Subramanian, A., Irudayaraj, J., Ryan, T., 2006a. A mixed self-assembled monolayer-based surface plasmon immunosensor for the detection of *E. coli* O157:H7. Biosens. Bioelectron. 21(7), 998–1006.

Subramanian, A., Irudayaraj, J., Ryan, T., 2006b. Mono and dithiol surface plasmon resonance biosensors for detection of *Staphylococcus aureus*. Sens. Actuators B: Chem. 114(1), 192–198.

Sugunan, A., Guduru, V.K., Uheida, A., Toprak, M.S., Muhammed, M., 2010. Radially oriented ZnO nanowires on flexible poly-L-lactate nanofibers for continuous-flow photocatalytic water purification. J. Am. Ceram. Soc. 93, 3740-3744.

Sugunan, A., Warad, H.C., Bosman, M., Dutta, J., 2006. Zinc oxide nanowires in chemical bath on seeded substrates: Role of hexamine. J. Sol-Gel Sci. Techn. 39(1), 49-56.

Sullivan, T.P., Huck, W.T.S., 2003. Reactions on monolayers: organic synthesis in two dimensions. Eur. J. Org. Chem. 2003(1), 17-29.

Sun, Y., Fuge, G.M., Fox, N.A., Riley, D.J., Ashfold, M.N.R., 2005. Synthesis of aligned arrays of ultrathin ZnO nanotubes on a Si wafer coated with a thin ZnO film. Adv. Mater. 17, 2477-2481.

Sun, Y., Yan, F., Yang, W., Sun, C., 2006. Multilayered construction of glucose oxidase and silica nanoparticles on Au electrodes based on layer-by-layer covalent attachment. Biomaterials 27(21), 4042–4049.

Swamy, H.G., Reddy, P.G., 1990. Preparation of ZnO films by activated reactive evaporation. Semicond. Sci. Technol. 5, 980-981.

Tak, Y., Yong, K., 2005. Controlled growth of well-aligned ZnO nanorod array using a novel solution method. J. Phys. Chem. B 109(41), 19263-19269.

Talbi, A., Sarry, F., Elhakiki, M., Le Brizoual, L., Elmazria, O., Nicolay, P., Alnot, P., 2006. ZnO/quartz structure potentiality for surface acoustic wave pressure sensor. Sensor. Actuat. A: Phys. 128(1), 78-83.

Tian, Z.R., Voigt, J.A., Liu, J., Mekenzie, B., Mcdermott, M.J., 2002. Biomimetric arrays of oriented helical ZnO nanorods and columns. J. Am. Chem. Soc. 124, 12954-12955.

Tien, L.C., Pearton, S.J., Norton, D.P., Ren, F., 2008. Synthesis and microstructure of vertically aligned ZnO nanowires grown by high pressure-assisted pulsed laser deposition. J. Mater. Sci. 43(21), 6925-6932.

Torrelles, X., Vericat, C., Vela, M.E., Fonticelli, M.H., Millone, M.A.D., Felici, R., Lee, T., Zegenhagen, J., Munoz, G., Martin-Gago, J.A., Salvarezza, R.C., 2006. Two-site adsorption model for the –R30˚ dodecanethiolate lattice on Au (111) surfaces. J. Phys. Chem. B 110, 5586 -5594.

Tsang, V.C.W.; Greene, R.M.; Pilcher, J.B.J., 1995. Optimization of the covalent conjugating procedure ($NaIO_4$) of horseradish peroxidase to antibodies for use in enzyme-linked immunosorbent assay. Immunoassay Immunochem. 16(4), 395-418.

Tsuneda, S., Ishida, T., Nishida, N., Hara, M., Sasabe, H., Knoll, W., 1999. Tailoring of a smooth polycrystalline gold surface as a suitable anchoring site for self-assembled monolayer. Thin Solid Films 339(1-2), 142-147.

Ulman, A., 1996. Formation and structure of self-assembled monolayers. Chem. Rev. 96(4), 1533-1554.

Vayssiers, L., Keis, K., Lindquist S., Hagfeldt A., 2001. Purpose-built anisotropic metal oxide material: 3D highly oriented microrod array of ZnO. J. Phys. Chem. B 105(17), 3350.

Vericat, C., Vela, M.E., Benitez, G., Carro, P., Salvarezza, R.C., 2010. Self-assembled monolayers of thiols and dithiols on gold: new challenges for a well-known system. Chem. Soc. Rev. 39, 1805-1834.

Vericat, C., Vela, M.E., Benitez, G.A., Gago, J.A.M., Torrelles, X., Salvarezza, R.C., 2006. Surface characterization of sulphur and alkanethiol self-assembled monolayers on Au(111). J. Phys.: Condens. Matter 18, R687-R900.

Vericat, C., Vela, M.E., Salvarezza, R.C., 2005. Self-assembled monolayers of alkanethiols on Au(111): surface structures, defects and dynamics. Phys. Chem. Chem. Phys. 7, 3258-3268.

Vos, J.G., Forster, R.J., Keyes, T.A., 2003. Interfacial Supramolecular Assemblies, Wiley, New York.

Wang, C., Chu, X., Wu, M., 2006a. Detection of H_2S down to ppb levels at room temperature using sensors based on ZnO nanorods. Sens. Actuators B: Chem. 113(1), 320-323.

Wang, J.M., Gao, L., 2003. Wet chemical synthesis of ultralong and straight single-crystalline ZnO nanowires and their excellent UV emission properties. J. Mater. Chem. 13, 2551-2554.

Wang, J.X., Sun, X.W., Huang, H., Lee, Y.C., Tan, O.K., Yu, M.B., Lo, G.Q., Kwong, D.L., 2007a. A two-step hydrothermally grown ZnO microtube array for CO gas sensing. Appl. Phys. A 88, 611-615.

Wang, L., Tsan, D., Stoeber, B., Walus, K., 2012. Substrate-free fabrication of self-supporting ZnO nanowire arrays. Adv. Mater. 24(29), 3999-4004.

Wang, M., Ye, C., Zhang, Y., Wang, H., Zeng, X., Zhang, L., 2008. Seed-layer controlled synthesis of well aligned ZnO nanowire arrays via a low temperature aqueous solution method. J. Mater. Sci.: Mater. Electron. 19(3), 211-216.

Wang, M.C., Liao, J.D., Weng, C.C., Klauser, R., Shaporenko, A., Grunze, M., Zharnikov, M., 2003. Modification of aliphatic monomolecular films by free radical dominant plasma: the effect of the alkyl chain length and the substrate. Langmuir 19(23), 9774-9780.

Wang, X., Song, J., Liu, J., Wang, Z.L., 2007b. Direct-current nanogenerators driven by ultrasonic waves. Science 316, 102-105.

Wang, X., Song, J., Summers, C.J., Ryou, J.H., Li, P., Dupuis, R.D., Wang, Z.L., 2006b. Density-controlled growth of aligned ZnO nanowires sharing a common contact: A simple, low-cost, and mask-free technique for large-scale applications. J. Phys. Chem. B 110(15), 7720-7724.

Wang, Z., Li, H.L., 2002. Highly ordered zinc oxide nanotubules synthesized within the anodic aluminium oxide template. Appl. Phys. A 74, 201-203.

Wang, Z., Qian, X., Yin, J., Zhu, Z., 2004. Large-scale fabrication of tower-like, flower-like, and tube-like ZnO arrays by a simple chemical solution route. Langmuir 20(8), 3441-3448.

Wang, Z.L., 2004a. Zinc oxide nanostructures: growth, properties and applications. J. Phys.: Condens. Matter 16, R829-R858.

Wang, Z.L., 2004b. Nanostructures of zinc oxide. Materialstoday 7(6), 26-33.

Wang, Z.L., 2007. Oxide nanobelts and nanowires-growth, properties and applications. J. Nanosci. Nanotechnol. 8, 27-55.

Wang, Z.L., 2008. Towards self-powered nanosystems: from nanogenerators to nanopiezotronics. Adv. Funct. Mater. 18, 3553-3567.

Wang, Z.L., 2009. Ten years' venturing in ZnO nanostructures: from discovery to scientific understanding and to technology applications. Chinese Science Bulletin 54(22), 4021-4034.

Wang, Z.L., Song, J.H., 2006. Piezoelectric nanogenerators based on zinc oxide nanowire arrays. Science 312, 242-246.

Wasserman, S.R., Tao, Y.T., Whitesides, G.M., 1989. Structure and reactivity of alkylsiloxane monolayers formed by reaction of alkyltrichlorosilanes on silicon substrates. Langmuir 5(4), 1074-1087.

Wei, A., Pan, L., Huang, W., 2011. Recent progress in the ZnO nanostructure-based sensors. Mater. Sci. Eng. B 176, 1409-1421.

Weintraub, B., Zhou, Z., Li, Y., Deng, Y., 2010. Solution synthesis of one-dimensional ZnO nanomaterials and their applications. Nanoscale 2(9), 1573-1587.

Wen, B., Huang, Y., Boland, J.J., 2008. Controllable growth of ZnO nanostructures by a simple solvothermal process. J. Phys. Chem. C 112(1), 106-111.

Wen, X., Fang, Y., Pang, Q., Yang, C., Wang, J., Ge, W., Wong, K.S., Yang, S., 2005. ZnO nanobelts arrays grown directly from and on zinc substrates: synthesis, characterization, and applications. J. Phys. Chem. B 109, 15303-15308.

Willander, M., Nur, O., Zhao, Q.X., Yang, L.L., Lorenz, M., Cao, B.Q., Pérez, J.Z., Czekalla, C., Zimmermann, G., Grundmann, M., Baklin, A., Behrends, A., Al-Suleiman, M., El-Shaer, A., Che Mofor, A., Postels, B., Waag, A., Boukos, N., Travlos, A., Kwack, H.S., Guinard, J., Le Si Dang, D., 2009. Zinc oxide nanorod based photonic devices: recent progress in growth, light emitting diodes and lasers. Nanotechnology 20(33), 332001-332040.

Wolf, S.F., Haines, L., Fisch, J., Kremsky, j.N., Dougherty, J.P., Jacobs, K., 1987. Rapid hybridization kinetics of DNA attached to submkron latex patricles. Nucl. Acids Res. 15(7), 2911-2926.

Wong, L.S., Khan, F., Mickfield, J., 2009. Selective covalent protein immobilization: strategies and applications. Chem. Rev. 109(9), 4025-4053.

Wu, J.J., Liu, S.C., 2002. Catalyst-free growth and characterization of ZnO nanorods. J. Phys. Chem. B 106(37), 9546-9551.

Xiao, M., Kuwabara, M., 2005. Effect of seed layer on the orientation of zinc oxide film on silicon substrate. J. Mater. Sci. Technol. 21(6), 887-890.

Xing, X., Zheng, K., Xu, H., Fang, F., Shen, H., Zhang, J., Zhu, J., Ye, C., Cao, G., Sun, D., Chen, G., 2006. Synthesis and electrical properties of ZnO nanowires. Micron. 37(4), 370-373.

Xu, C.K., Shin, P., Cao, L.L., Gao, D., 2010. Preferential growth of long ZnO nanowire array and its application in dye-sensitized solar cells. J. Phys. Chem. C 114(1), 125-129.

Xu, H.Y., Wang, H., Zhang, Y.C., Wang, S., Zhu, M., Yan, H., 2003. Asymmetric twinning crystals of zinc oxide formed in a hydrothermal process. Cryst. Res. Technol. 38(6), 429-432.

Xu, J., Han, J., Zhang, Y., Sun, Y., Xie, B., 2008a. Studies on alcohol sensing mechanism of ZnO based gas sensors. Sensors and Actuators B: Chem. 132(1), 334-339.

Xu, S., Lao, B., Weintraub, B., Wang, Z.L., 2008b. Density-controlled growth of aligned ZnO nanowire arrays by seedless chemical approach on smooth surfaces. J. Mater. Res. 23(8), 2072-2077.

Xu, S., Qin, Y., Xu, C., Wei, Y., Yang, R., Wang, Z.L., 2010. Self-powered nanowire devices. Nat. Nanotechnol. 5(5), 366-373.

Yam, C.M., Deluge, M., Tang, D., Kumar, A., Cai, C.J., 2006. Preparation, characterization, resistance to protein adsorption, and specific avidin-biotin binding of poly(aminoamine) dendrimers functionalized with oligo(ethylene glycol) on gold. Colloid Interface Sci. 296, 118-130.

Yamada, R., Sakai, H., Uosaki, K., 1999. Solvent effect on the structure of the self-assembled monolayer of alkanethiol. Chem. Lett. 28(7), 667-668.

Yamada, R., Wano, H., Uosaki, K., 2000. Effect of temperature on structure of the self-assembled monolayer of decanethiol on Au(111) surface. Langmuir 16(13), 5523-5525.

Yang, P., Yan, H., Mao, S., Russo, R., Johnson, J., Saykally, R., Morris, N., Pham, J., He, R., Choi, H., 2002. Controlled growth of ZnO nanowires and their optical properties. Adv. Funct. Mater. 12(5), 323-331.

Yang, Y., Sun, X.W., Tay, B.K., You, G.F., Tan, S.T., Teo, K.L., 2008. A p-n homojunction ZnO nanorod light-emitting diode formed by As ion implantation. Appl. Phys. Lett. 93, 253107-253109.

Yang, Z., Gonzalez-Cortes, A., Jourquin, G., Viré, J., Kauffmann, J., Delplancke, J., 1995. Analytical application of self assembled monolayers on gold electrodes: critical importance of surface pretreatment. Biosens. Bioelectron. 10(9-10), 789-795.

Yao, B.D., Chen, Y.F., Wang, N., 2002. Formation of ZnO nanostructures by a simple way of thermal evaporation. Appl. Phys. Lett. 81(4), 757-759.

Yasuda, T., Segawa, Y., 2004. Zinc oxide films synthesized by metal organic chemical reactions. Phys. Status Solidi b 241(3), 676-679.

Yoon, I.T., Ji, T.S., Park, H.L., 1997. Observation of Burstein-Moss shift in heavily Te-doped $In_{0.5}$ $Ga_{0.5}$ P layers grown by liquid phase epitaxy. Thin Solid Films 302(1-2), 270-274.

Yousefi, R., Zak, A.K., 2011. Growth and characterization of ZnO nanowires grown on the Si(111) and Si(100) substrate: Optical properties and biaxial stress of nanowires. Mat. Sci. Semicon. Proc. 14(2), 170-174.

Yue, H., Waldeck, D.H., Schrock, K., Kirby, D., Knorr, K., Switzer, S., Rosmus, J., Clark, R.A., 2008. Multiple sites for electron tunnelling between cytochrome c and mixed self-assembled monolayers. J. Phys. Chem. C. 112(7), 2514-2521.

Zhang, B., Zhou, S., Liu, B., Gong, H., Zhang, X., 2009a. Fabrication and green emission of ZnO nanowire arrays. Science in China Series E: Technol. Sci. 52(4), 883-887.

Zhang, X., Wang, H., Bourgeois, L., Pan, R., Zhao, D., Webley, P.A., 2008. Direct electrodepostion of gold nanotube arrays for sensing applications. J. Mater. Chem. 18, 463-467.

Zhang, Y., Liu, Y., Wu, L., Li, H., Han, L., Wang, B., Xie, E., 2009b. Effect of annealing atmosphere on the photoluminescence of ZnO nanospheres. Appl. Surf. Sci. 255(9), 4801-4805.

Zhang, Y., Ram, M.K., Stefanakos, E.K., Goswami, D.Y., 2012. Synthesis, characterization, and applications of ZnO nanowires. Journal of Nanomaterials 2012, 1-22.

Zhang, Y., Yu, K., Jiang, D., Zhu, Z., Geng, H., Luo, L., 2005. Zinc oxide nanorod and nanowire for humidity sensor. Appl. Surf. Sci. 242(1-2), 212-217.

Zhao, C., Huang, C., Zhu, R., Xu, J., Chen, L., Yu, D., 2011. 2D planar field emission devices based on individual ZnO nanowires. Solid State Commun. 151(22), 1650-1653.

Zhao, Q.X., Klason, P., Willander, M., 2007. Growth of ZnO nanostructures by vapour-liquid-solid method. Appl. Phys A 88(1), 27-30.

Zhou, J., Gu, Y., Fei, P., Mai, W., Gao, Y., Yang, R., Bao, G., Wang, Z.L., 2008. Flexible piezotronic strain sensor. Nano Lett. 8, 3035-3040.

CHAPTER 3

Tailoring hydrothermally grown ZnO nanowires by controlling their growth parameters

Tailoring hydrothermally grown ZnO nanowires by controlling their growth parameters

[1] D.P. Neveling, [2] T.S. van den Heever, [3] R. Bucher, [2] W.J. Perold, [1] L.M.T. Dicks

[1] Department of Microbiology, University of Stellenbosch, Private Bag X1, Matieland 7602, Stellenbosch, South Africa

[2] Department of Electrical and Electronic Engineering, University of Stellenbosch, Private Bag X1, Matieland 7602, Stellenbosch, South Africa

[3] iThemba LABS, PO Box 722, Somerset West 7129, South Africa

Abstract

Controlling the synthesis of ZnO nanowires is crucial when designing nano-generators and piezoelectric sensors. In this study, seed layer deposition, RF cylindrical magnetron sputtering and sol-gel spin coating were compared in the synthesis of ZnO nanowires by using the hydrothermal growth approach. The effects of Au film layer thickness and its crystal orientation on the growth of ZnO nanowires were also assessed. Deposited ZnO seed layer films were characterized by atomic force microscopy (AFM) and ellipsometry. Synthesized ZnO nanowires were characterized by scanning electron microscopy (SEM), energy dispersive spectroscopy (EDS), transmission electron microscopy (TEM) and X-ray diffraction (XRD). Deposition of ZnO seed layer films by the RF cylindrical magnetron sputtering technique resulted in the most c-axis oriented ZnO nanowires with uniform dimensions. An increase in the Au film layer thickness led to a decrease in diameter of the nanowires and less orientation in the c-axis. Polycrystalline Au film layer increased the mean diameter of the ZnO nanowires without effecting the c-axis orientation. These findings give insight into the conditions which are required to control the dimensions and alignment of ZnO nanowires.

Introduction

ZnO nanowires perpendicular to the substrate surface have the potential to generate piezoelectric energy which is used in electromechanical devices (Li et al., 2004). To use ZnO nanowires as nanosensors, the ZnO crystals have to be aligned perpendicular to the sample surface, e.g. along the c-axis of the substrate. By growing highly oriented ZnO nanowires, the surface per unit area of the nanosensor increases and improves the performance of the nanodevice (Song and Lim, 2007). It is thus important to control the growth, orientation, position and size of the ZnO nanowires to increase the output voltage of the nanosensor (Liu et al., 2008).

ZnO nanowires grown on silicon substrates are receiving increased interest due to the low production cost, large scale potential and different applications in electronic equipment. Numerous methods have been developed for the synthesis of ZnO nanostructures, e.g. vapour-liquid-solid (VLS) growth with the use of a catalyst (Huang et al. 2001), pulsed laser deposition (Choi et al., 2001), electrochemical deposition in porous membranes (Liu et al., 2003), metal vapour transport using Zn sources (Lyu et al., 2002), physical vapour transport using ZnO and graphite powders (Yao et al., 2002), chemical vapour deposition using zinc acetylacetonate hydrate (Wu and Liu, 2002), metal organic chemical vapour deposition using diethylzinc and O_2/N_2O as precursors (Kim et al., 2003) and the hydrothermal growth approach (Vayssiers et al., 2001). Of all these techniques, the hydrothermal growth method is preferred as it is performed at low growth temperatures and has the greatest potential in large scale production (Yousefi and Zak, 2011).

Parameters that need to be controlled to obtain ZnO nanowires with reproducible mean diameters and orientations when using the hydrothermal growth method includes the presence of a ZnO seed layer film, concentration of the reactants, pH of the solution, growth temperature, growth time and the type of substrate onto which the nanowires are synthesized (Bai and Wu, 2011; Ghosh et al., 2007; Song and Lim, 2007; Xiao and Kuwabara, 2005) It is important to control all parameters as they alter the morphology, crystallinity and alignment of the synthesized ZnO nanowires.

Growth directly onto bare silicon substrate is difficult due to the presence of lattice and thermal mismatches between the ZnO crystal nuclei and the silicon substrate (Zhang, 2010). The presence of a ZnO seed layer film strongly influences the morphology and orientation of the synthesized ZnO nanowires (Erdélyi et al., 2011). The ZnO seed layer lowers the

interfacial energy between the crystal nuclei and the substrate, hence decreasing the nucleation barrier and facilitating the growth of ZnO nanowires (Bai, 2012). Superior alignment of ZnO nanowires on ZnO seed layers are due to matching lattice structures and the polar nature of the ZnO surface. The ZnO surface is either positively or negatively charged and attracts ions of opposite charges (OH^- or Zn^+) to form ZnO (Wang, 2004). Moreover, the seed layer increases the surface roughness of the substrate surface, which results in more available nucleation sites for the growth of ZnO nanowires (Li et al., 2005; Wen et al., 2008). A decrease in the ZnO seed layer thickness results in the decrease in the mean ZnO nanowire diameter. This is due to the smaller grain sizes of the seed layer which in turn leads to an increase in the total surface area of the ZnO nanowires (Song and Lim, 2007; Wang et al., 2008).

Several methods have been developed to deposit ZnO seed layer films, e.g. chemical vapour deposition (Hu and Gordon, 1992), reactive evaporation (Swamy and Reddy, 1990), pulsed laser ablation (Ardakani, 1996), sputtering (Yoon et al., 1997), spray pyrolysis (Olvera et al., 1993), a hydrothermal method (Nishizawa and Yuasa, 1998) and the sol-gel spin coating technique (Ohyama et al., 1997; Xiao and Kuwabara, 2005). When a seed layer deposition technique is used, a number of factors need to be controlled, as they influence the c-axis orientation of the synthesized ZnO nanowires. The principle behind the sol-gel spin coating technique entails that a liquid precursor is dropped onto a surface which is spun to form a uniform monolayer. With the sol-gel spin coating technique, the concentration of the ZnO seed layer, baking temperature and time, and the final sintering temperature and time need to be carefully controlled (Bai and Wu, 2011; Li et al., 2004; Xiao and Kuwabara, 2005; Zhang et al., 2006). For the RF magnetron sputtering technique the most important factors include the sputtering time and power, as these factors influences the diameter of the ZnO grains, and subsequently, the diameter of the synthesized ZnO nanowires. The principle behind the RF magnetron sputtering technique entails radio frequencies creating plasma, which is deposited onto a surface to from a uniform monolayer. The ZnO grain diameters decrease with an increase in sputtering power, which in turn leads to a decrease in the mean diameter of the synthesized ZnO nanowires (Hwang et al., 2008; Yang et al., 2011).

The morphology of the ZnO nanowires is also affected by the purity of the growth solution and the cleanliness of the substrate surface. Any impurities in the solution or on the substrate surface result in grain sizes larger than that of the ZnO seed layer nuclei. These sites are more favourable for nucleation, which ultimately results in the formation of bush-like

nanowire bundles (Wang et al., 2012). The influence of gold on the growth of ZnO nanowires when using the hydrothermal growth approach has not yet been elucidated. However, for the VLS method gold plays a catalytic role. The thickness of the catalyst affects the diameter and the density of the ZnO nanowires (Brewster et al., 2011). A thinner catalytic layer results in smaller diameters and more dense ZnO nanowires compared to thicker catalytic layers (Dalal et al., 2006).

An increase in zinc precursor concentration increases the length and mean diameter of the synthesized ZnO nanowires (Song and Lim, 2007; Tak and Yong, 2005; Wen et al., 2008). The diameter of the ZnO nanowires also decreases with a decrease in the pH of the growth solution (Li et al., 2005; Tak and Yong, 2005), thus by controlling the concentration and pH of the aqueous solution, the growth of ZnO nanowires can be tailored to desired dimensions (Song and Lim, 2007). Hexamethylenetetramine (HMTA) also plays a role in the growth of ZnO nanowires in that it decomposes to formaldehyde and ammonia, which acts as a pH buffer and supply of OH^- precursor (Wang et al., 2008). HMTA also assists in the epitaxial growth of the ZnO nanowires. The precursor is a nonpolar chelating agent that preferentially attaches to the nonpolar facets of ZnO nanostructures, thereby exposing the (0001) plane for epitaxial growth (Sugunan et al., 2006; Wen et al., 2008).

Synthesis of ZnO nanowires by the hydrothermal growth approach involves the controlled precipitation onto a substrate through the hydrolysis/condensation reaction of metal ions and their complexes. In an ammonium-rich environment, most of the zinc ions form amine complexes. When the temperature of the solution is increased, the amine complexes reacts with the reaction media and produce ZnO crystals, and heterogeneous nucleation will take place preferentially on the ZnO seed layer surface (Wen et al., 2008). The growth temperature of ZnO nanowires affects the nucleation rate and thus the nanowire growth rate. ZnO nanowires do not form at low temperatures ($\geq$ 48 °C), while too high temperatures ($\leq$ 95 °C) results in slower nanowire growth and the presence of impurities (Wang et al., 2012). When growth temperature decreases from 90 to 60 °C, the average diameter of the synthesized ZnO nanowires decrease (Song and Lim, 2007).

The hydrothermal growth approach uses a closed system with limited amounts of precursors. Therefore the depletion of the precursors is inevitable and the growth rate will decrease as the reaction time increases (Tak and Young, 2005). The length of the ZnO nanowires can be experimentally tailored until precursors become depleted by adjusting the

growth time. However, as the nanowires grow longer they become intertwined (Li et al., 2005).

The substrate onto which the ZnO nanowires are grown should also be considered as lattice mismatches between the substrate and the ZnO nanowires affect the morphology and alignment of the synthesized ZnO nanowires (Yousefi and Zak, 2011). Surface atoms in a Si (100) substrate are arranged in a square pattern, whilst they follow a hexagonal pattern for a Si (111) substrate as does the ZnO crystal structure. The Si (111) surface has a better matching lattice with the ZnO lattice, compared to that of Si (100) (Yousefi and Zak, 2011). ZnO nanowires grown on Si (111) substrates have larger diameters than those grown on Si (100) and are more crystalline as opposed to amorphous (Sugunan et al., 2006; Wen et al., 2008).

Control of the morphology and alignment of ZnO nanowires involves controlling numerous factors and their combined activities result in well-aligned ZnO nanowire arrays. In this study we report the synthesis of ZnO nanowires by the hydrothermal growth approach on Si (100) substrates coated with an Au film layer and a ZnO seed layer film. A comparative study was used to determine the most suitable seed layer deposition technique for the synthesis of ZnO nanowires. Sol-gel spin coating and the RF cylindrical magnetron sputtering techniques were compared. The effect of Au film layer thickness and crystal orientation on the morphology and alignment of the synthesized ZnO nanowires were also assessed. The ZnO seed layers were characterized by atomic force microscopy (AFM) and ellipsometry. ZnO nanowires were characterized by scanning electron microscopy (SEM), energy-dispersive x-ray spectroscopy (EDS), transmission electron microscopy (TEM) and X-ray diffraction (XRD).

Materials and Methods

Preparation of silicon wafers

Silicon (100) wafers were cut into 1 x 1 cm sizes and sonicated for 10 min in acetone, followed by 10 min in absolute ethanol and 10 min in distilled H_2O. The wafers were dried under nitrogen gas and placed on a hot plate at 110 °C for 5 min and then immersed in 40 % (v/v) hydrofluoric acid for 30 sec to enhance bonding between the Si and Au atoms. The wafers were then rinsed in distilled H_2O, dried under nitrogen gas and heated on a hot plate as

before, and placed in an Edwards S150B sputter coater (Edwards, West Sussex, UK). A 40 nm Au film layer was sputtered onto the silicon wafers at 1.5 kV and 20 mA, under vacuum (2 x 10^{-1} mbar) in the presence of argon.

Deposition of the ZnO seed layers

The gold-plated Si wafers were cleaned by rapid immersion in absolute ethanol to remove surface impurities, dried under nitrogen gas and placed on a hot plate at 110 °C for 5 min. ZnO seed layers were deposited by the sol-gel spin coating or the RF cylindrical magnetron sputtering techniques. The sol-gel spin coating technique was performed as follows: zinc acetate dehydrate was dissolved in a mixture of 2-methoxyethanol and monoethanolamine at 25 °C. The concentration of zinc acetate was 0.75 M and the molar ratio of monoethanolamine to zinc acetate was 1:1. The solution was stirred for 1 h at 60 °C and 25 µl was placed onto the gold-plated Si wafers and spun in a Laurell WS-400-6NPP spin coater (Laurell Technologies, Pennsylvania, USA) at 3000 rpm for 30 sec. After spin-coating, the wafers were baked at 200 °C for 5 min on a hot plate to evaporate the solvent and remove the residual organic components. The procedure was repeated up to six times. The ZnO seed layers were then annealed in air at 700 °C for 10 min.

With the RF cylindrical magnetron sputtering technique, ZnO was deposited under 2 x 10^{-2} mbar pressure in the presence of 60 % oxygen and at 100 W. The deposition time varied from 1 to 6 min.

Effect of Au thickness on the growth of ZnO nanowires

To determine the effect Au film layer thickness has on the growth of ZnO nanowires synthesized using the hydrothermal growth approach, Au film layers of different thicknesses were used. Silicon wafers were prepared as before. However, after etching with hydrofluoric acid, the wafers were sputtered with Au using an Edwards S150B sputter coater, as described before, to yield layers of 20, 40 and 60 nm in thickness. The ZnO seed layers were deposited for 3 min using the RF cylindrical magnetron sputtering technique under 2 x 10^{-2} mbar pressure in the presence of 60 % oxygen and at 100 W.

Effect of Au crystal orientation on the growth of ZnO nanowires

To determine the effect of Au crystal orientation on the growth of the ZnO nanowires, single and polycrystalline Au film layer were used. Silicon wafers were prepared as described before, and sputtered with a single crystalline Au film layer (40 nm) by an Edwards S150B sputter coater as described above or a 40 nm polycrystalline Au film layer by the hydrothermal evaporation method. In the latter, the chamber was evacuated to 2 x 10^{-5} mbar and the thickness of the Au film layer was controlled using a QCM sensor (Sigma Instruments, Colorado, USA). ZnO seed layers were deposited for 3 min using the RF cylindrical magnetron sputtering technique under 2 x 10^{-2} mbar pressure in the presence of 60 % oxygen and at 100 W.

Synthesis of ZnO nanowires

ZnO nanowires were synthesized using the hydrothermal growth method. The gold-plated Si wafers coated with a ZnO seed layer were placed in a solution of 0.01 M zinc nitrate hexahydrate [$Zn(NO_3)_2 \cdot 6H_2O$] and 0.01 M hexamethylenetetramine [$C_6H_{12}N_4$] in distilled H_2O for 7 h in an oven at 90 °C. The wafers were then washed with distilled water to remove residual salts and amino complexes, dried under nitrogen gas and placed on a hotplate at 110 °C for 5 min. The wafers were then baked at 350 °C for 30 min.

Characterization of ZnO nanowires

A Nanosurf AFM Easyscan 2 (Nanosurf Inc., California, USA) was used to characterize the surface topology and to determine the surface roughness of the ZnO seed layers deposited by the sol-gel spin coating and RF cylindrical magnetron sputtering techniques. A Woollam J.A. M-2000 variable angle spectroscopic ellipsometer with a rotating analyser, VASE (J.A. Woollam Co. In., Nebraska, USA), was used to determine the surface thickness of the deposited ZnO seed layer films. The ellipsometric angles Ψ and Δ were obtained for variable incidence angles by measuring the complex Fresnel reflection coefficients r_p and r_s as indicated in equation 1(Madsen et al., 2011).

$$\frac{r_p}{r_s} = \tan(\psi) \cdot e^{i\Delta} \quad (1)$$

Measurements were obtained in the range of 10-500 nm at room temperature for an angle of incidence of 65°. The films were regarded as homogeneous material with film thickness modelled using a Cauchy model. The experimental data was fitted to obtain the optical functions of the blends using a Lorentz model. Model parameters were obtained by minimizing the error function which is defined by the following equation (Jellison, 1993).

$$MSE = \frac{\sum\left[\frac{\left|\tan(\psi_{\exp}) - \tan(\psi_{cal})\right|}{\sigma_{\tan}(\psi)}\right]^2 + \left[\frac{\left|\cos(\Delta_{\exp}) - \cos(\Delta_{cal})\right|}{\sigma_{\cos}(\Delta)}\right]^2}{N - M - 1} \quad (2)$$

Where MSE is the mean square error, Ψ_{exp}, Δ_{exp} are the measured values and Ψ_{cal}, Δ_{cal} are the calculated values, N is the number of wavelengths at which measurements were performed, and M is the number of parameters used in the fit.

The surface morphology, diameter and density of the synthesized ZnO nanowires were evaluated using a FEI Nova NanoSEM 230, equipped with a TLD detector (FEI, Oregon, USA). The purity and elemental composition of the ZnO nanowires were analysed by energy-dispersive x-ray spectroscopy (EDS) using a FEI Nova NanoSEM 230, equipped with an X/Max Oxford energy-dispersive x-ray (EDX) detector (Oxford Instruments, Oxfordshire, UK) with a detector area of 20 mm^2. EDS spectrums were analysed using INCA software (Inca Software, Berkshire, UK).

TEM micrographs were collected with a FEI Tecnai G^2 F20 TEM (FEI, Oregon, USA), of which the LaB_6 filament was operated at an accelerating voltage of 200 kV. Selected area electron diffraction (SAED) patterns were collected on a Philips Tecnai TF20 TEM (FEI, Oregon, USA), equipped with a field emission gun and operated at an accelerating voltage of 200 kV. High resolution transmission electron microscopy (HRTEM) images were obtained to analyse the crystal structure of the ZnO nanowires and indicate whether the axial growth is along the [0001] direction. The mean length and wall diameter of the ZnO nanowires were also determined using TEM micrographs. For this purpose ZnO nanowires were scratched off the substrate surface, dissolved in absolute ethanol and ultrasonicated for 10 sec. A drop of the liquid was placed on a Cu grid of which the back was covered with a carbon film layer. The samples were allowed to air dry prior to analysis.

The ZnO nanowires and Au film layers crystal structures and phase compositions were determined by XRD using a Bruker AXS D8 Advance X-ray diffractometer operated in locked coupled mode (Bruker AXS, Frankfurt, Germany). The instrument was equipped with a Vantec-1 position sensitive detector optimized for Cu-Kα radiation with λ= 1.5406 Å. The X-ray tube was operated at 40 mA and 40 kV and the measurements were recorded at a scanning rate of 0.5 sec/step with a step size of 0.014° in a for 2θ range extending from 31.28° to 149.3°.

Results and Discussion

Seed layer deposition

Surface topology images of the ZnO seed layers deposited by the sol-gel spin coating and RF cylindrical magnetron sputtering techniques are shown in Fig. 1. ZnO seed layer films deposited by the RF cylindrical magnetron sputtering technique for 1 to 6 min [Fig. 1 (a-f)] resulted in mean ZnO seed grain diameters of 25, 33, 49, 54, 62 and 72 nm, respectively, and a corresponding root-mean-square surface roughness of 14, 13, 13, 12, 11 and 9 nm. The ZnO seed layer films deposited by the sol-gel spin coating technique for 1 to 6 coats [Fig. 1 (g-l)] resulted in mean ZnO seed grain diameters of 34, 58, 87, 96, 112 and 133 nm, respectively, and a corresponding root-mean-square roughness of 24, 38, 54, 68, 84 and 98 nm. In both seed layer deposition techniques an increase in ZnO deposition resulted in an increase in the ZnO seed grain diameter, which is consistent with previous reported results (Zhang et al., 2006). An increase in ZnO deposition using the sol-gel spin coating technique resulted in an increase in surface roughness. However, in the case of the RF cylindrical magnetron sputtering technique a decrease in surface roughness was observed. The thickness of the ZnO seed layers deposited by the RF cylindrical magnetron sputtering technique for 1 to 6 min was 14, 25, 39, 59, 78 and 92 nm, respectively. The sol gel spin technique with 1 to 6 coats produced ZnO layers with a thickness of 49, 98, 147, 194, 248 and 301 nm, respectively.

High magnification top SEM images of ZnO nanowires synthesized on ZnO seed layers deposited by both deposition techniques revealed the effect an increase in the ZnO seed layer thickness had on the mean diameter of the synthesized nanowires [Fig. 2 and 3 (a-f)]. An increase in the ZnO seed layer thickness resulted in an increase in the mean diameter of the synthesized ZnO nanowires. Low magnification 45° tilted SEM images [Fig. 2 and 3 (g-l)]

indicated that the ZnO nanowires were uniformly spread and mainly c-axis oriented. These results correspond with that previously reported by Xiao and Kuwabara (2005). All ZnO seed layers deposited by both deposition techniques resulted in hexagonal shaped ZnO nanowires [Figs. 2 and 3 (a-f)].

The mean diameter of the synthesized ZnO nanowires was calculated by determining the relative diameter abundance of 500 ZnO nanowires. The mean diameter of ZnO nanowires synthesized on a seed layer deposited by the RF cylindrical magnetron sputtering technique for 1 to 6 min was 26 nm (σ= 2.53), 36 nm (σ= 2.44), 35 nm (σ= 3.42), 45 nm (σ= 2.62), 46 nm (σ= 2.07) and 83 nm(σ= 4.05), respectively. An F-test was conducted to determine whether the means of the samples were normally distributed. The Kruskal-Wallis test was done to determine whether the samples originated from the same distribution. ANOVA statistical test was conducted to test whether the means of the samples of the different groups were equal. Statistical analysis indicated that the ZnO nanowire diameters followed a normal distribution which differed significantly in their average and standard deviation for deposition times between 1 and 6 min. However, deposition between 2 and 3 min, and 4 and 5 min were statistical similar ZnO nanowire diameters. The nanowire densities of the respective sputtering times were 48, 75, 120, 91, 49 and 43 per μm^2. The density of the nanowires increased up to 3 min of deposition, followed by a steady decrease. The initial increase is as a result of disoriented ZnO nanowires becoming more oriented. The decrease is due to an increase in the mean ZnO nanowire diameter. These results correspond with previously reported results, i.e. increasing the sputtering time results in an increase in the mean ZnO seed grain diameter, and subsequently an increase in the average diameter of the synthesized ZnO nanowires (Song and Lim, 2007).

A mean diameter of 40 nm (σ= 8.14), 65.6 nm (σ= 8.74), 64 nm (σ= 4.46), 63 nm (σ= 4.75), 84 nm (σ= 4.44) and 79 nm (σ= 8.7) was recorded for ZnO nanowires synthesized on seed layers deposited by the sol-gel spin coating technique for 1-6 spin coats, respectively. Statistical analysis concluded that the ZnO nanowire diameters followed a normal distribution which differed significantly in their average and standard deviation for 1-6 spin coats, however were statistically similar for 2-4 spin coats, and 5-6 spin coats. These results correspond with previously reported results (Kenanakis et al. ; Wang et al., 2008). The ZnO nanowire densities recorded with sol-gel spin coating were 123, 75, 68, 57, 49 and 44 per μm^2 for 1 to 6 spin coats, respectively. The nanowire density decreased continuously as the mean ZnO nanowire diameter increased. RF cylindrical magnetron sputtering resulted in

a higher abundance of the mean ZnO nanowire diameter as appose to sol-gel spin coating technique which resulted in a more diverse ZnO nanowire diameter range. Energy dispersive spectroscopy analysis of the individual ZnO nanowires synthesized on both types of ZnO seed layers indicated that Zn (47-49 %) and O (53-51 %) elements were nearly stoichiometric with a ratio of 1:1.

Transmission electron microscopy images of ZnO nanowires synthesized on seed layers deposited by the RF cylindrical magnetron sputtering [Fig. 4 (a-f)] and the sol-gel spin coating technique [Fig. 4 (g-l)], with corresponding HRTEM images and SAED patterns, where used to study the crystallinity and crystal growth planes of the synthesized ZnO nanowires. Transmission electron microscopy and SEM observations indicated that an increase in the ZnO seed layer thickness by either deposition technique resulted in an increase in the mean diameter of the synthesized ZnO nanowires. The corresponding HRTEM images of the synthesized ZnO nanowires by both deposition techniques revealed a major lattice spacing of 0.28 nm, which corresponds to the distance of the (002) crystal plane of wurtzite ZnO. Additional lattice spacings for seed layers deposited by the RF cylindrical magnetron sputtering technique were 0.37 nm and 0.44 nm for 1 min deposition, which corresponds to the crystal planes (102) and (103) respectively; 0.26 nm for 5 min deposition, corresponding to crystal plane (100); and 0.48 nm for 6 min deposition, corresponding to crystal plane (105) of wurtzite ZnO. The HRTEM image also confirmed the perfection of the atomic arrangements within the ZnO nanowires. The corresponding SAED patterns of individual ZnO nanowires synthesized on both types of seed layer films revealed that the ZnO nanowires have a single-crystal hexagonal wurtzite structure. By indexing the diffraction patterns the main axis of the ZnO nanowires equivalent to the growth direction can be determined. All ZnO nanowires synthesized on both types of seed layer films grew along the [0001] direction. The average length of ZnO nanowires synthesized for a growth period of 7 h was estimated by using a TEM micrograph which contained ZnO nanowires attached to the substrate surface [Fig. 5 a-c]. The average length of ZnO nanowires were between 1.6 and 1.7 µm for ZnO nanowires synthesized on both types of ZnO seed layers.

The XRD patterns of ZnO nanowires produced on ZnO seed layers deposited by both deposition techniques were used to assess which seed layer film results in the most c-axis (Table 1) oriented ZnO nanowires by looking at the at the relative abundance of ZnO diffraction peaks other than the 002 peak. Since the surface of the sample lies in the scattering plane of the instrument, a set of perfectly aligned nanowires standing perpendicular

to that surface would result in a single diffraction peak, e.g. the 002 peak. Those nanowires standing oblique to the surface will, however, contribute to diffraction peaks other than the 002 peak. Hence, the relative distribution of ZnO diffraction peaks will indicate which samples present the highest orientation of nanowires along the [0001] direction. The ZnO diffraction peaks that did not overlap with either the gold layer or the Si substrate peaks are listed. The XRD patterns of all ZnO nanowires synthesized on both seed layer films were indexed using the JCPDS database and corresponded to hexagonal ZnO. The peak intensities of all XRD patterns were normalized with respect to the 002 reflection. The XRD patterns indicated that an increase in the ZnO seed layer thickness, using the RF cylindrical magnetron sputtering technique, resulted in a decrease in the intensity of crystal planes other than the (002) plane, which indicates that an increase in the ZnO seed layer thickness improved the c-axis orientation of the synthesized ZnO nanowires. The XRD patterns of ZnO nanowires synthesized on seed layers deposited by the sol-gel spin coating technique indicated that increasing the ZnO seed layer thickness resulted in an increase in the intensity of other crystal planes other than the (002) plane, which indicates a worsening of the c-axis alignment. This may be due to the increase in the surface roughness of the seed layers deposited by the sol-gel spin coating technique. As increasing the seed layer thickness by the RF cylindrical magnetron sputtering technique decreased the surface roughness and improved the c-axis orientation of the ZnO nanowires. This may be due to surface impurities, as increased deposition by the sol-gel spin coating technique results in the increase in exposure to impurities. Results previously reported show that smoother seed layer surfaces result in more aligned nanowires as opposed to rougher surfaces (Erdélyi et al., 2011). Findings by Wang et al. (2008) and Zhang (2010) indicated that an increase in the spin coating time of the sol-gel spin coating technique results in worsening of the seed layer quality, and subsequently gives rise to disoriented nanowires. However, the presence of strong 002 diffraction peaks for all ZnO nanowires synthesized on seed layers deposited by both deposition techniques confirmed that the ZnO nanowires were preferentially oriented along the [0001] direction.

Results obtained by XRD, SEM and TEM have shown that the ZnO nanowires are vertically aligned and are preferentially oriented along the [0001] direction. Increasing the ZnO seed layer thickness by both deposition techniques resulted in an increase in the mean ZnO nanowire diameter. The RF cylindrical magnetron sputtering technique resulted in a higher abundance of mean ZnO nanowires compared to the sol-gel spin coating technique which resulted in more diverse ZnO nanowire diameters. Increasing the ZnO seed layer

thickness by the RF cylindrical magnetron sputtering technique improved the c-axis alignment. However, for the sol-gel spin coating technique a worsening of the c-axis alignment was observed, which may be due to the increase in surface roughness. Previous reports showed that smoother seed layer surfaces results in more aligned nanowires, as opposed to rougher surfaces (Erdélyi et al., 2011). These results show that the morphology and alignment of the ZnO nanowires depends on the quality of the deposited seed layer, corresponding to findings reported by Ladanov et al. (2013), Li et al. (2005), and Xiao and Kuwabara (2005).

Au film layer thickness

The effect of the Au film layer thickness on the growth of the ZnO nanowires was assessed by varying the Au film layer thickness from 20-60 nm. X-ray diffraction analysis indicated that a single crystalline Au (111) film layer was deposited using the Edwards sputter coater. The hexagonal shape of the synthesized ZnO nanowires was clearly visible in high magnification top SEM images [Fig. 6 (a-c)]. The ZnO nanowires were uniformly distributed over a large surface area and were mainly c-axis oriented, as shown with the 45° tilted SEM images taken at low magnification [Fig. 6 (d-f)]. An increase in the Au (111) film layer thickness resulted in a decrease in the mean diameter of the synthesized ZnO nanowires. The mean diameter for the ZnO nanowires synthesized on a 20, 40 and 60 nm Au (111) film was 48 nm (σ= 19), 32 nm (σ= 3.35) and 27 nm (σ= 1.93), respectively. Statistical analysis concluded that the ZnO nanowire diameters followed a normal distribution and that the average diameter and standard deviation differed significantly for ZnO nanowires synthesized on different Au (111) film layer thicknesses. The nanowire densities were 68, 112 and 184 per μm^2, respectively. An increase in the Au (111) film layer thickness resulted in an increase in the nanowire density, which is due to the decrease in the mean ZnO nanowire diameter. Energy dispersive spectroscopy analysis of individual ZnO nanowires synthesized on varying Au film layer thicknesses showed that the elements Zn (48-50 %) and O (50-52 %) were nearly stoichiometric with a ratio of 1:1.

The ZnO crystallinity and growth direction of nanowires synthesized on an Au (111) film layer of 20, 40 and 60 nm thick were studied using TEM images [Fig. 7 (a-c)], HRTEM images and SAED patterns. Transmission electron microscopy images of the ZnO nanowires corresponded with SEM images, showing that the mean diameter of the nanowires decreased

with an increase in Au (111) film layer thickness. The HRTEM images revealed that the major lattice spacing is 0.28 nm, which corresponds to the (002) crystal planes of wurtzite ZnO. Additional lattice spacing of 0.26 nm was observed for 60 nm Au (111) film layer, which corresponds to the (100) crystal plane of wurtzite ZnO. The HRTEM images confirmed the perfection of the atomic arrangement within the ZnO nanowires.

The corresponding SAED patterns revealed that the ZnO nanowires were single crystalline and have a wurtzite structure. The indexed diffraction patterns of the ZnO nanowires indicated that the growth direction of all ZnO nanowires is along the [0001] direction. XRD patterns of the ZnO nanowires synthesized on varying Au (111) film layer thicknesses are listed in Table 2. The XRD spectra of all ZnO nanowires were indexed to hexagonal ZnO, which correlates with SEM observations. X-ray diffraction spectra were normalized with respect to the 002 reflection. An increase in the Au (111) film layer thickness resulted in an increase in the intensity of other crystal planes other than the (002) plane, indicating a worsening in the c-axis alignment of the ZnO nanowires. The presence of strong 002 diffraction peaks for all ZnO nanowires confirmed that the synthesized ZnO nanowires were preferentially oriented perpendicular to the substrate surface. Based on data obtained from SEM, TEM and XRD the ZnO nanowires were vertically aligned and preferentially oriented along the [0001] direction. Increasing the Au (111) film layer thickness resulted in a decrease in the mean ZnO nanowire diameter and worsening of the c-axis alignment.

These results show that the presence of an Au film layer beneath the ZnO seed layer affects the morphology of the synthesized ZnO nanowires. Results recently reported showed that the growth of ZnO nanowires are effected by a metal underlayer (Brown et al., 2013). Brown et al. (2013) showed that the presence of an Au film layer leads to the decrease in the average nanowire diameter, which is due to a faster initial growth rate. It is speculated that the presence of a metal film layer inhibits nanowire growth by the presence of metal cations which causes fluctuations in the local pH and/or leading to defect formation in the crystal lattice (Brown et al., 2013; Chew et al., 2012).

Au film layer crystal orientation

Gold deposited by the sputtering technique using the Edwards S150B sputter coater resulted in single crystalline Au (111) film layers, whereas Au deposited by the hydrothermal evaporation method resulted in polycrystalline Au films layers [(111) 77%, (200) 7%, (220)

8%, and (311) 8%], as determined by XRD. The hydrothermal evaporation method resulted in a polycrystalline film layer due to the aqueous based method of deposition which ultimately results in poor orientation. Top high magnification SEM images [Fig. 8 (a-b)] of Au (111) and polycrystalline Au film layers indicated that hexagonal shaped ZnO nanowires were synthesized. Low magnification, 45° tilted SEM images [Fig. 8 (c-d)], revealed uniformly distributed, mainly c-axis oriented ZnO nanowires over a large surface area. The mean diameters for ZnO nanowires synthesized on polycrystalline Au and Au (111) film layers were 57 nm (σ= 6) and 35 nm (σ= 2), respectively. Statistical analysis concluded that the ZnO nanowire diameters were normally distribution and differed significantly with respect to their average diameter and standard deviation. Polycrystalline Au resulted in an increase in the mean ZnO nanowire diameter, whereas single crystalline Au (111) resulted in a decrease in the mean diameter. The nanowire density was 120 and 79 per μm^2 for Au (111) and polycrystalline Au film layers, respectively. A single crystalline film resulted in higher densities of ZnO nanowires due to smaller diameters as compared to a polycrystalline film layer. Energy dispersive spectroscopy analysis of the individual ZnO nanowires indicated that the elements Zn (49-50 %) and O (50-51 %) were nearly stoichiometric with a ratio of 1:1.

TEM images of synthesized ZnO nanowires [Fig. 9 (a-b)] corresponded with SEM images obtained, i.e. the mean diameter of the nanowires decreased with improvement in the single crystallinity of the Au film layer. Corresponding HRTEM images of the ZnO nanowires revealed a major lattice spacing of 0.28 nm, which corresponds to the (002) crystal plane. Indexing the diffraction patterns of the corresponding SEAD patterns indicated that the growth direction of all the synthesized ZnO nanowires was along the [0001] direction. The XRD pattern of the synthesized ZnO nanowires (Table 3) indicated that the crystal orientation of the gold film layer had no effect on the c-axis alignment of the synthesized ZnO nanowires.

No major differences in the presence of planes other than the (002) plane was observed. The presence of strong 002 diffraction peaks for all ZnO nanowires confirmed that the synthesized ZnO nanowires were preferentially oriented along the [0001] direction. Based on SEM, TEM and XRD results the ZnO nanowires were vertically aligned and preferentially oriented along the [0001] direction. Polycrystalline Au film layers resulted in an increase in the mean ZnO nanowire diameter as compared to single crystalline Au (111) film layers, and the Au film layer crystal orientation had no effect on the c-axis alignment of the synthesized ZnO nanowires.

Conclusion

Numerous factors need to be taken into account when synthesizing ZnO nanowires. An increase in ZnO seed layer thickness increased the mean diameter of the synthesized ZnO nanowires. When the RF cylindrical magnetron sputtering technique was used, an increase in the ZnO seed layer thickness decreased the reflection intensity of other ZnO crystal planes, excluding the (002) plane. This suggested an improvement in the ZnO nanowire c-axis alignment. However, when the sol-gel spin coating technique was used, an increase in the ZnO seed layer thickness increased the presence of other ZnO crystal planes, excluding the (002) plane. This suggested that the c-axis alignment of the ZnO nanowires worsened. The RF cylindrical magnetron sputtering technique resulted in a higher abundance of the mean ZnO nanowire diameter compared to the sol-gel spin coating technique which results in a more diverse ZnO nanowire diameter. An increase in the Au (111) film layer thickness resulted in a decrease in the mean ZnO nanowire diameter and an increase in the presence of other ZnO crystal planes, excluding the (002) plane. This suggested that the c-axis alignment worsened with the increase in Au (111) film layer thickness. Polycrystalline Au film layers increased the mean ZnO nanowire diameter as appose to single crystalline Au (111) film layers. Gold crystal orientation had no effect on the c-axis orientation of the synthesized ZnO nanowires. The optimal ZnO nanowire structure in a transducer is one with the smallest diameter and perfectly orientated. These findings show the importance of the intial quality of the ZnO seed layer. The seed layer deposition technique, RF magnetron sputtering produces a more uniform ZnO seed layer with seed grains of similar sizes, as opposed to the sol-gel spin coating technique. Metal surfaces beneath the ZnO seed layer effects the growth of ZnO nanowires. The quality of the metal film layer, in turn, effects the quality of the deposited ZnO seed layer and, hence, the quality of the synthesized ZnO nanowires.

References

Ardakani, H.K., 1996. Electrical conductivity of in situ “hydrogen-reduced” and structural properties of zinc oxide thin films deposited in different ambients by pulsed excimer laser ablation. Thin Solid Films 287(1-2), 280-283.

Bai, S., 2012. Growth and properties of ZnO nanowires synthesized by a simple hydrothermal method. J. Mater. Sci: Mater. Electron 23(2), 398-402.

Bai, S., Wu, S., 2011. Synthesis of ZnO nanowires by the hydrothermal method, using the sol-gel prepared ZnO seed films. J. Mater. Sci: Mater. Electron 22(4), 339-344.

Brewster, M.M., Zhou, X., Lim, S.K., Gradečak, S., 2011. Role of Au in the growth and nanoscale optical properties of ZnO nanowires. J. Phys. Chem. Lett. 2(6), 586-591.

Brown, R.A., Evans, J.E., Smith, N.A., Tarat, A., Jones, D.R., Barnett, C.J., Maffeis, T.G.G., 2013. The effect of metal layers on the morphology and optical properties of hydrothermally grown zinc oxide nanowires. J. Mater. Sci. 48, 4908-4913.

Chew, C.J., Brown, R.A., Maffeis, T.G.G., Li, L., 2012. Comparison of ZnO nanowires synthesized on various surfaces on a single substrate. Mater. Lett. 72(1), 60-63.

Choi, J.H., Tabata, H., Kawai, T., 2001. Initial preferred growth in zinc oxide thin films on Si and amorphous substrates by a pulsed laser deposition. J. Cryst. Growth 226(4), 493-500.

Dalal, S.H., Baptista, D.L., Teo, K.B.K., Lacerda, R.G., Jefferson, D.A., Milne, W.I., 2006. Controllable growth of vertically aligned zinc oxide nanowires using vapour deposition. Nanotechnol. 17(19), 4811-4818.

Erdélyi, R., Nagata, T., Rogers, D.J., Teherani, F.H., Horváth, Z.E., Lábadi, Z., Baji, Z., Wakayama, Y., Volk, J., 2011. Investigations into the impact of the template layer on ZnO nanowire arrays made using low temperature wet chemical growth. Cryst. Growth Des. 11(6), 2515-2519.

Ghosh, R., Dutta, M., Basak, D., 2007. Self-seeded growth and ultraviolet photoresponse properties of ZnO nanowire arrays. Appl. Phys. Lett. 91(7), 073108.

Hu, J., Gordon, R.G., 1992. Textured aluminium-doped zinc oxide thin films from atmospheric pressure chemical-vapour deposition. J. Appl. Phys. 71(2), 880-890.

Huang, H., Mao, S., Feick, H., Yan, H., Wu, Y., Kind, H., Tran, N., Weber, E., Ruso R., Yang, P., 2001. Room-temperature ultraviolet nanowire nanolasers. Science 292(5523), 1897-1899.

Hwang, B., Park, K., Chun, H., An, C., Kim, H., Lee, H., 2008. The effects of the microstructure of ZnO films on the electrical performance of their thin film transistors. Appl. Phys. Lett. 93(22), 222104.

Jellison, G.E., 1993. Data analysis for spectroscopic ellipsometry. Thin Solid Films 234(1-2), 416-422.

Kenanakis, G., Vernardou, D., Koudoumas, E., Katsarakis, N., 2009. Growth of z-axis oriented ZnO nanowires from aqueous solution: the decisive role of a seed layer for controlling the wires diameter. J. Crys. Growth 311(23-24), 4799-4804.

Kim, S.W., Fujita, Sz., Fujita, Sg., 2003. Self-organized ZnO quantum dots on SiO_2/Si substrates by metalorganic chemical vapour deposition. Appl. Phys. Lett. 81(26), 5036-5038.

Ladanov, M., Algarin-Amaris, P., Villalba, P., Emirov, Y., Matthews, G., Thomas, S., Ram, M.K., Kumar, A., Wang, J., 2013. Effects of the physical properties of atomic layer deposition grown seeding layers on the preparation of ZnO nanowires. J. Phys. Chem. Solids, http://dx.doi.org/10.1016/j.jpcs.2013.05.026.

Li, H., Wang, J., Liu, H., Yang, C., Xu, H., Li, X., Cui, H., 2004. Sol-gel preparation of transparent zinc oxide films with highly preferential crystal orientation. Vacuum 77(1), 57-62.

Li, Q., Kumar, V., Li, Y., Zhang, H., Marks, T.J., Chang, R.P.H., 2005. Fabrication of ZnO nanorods and nanotubes in aqueous solutions. Chem. Mater. 17(5), 1001-1006.

Liu, C., Zapien, J.A., Yao, Y., Meng, X., Lee, C.S., Fan, S., Lifshitz, Y., Lee, S.T., 2003. High-density, ordered ultraviolet light-emitting ZnO nanowire arrays. Adv. Mater. 15(10), 838-841.

Liu, J., Fei, P., Zhou, J., Tummala, R., Wang, Z.L., 2008. Toward high output-power nanogenerator. Appl. Phys. Lett. 92(17), 173105.

Lyu, S.C., Zhang, Y., Ruh, H., Lee, H.J., Shim, H.W., Suh, E.K., Lee, C.J., 2002. Low temperature growth and photoluminescence of well-aligned zinc oxide nanowires. Chem. Phys. Lett. 363(1-2), 134-138.

Madsen, M.V., Sylvester-Hvid, K.O., Dastmalchi, B., Hingerl, K., Norrman, K., Tromholt, T., Manceau, M., Angmo, D., Krebs, F.C., 2011. Ellipsometry as a non-destructive depth profiling tool for roll-to-roll manufactured flexible solar cells. J. Phys. Chem. C 115(21), 10817-10822.

Nishizawa, H., Yuasa, K., 1998. Preparation of highly oriented ZnO thin film under hydrothermal conditions. J. Mater. Sci. Lett. 17(12), 985-987.

Ohyama, M., Kozuka, H., Yoko, T., 1997. Sol-gel preparation of ZnO films with extremely preferred orientation along (002) plane from zinc acetate solution. Thin Solid Films 306(1), 78-85.

Olvera, M.de la L., Maldonado, A., Asomoza, R., Konagai, M., Asomoza, M., 1993. Growth of textured ZnO-IN thin-films by chemical spray deposition. Thin Solid Films 229(2), 196-200.

Song, J., Lim, S., 2007. Effect of seed layer on the growth of ZnO nanorods. J. Phys. Chem. C 111(2), 596-600.

Sugunan, A., Warad, H.C., Boman, M., Dutta, J., 2006. Zinc oxide nanowires in chemical bath on seeded substrates: Role of hexamine. J. Sol-Gel Sci. Techn. 39(1), 49-56.

Swamy, H.G., Reddy, P.G., 1990. Preparation of ZnO films by activated reactive evaporation. Semicond. Sci. Technol. 5, 980-981.

Tak, Y., Yong, K., 2005. Controlled growth of well-aligned ZnO nanorod array using a novel solution method. J. Phys. Chem. B 109(41), 19263-19269.

Vayssiers, L., Keis, K., Lindquist, S., Hagfeldt, A., 2001. Purpose-built anisotropic metal oxide material: 3D highly oriented microrod array of ZnO. J. Phys. Chem. B 105(17), 3350-3352.

Wang, L., Tsan, D., Stoeber, B., Walus, K., 2012. Substrate-free fabrication of self-supporting ZnO nanowire arrays. Adv. Mater. 24(29), 3999-4004.

Wang, M., Ye, C., Zhang, Y., Wang, H., Zheng, X., Zhang, L., 2008. Seed-layer controlled synthesis of well-aligned ZnO nanowire arrays via a low temperature aqueous solution method. J. Mater. Sci: Mater. Electron 19(3), 211-216.

Wang, Z.L., 2004. Nanostructures of ZnO. Mater. Today 7(6), 26-33.

Wen, B., Huang, Y., Boland, J.J., 2008. Controllable growth of ZnO nanostructures by a simple solvothermal process. J. Phys. Chem. C 112(1), 106-111.

Wu, J., Liu, S., 2002. Catalyst-free growth and characterization of ZnO nanorods. J. Phys. Chem. B 106(37), 9546-9551.

Xiao, M., Kuwabara, M., 2005. Effect of seed layer on the orientation of zinc oxide film on silicon substrate. J. Mater. Sci. Technol. 21(6), 887-890.

Yang, J., Lee, M.S., Park, K., Moon, M.R., Jung, D., Kim, H., Lee, H., 2011. Effects of the microstructure of ZnO seed layer on the ZnO nanowire density. J. Mater. Res. 26(10), 1292-1297.

Yao, B.D., Chen, Y.F., Wang, N., 2002. Formation of ZnO nanostructures by a simple way of thermal evaporation. Appl. Phys. Lett. 81(4), 757-759.

Yoon, I.T., Ji, T.S., Park, H.L., 1997. Observation of Burstein-Moss shift in heavily Te-doped $In_{0.5}$ $Ga_{0.5}$ P layers grown by liquid phase epitaxy. Thin Solid Films 302(1-2), 270-274.

Yousefi, R., Zak, A.K., 2011. Growth and characterization of ZnO nanowires grown on the Si(111) and Si(100) substrate: Optical properties and biaxial stress of nanowires. Mat. Sci. Semicon. Proc. 14(2), 170-174.

Zhang, C., 2010. High-quality oriented ZnO films grown by sol-gel process assisted with ZnO seed layer. J. Phys. Chem. Solids 71(3), 364-369.

Zhang, C., Li, X., Zhang, X., Yu, W., Zhao, J., 2006. Seed-layer induced growth of highly-quality oriented ZnO films by a sol-gel process. J. Cryst. Growth 290(1), 67-72.

Table 1. XRD patterns of ZnO nanowires synthesized on substrates covered with a 40 nm Au (111) film layer, and a ZnO seed layer film deposited by the RF cylindrical magnetron sputtering technique or the sol-gel spin coating technique for 1-6 min or 1-6 spin coats, respectively.

hkl	100	002*	101	102	110	103	004	203	114	105	213	006
RF cylindrical magnetron sputtering												
1 min	1.05	100	5.80	4.71	3.64	7.41	2.56	0.64	0.81	2.17	16.58	0.85
2 min	0.09	100	0.35	0.71	1.05	1.36	2.85	0.12	0.11	0.77	0.91	0.66
3 min	0.05	100	0.31	0.5	0.28	0.61	2.85	0.06	0.05	0.28	0.67	0.61
4 min	0.09	100	0.24	0.49	0.57	0.65	2.01	0.07	0.05	0.33	0.37	0.67
5 min	0.06	100	0.14	0.59	0.51	0.56	2.71	0.09	0.06	0.32	0.27	0.66
6 min	0.06	100	0.07	0.53	0.43	0.22	2.87	0.09	0.05	0.33	0.04	0.67
Sol-gel spin coating												
Seed 1	0.07	100	0.27	0.50	0.6	0.27	2.76	0.07	3.15	0.19	1.06	0.51
Seed 2	0.38	100	0.9	0.73	0.75	0.95	2.53	0.13	4.62	0.39	0.3	0.58
Seed 3	1.38	100	3.22	2.01	1.76	0.94	2.83	0.29	3.14	0.23	0.32	0.68
Seed 4	1.31	100	2.53	2.12	2.02	0.94	1.79	0.32	1.56	0.26	0.38	0.63
Seed 5	1.83	100	2.83	2.89	3.87	2.75	1.51	0.45	0.45	0.45	0.41	0.61
Seed 6	2.15	100	3.07	2.34	2.87	2.88	2.41	0.57	0.15	0.54	0.43	0.60

*XRD spectrums are normalized with respect to the (002) crystal plane.

Table 2. XRD patterns of ZnO nanowires synthesized on substrates covered with a 20, 40 or 60 nm Au (111) film layer, and a ZnO seed layer film deposited by the RF cylindrical magnetron sputtering technique for 3 min.

hkl	100	002*	101	102	110	103	004	203	114	105	213	006
Au thickness												
20 nm	0.98	100	5.31	4.25	2.18	11.51	2.99	0.59	0.89	2.987	0.39	0.66
40 nm	1.34	100	8.52	6.19	2.36	14.06	3.03	1.14	2.56	4.04	2.3	0.82
60 nm	1.99	100	10.91	8.76	11.24	17.34	2.66	1.34	3.19	3.98	4.77	0.86

*XRD spectrums are normalized with respect to the (002) crystal plane.

Table 3. XRD patterns of ZnO nanowires synthesized on substrates covered with a 40 nm Au (111) or 40 nm polycrystalline Au film, and a ZnO seed layer film deposited by the RF cylindrical magnetron sputtering technique for 3 min.

hkl	100	002*	101	102	110	103	004	203	114	105	213	006
Au orientation												
Au (Poly)	0.07	100	0.24	0.21	0.2	1.39	2.71	0.04	0.07	0.99	0.09	0.63
Au (111)	0.05	100	0.31	0.5	0.28	0.06	0.28	0.06	0.03	0.28	0.67	0.61

*XRD spectrums are normalized with respect to the (002) crystal plane.

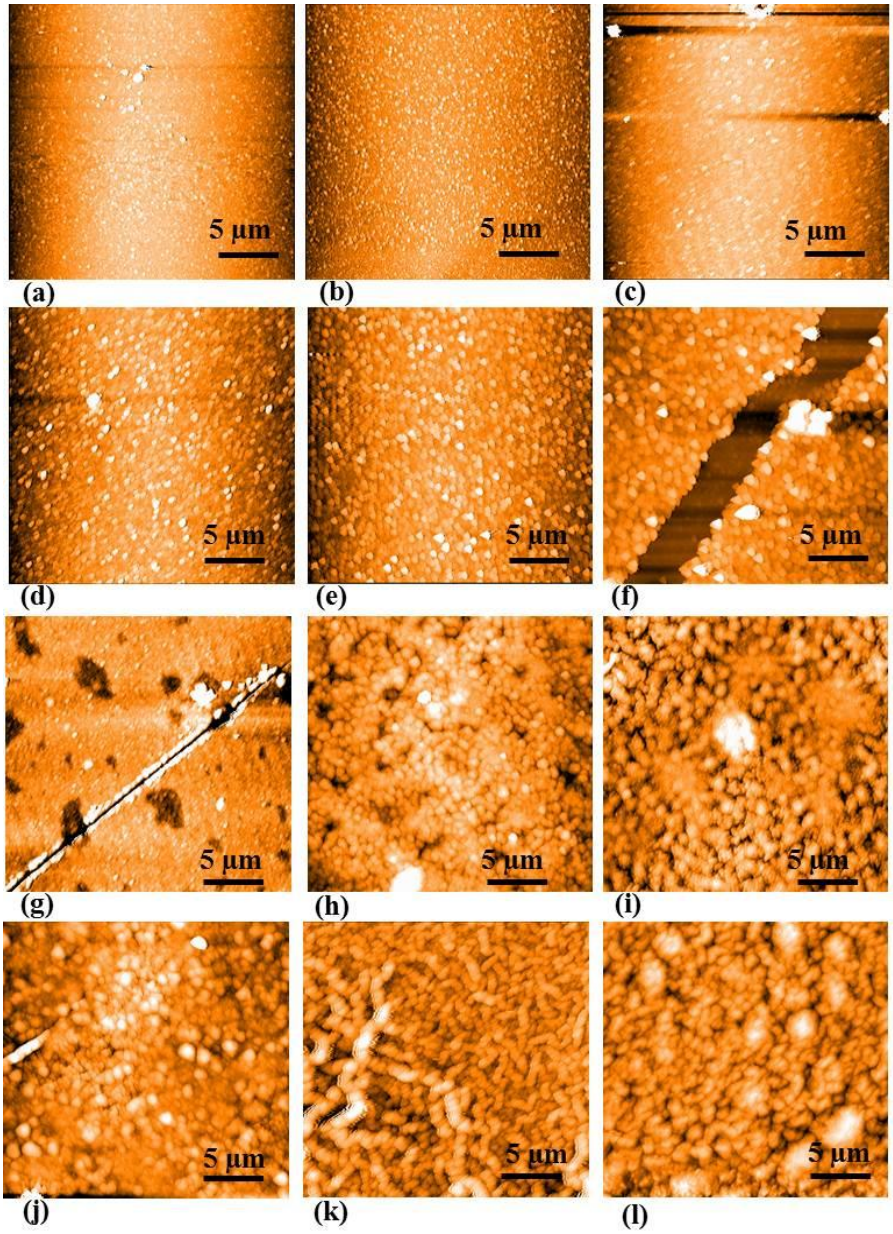

Fig. 1. AFM images of the surface topology of ZnO seed layer films deposited by the RF cylindrical magnetron sputtering technique for 1-6 min deposition (**a-f**, respectively) and the sol-gel spin coating technique for 1-6 spin coats (**g-l**, respectively).

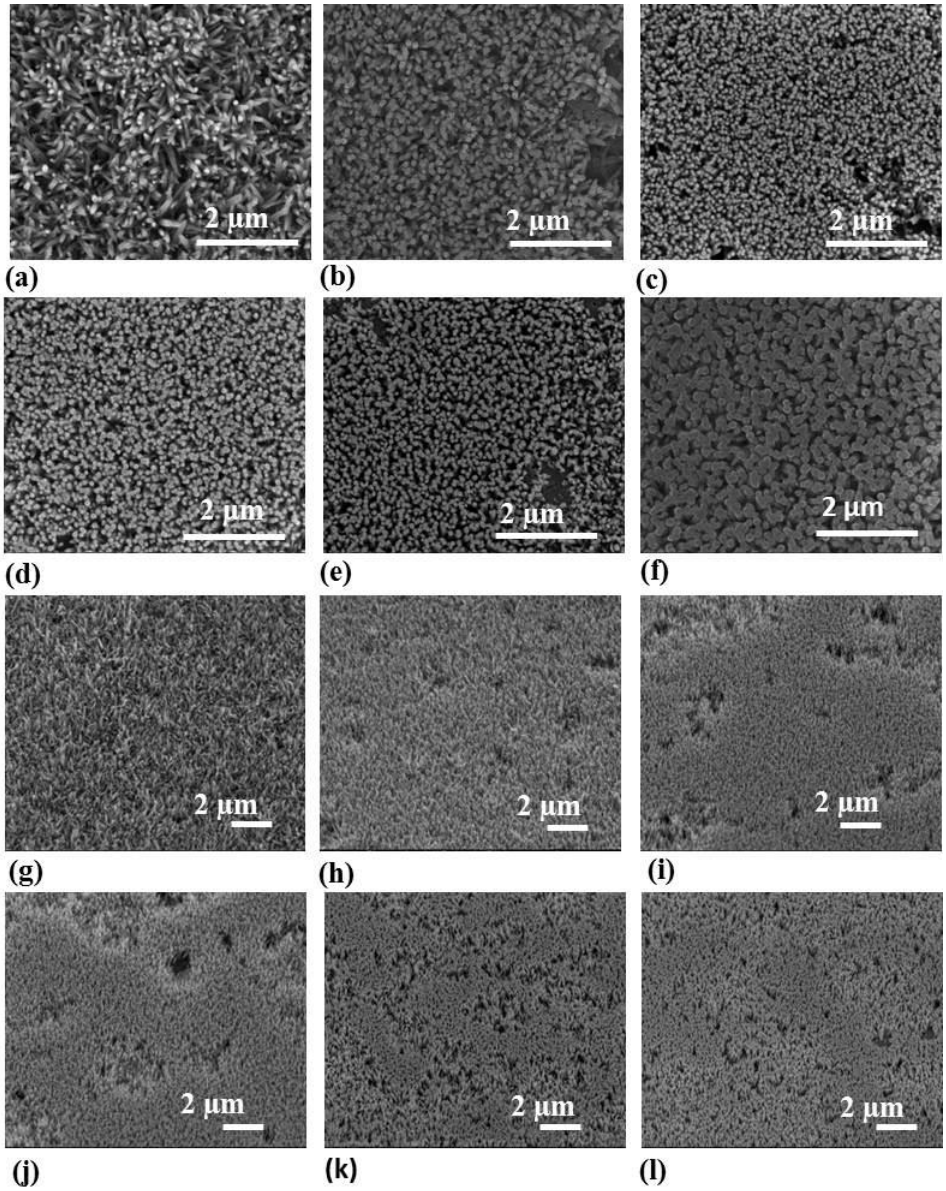

Fig. 2. High magnification top FEI-SEM images of vertically aligned ZnO nanowires grown using the hydrothermal growth method on substrates containing a 40 nm Au (111) film layer covered with a ZnO seed layer film deposited by the RF cylindrical magnetron sputtering technique for 1-6 min deposition (**a-f**, respectively). Low magnification tilted (45°) FEI-SEM images of the different deposition times are shown in **g-l**, respectively.

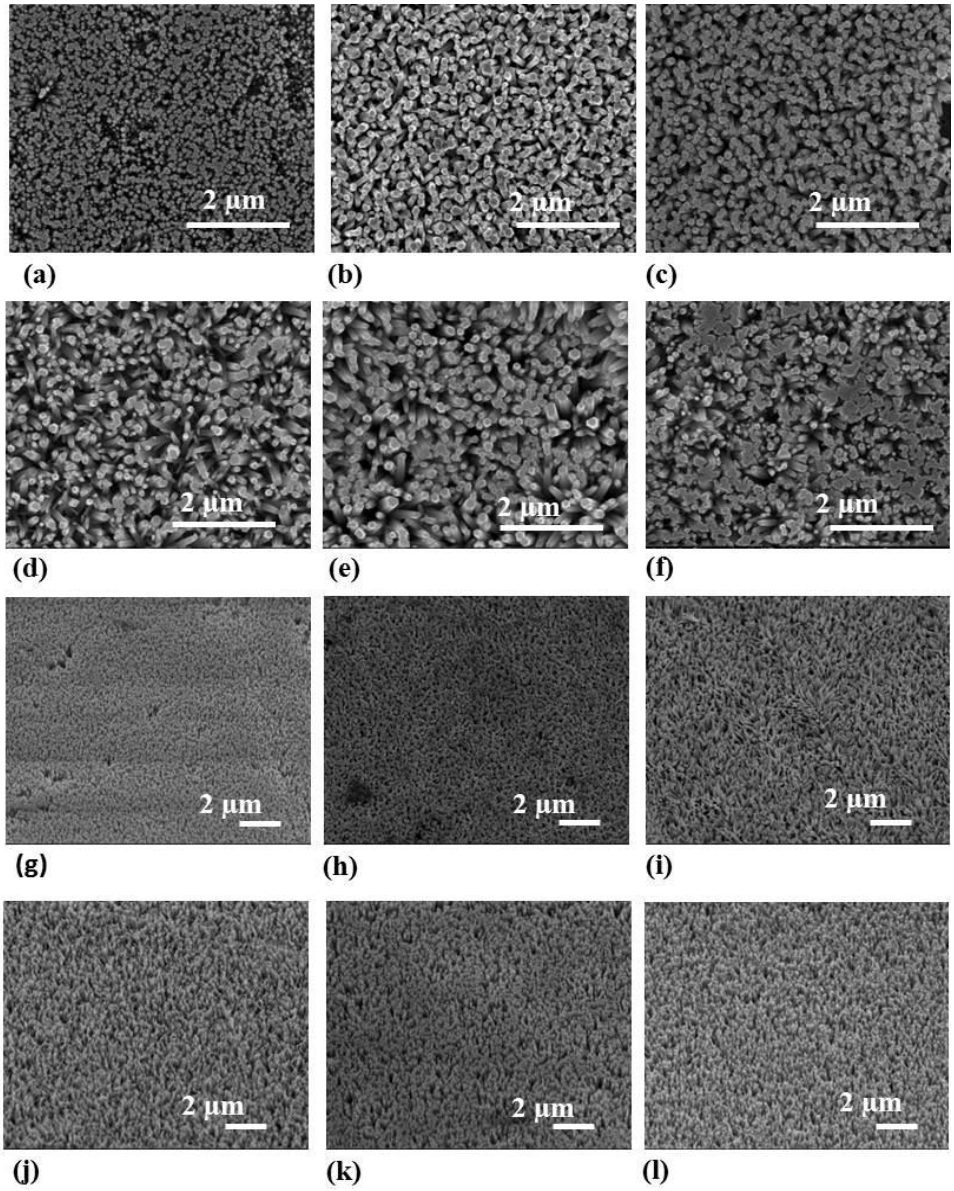

Fig. 3. High magnification top FEI-SEM images of vertically aligned ZnO nanowires grown using the hydrothermal growth method on substrates containing a 40 nm Au (111) film layer covered with a ZnO seed layer film deposited by the sol-gel spin coating technique for 1-6 spin coats (**a-f**, respectively). Low magnification tilted (45°) FEI-SEM images of the different spin coating times are shown in **g-l**, respectively.

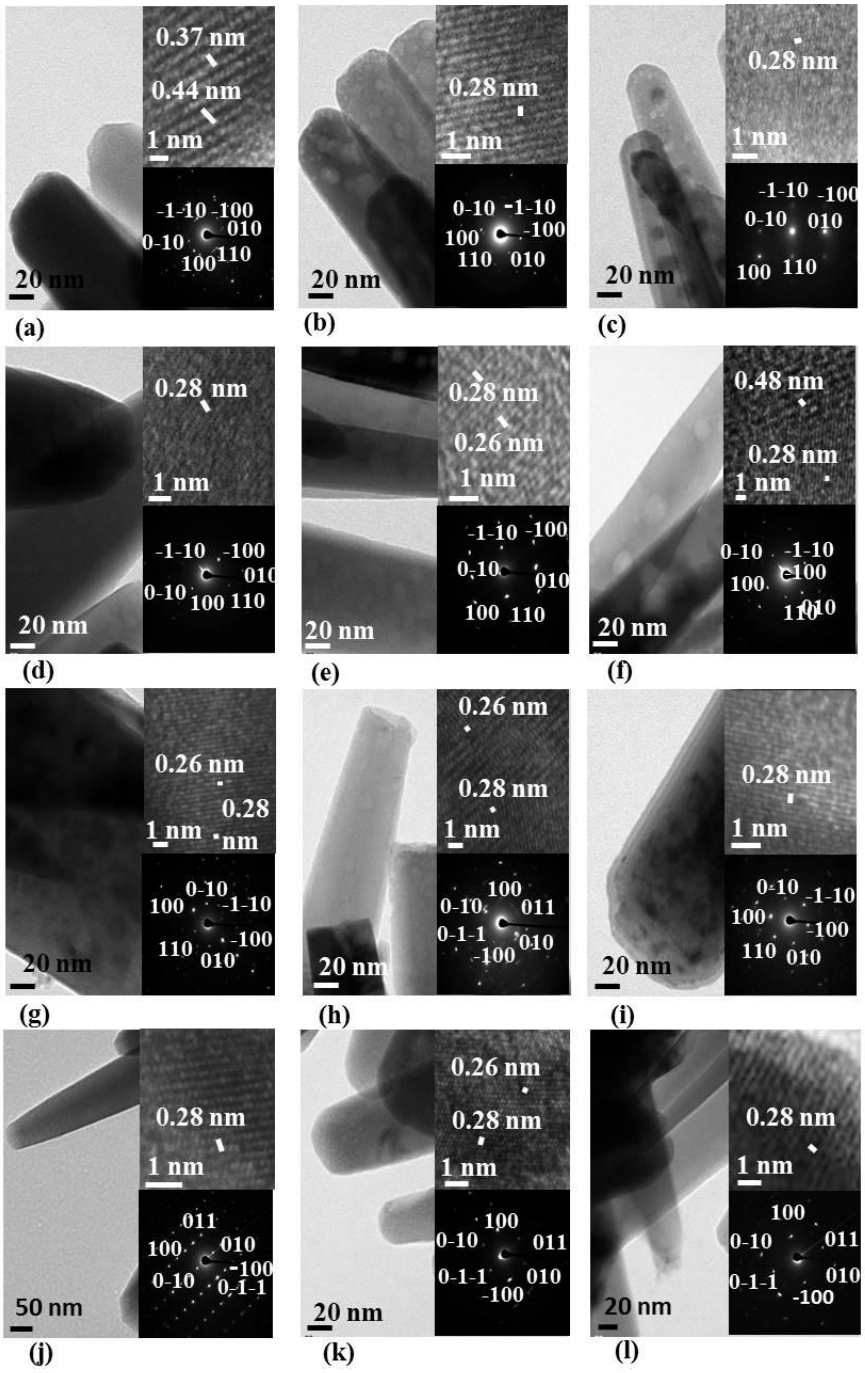

Fig. 4. TEM images of ZnO nanowires synthesized on substrates covered with a 40 nm Au (111) film layer covered with a ZnO seed layer film deposited by the RF cylindrical magnetron sputtering technique for 1-6 min (**a-f**, respectively) and the sol-gel spin coating technique for 1-6 spin coats (**g-l**, respectively). Corresponding HRTEM images and SAED patterns are shown.

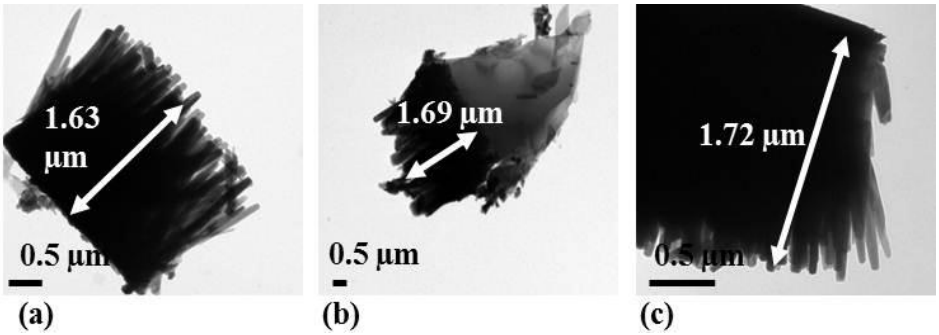

Fig. 5. TEM images of ZnO nanowires attached to the substrate surface which were grown on substrates containing a 40 nm Au (111) film layer covered by a ZnO seed layer film deposited for (**a**) 1 min by the RF cylindrical magnetron sputtering technique, (**b**) 1 spin coat by the sol-gel spin coating technique and (**c**) 3 min by the RF magnetron sputtering technique.

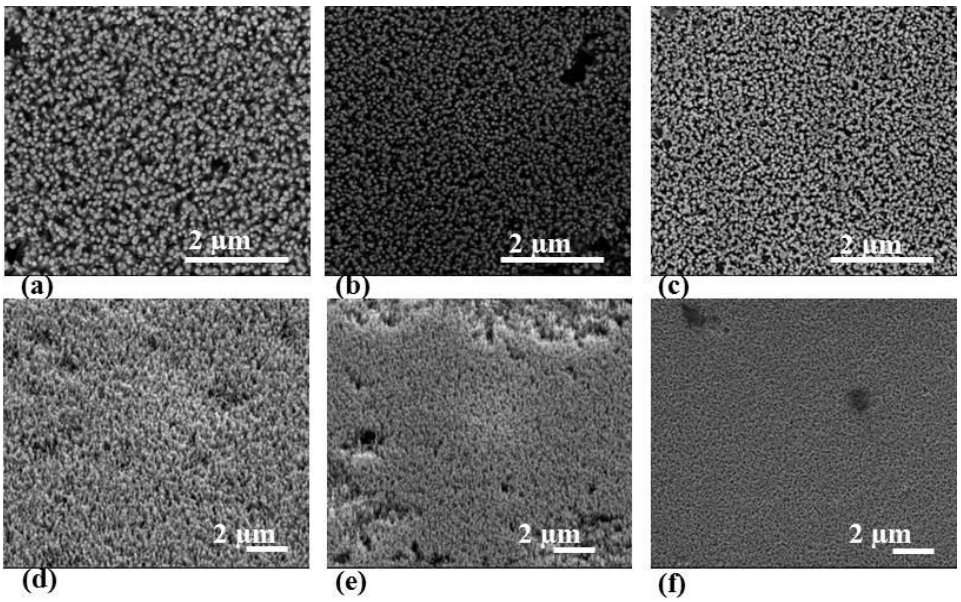

Fig. 6. High magnification top FEI-SEM images of vertically aligned ZnO nanowires grown by the hydrothermal growth approach on substrates covered with either (**a**) 20, (**b**) 40 or (**c**) 60 nm of Au (111) that were covered by a ZnO seed layer film deposited by the RF cylindrical magnetron sputtering technique for 3 min; (**d-f**) are low magnification tilted (45°) FEI-SEM images, respectively.

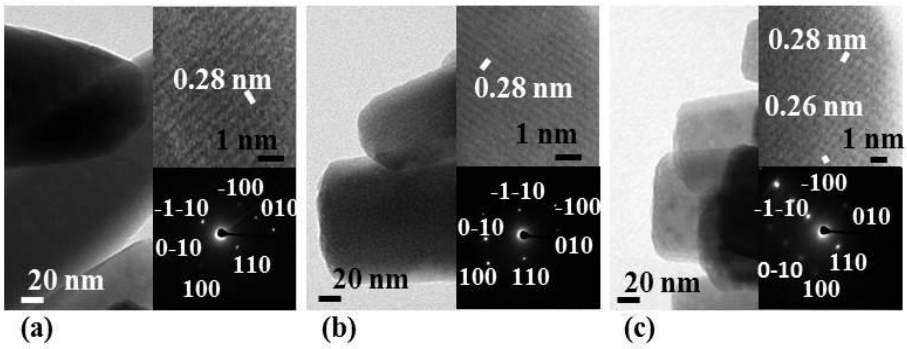

Fig. 7. TEM images of ZnO nanowires synthesized on substrates covered with either (**a**) 20, (**b**) 40 or (**c**) 60 nm of Au (111) film layers that were covered by a ZnO seed layer film deposited by the RF cylindrical magnetron sputtering technique for 3 min. Corresponding HRTEM images and SAED patterns are shown.

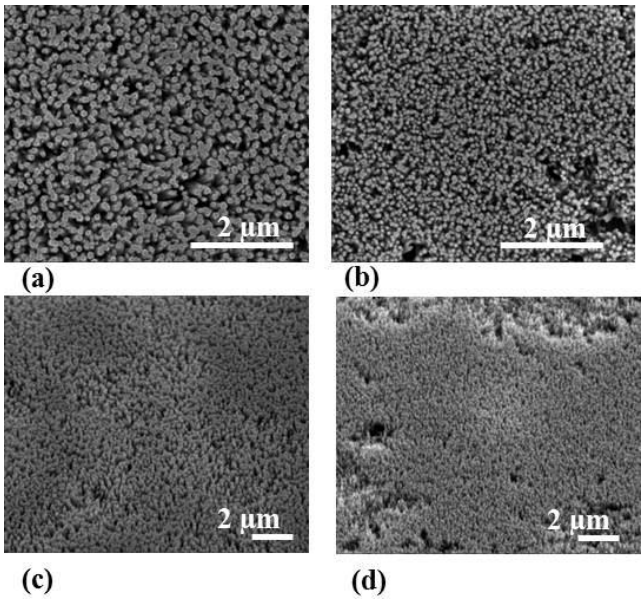

Fig. 8. High magnification top FEI-SEM images of vertically aligned ZnO nanowires grown by the hydrothermal growth approach on substrates covered with 40 nm of either (**a**) polycrystalline Au or (**b**) Au (111) that were covered by a ZnO seed layer film deposited by the RF cylindrical magnetron sputtering technique for 3 min, **c** and **d** are low magnification tilted (45°) FEI-SEM images, respectively.

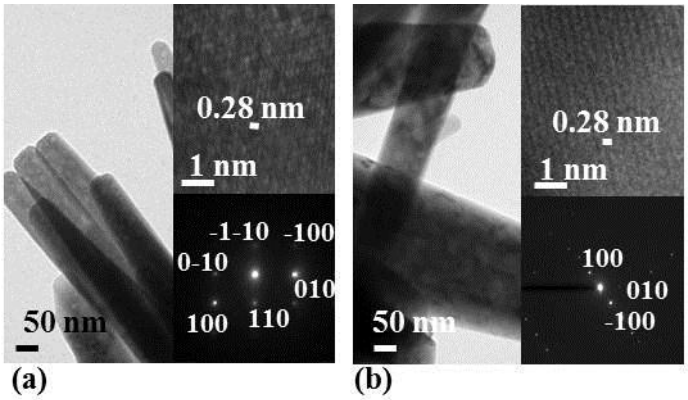

Fig. 9. TEM images of ZnO nanowires synthesized on (**a**) polycrystalline Au or (**b**) Au (111) that were covered by a ZnO seed layer film deposited by the RF cylindrical magnetron sputtering technique for 3 min. Corresponding HRTEM images and SAED patterns are shown.

CHAPTER 4

Immobilization of lysozyme to Au film layers using self-assembled monolayers

Immobilization of lysozyme to Au film layers using self-assembled monolayers

D.P. Neveling, L.M.T. Dicks

Department of Microbiology, University of Stellenbosch, Private Bag X1, Matieland 7602, Stellenbosch, South Africa

Abstract

Lysozyme was immobilized onto Au film layers by using self-assembled monolayers (SAMs). Combinations of alkanethiols (3-mercaptopropionic acid, 11-mercaptoundecanoic acid, 1-nonanethiol and 1-propanethiol) and dialkyl disulphides [bis-(10-carboxydecyl) disulphide] were compared to select the SAM that forms the strongest binding with primary amino groups of lysozyme. Lysozyme adhered strongly to 3-mercaptopropionic acid, but not to 11-mercaptoundecanoic acid/1-nonanethiol, as revealed by atomic force microscopy (AFM) and Fourier transform infrared (FTIR) spectroscopy. Staining with BacLight™ indicated that cells of *Micrococcus luteus* were killed when exposed to the immobilized lysozyme surface. Immobilized lysozyme may have lost its biological activity, however, the immobilized structure was not denatured as antibody recognition occurred. This suggested that killing of the cells was most probably inflicted by the gold film layer.

Introduction

The most challenging step during the development of biosensors is the immobilization of biomolecules in such a manner that they are positioned close to the surface, whilst retaining biological activity (Fransconi et al., 2010; Gooding and Hibbert, 1999; Rusmini et al., 2007; Wong et al., 2009). Proteins are easily denatured or inactivated during immobilization, mostly due to changes in tertiary structure (Jonkheijm et al., 2008; Rusmini et al., 2007; Sarma et al., 2009; Wong et al., 2009). Moreover, proteins adhere to surfaces through non-specific interactions, i.e. electrostatic interactions, hydrogen bonding and hydrophobic interactions (Mrksich, 2005). Self-assembled monolayers (SAMs) may shield proteins from direct contact with solid surfaces and thus reduce the possibility of denaturation (Katz et al., 1994).

Self-assembly is a process which involves the spontaneous arrangement of atoms and molecules in an ordered and functional structure, similar to the creation of life from basic building blocks (Samanta and Sarkar, 2011). Biological membranes, cellular structures and viruses are examples of sophisticated self-assembly systems (Vericat et al., 2010). Constuction of a SAM is the most elegant way of creating an organic thin film with specific surface properties onto which biomolecules can be immobilized (Flink et al., 2000; Gooding and Hibbert, 1999; Love et al., 2005; Ulman, 1996). Some control over the orientation and distribution of the immobilized protein is gained by this approach. The affinity of thiols for some metal surfaces (i.e. Au, Ag, Pt and Cu), particularly gold, makes alkanethiols ideal absorbates (Gooding and Hibbert, 1999) for SAMs. Numerous surface-active organosulphur compounds have been studied, e.g. alkanethiols, arenethiols, alkanedithiols, arenedithiols, dialkyl disulphides and dialkyl sulphides. Alkanethiols and dialkyl disulphides form similar structures. However, disulphides are less soluble and often lead to the formation of multilayers, whereas dialkyl sulphides form a weaker bond with gold in comparison to thiols and disulphides (Fransconi et al., 2010).

Self-assembled monolayer formation occurs in two steps, i.e. an initial fast step of absorption, followed by a slower step of monolayer organization (Godin et al., 2004; Schwartz, 2001). Initially, a small molecular density on the surface forms either a disordered mass of molecules, or an ordered two-dimensional horizontal phase (Schreiber, 2000; Schwartz, 2001). As more molecules absorb to the surface, the molecules start to form a three-dimensional crystalline or semi-crystalline structure on the surface (Schwartz, 2001;

Vos et al., 2003). The head groups assemble together, while the tail groups assemble far from the surface. Areas of close-packed molecules nucleate and grow until the surface of the substrate is covered in a single monolayer. A number of experimental factors affect the formation and the packing density of SAMs, i.e. the nature and surface roughness of the substrate (Hoogvliet et al., 2000), solvent used during assembly (Dannenberger et al., 1998), incubation temperature (Chen et al., 2000; Yamada et al., 2000), concentration and nature of the absorbate (Kim et al., 1993), immersion time (Kim et al., 1993) and the presence of oxygen (Lee et al., 1998).

Cleanliness and crystallinity of the substrate plays an important role in determining the compactness of the monolayer, as bare metal tends to absorb organic substances which results in monolayer defects (Creager et al., 1992; Guo et al., 1994; Lee et al., 1998; Ron and Rubinstein, 1998; Tsuneda et al., 1999; Yang et al., 1995). Well-defined, smooth substrates like Au (111) bind alkanethiols stronger than Au (100), resulting in higher SAM density and regularity (Hou et al., 1998; Lee et al., 1998). For smoother substrates, the density of defects are lower due to fewer grain boundaries, step edges and other surface features that cause defects in SAMs (Leopold and Bowden, 2002). Defects in monolayers include missing rows, vacancy Au islands, molecular defects and disorder (Vericat et al., 2005). Various solvents can be used for SAM formation. However, monolayers formed by low polar solvents have poor orientation in comparison to those formed in high polar solvents such as ethanol (Bain et al., 1989b; Dannenberger et al., 1998; Mamum and Hahn, 2012; Schneider and Buttry, 1993; Yamada et al., 1999). Increasing the reaction temperature above that of room temperature decreases the chance of monolayer defect fromation (Kang et al., 2010; Korolkov et al., 2010). At elevated temperatures the SAM domain and vacancy islands are larger, but the number of vacancy islands are less (Mamun and Hahn, 2012; Yamada et al., 2000).

Low concentrations of absorbates in the reaction solution and a longer immersion time produce regular shaped SAMs, whereas high concentrations of absorbates at shorter immersion times produce irregular SAMs (Bain et al., 1989b; Bensebaa et al., 1997). The formation of well-assembled monolayers also depends on the purity of the absorbate, as thiolated precursor impurities lack functional head groups and compete with the molecule of interest for available binding sites. Van der Waals forces between the alkyl chains enhance the stability and order of the absorbates. Thus, more alkyl chains in the absorbate [$HS(CH_2)_nX$, where $n \geq 10$] enhances the stability and regularity of the monolayer, whereas short chain lengths results in more molecular disorder (De Groot et al., 2007; Hong and Park,

2001; Nuzzo et al., 1987; Yue et al., 2008). The length of the aliphatic chain significantly influences the rate and extent of oxidation and desorption. Longer alkyl chain SAMs are more susceptible to oxidation (Wang et al., 2003). The presence of oxygen and the absence of light oxidizes thiolates and forms sulfonates ($-SO^{3-}$) and sulfinates ($-SO^{2-}$), which results in desorption of the SAM from the surface (Ron and Rubinstein, 1998; Wang et al., 2003).

Combined SAMs is a result of co-adsorption of two different absorbates of similar dimension, but with different terminal functional groups (one reactive and one inert). Combined SAMs provides a method to immobilize molecular species with physical dimensions which would normally prevent a well-organized assembly (Gooding et al., 2003). By varying the composition of a combined SAM, the density of attachment points can be controlled and, hence, also the surface loading of the protein (Gooding and Hibbert, 1999). The ratio of the two dissimilar molecules is usually proportional to the ratio of the initial concentration of the absorbates (Bain et al., 1989a; Wasserman et al., 1989).

Covalent attachment has the greatest potential for chemical conjugation, due to the stability of the bond (Fransconi et al., 2010; Samanta and Sarkar, 2011). The terminal functional groups of SAMs are often chemically modified to attach to biomoleclues. The enzyme either attaches to the SAM, or modified to contain thiol moieties that bind to the gold surface. The most common method to covalently attach proteins to surfaces involves the functionalization of SAM to form a reactive intermediate, which is then coupled to the biomolecule through specific amino acid side chain functional groups (Fransconi et al., 2010; Gooding and Hibbert, 1999). If the amino acid side chain functional group that is targeted for chemical conjugation is in high abundance ($\geq$ 10 %) the protein is attached through numerous residues simultaneously. This restricts the proteins degree of conformational freedom and additionally increases the heterogeneity of the immobilized population (Fransconi et al., 2010).

Different organic reactions have been explored to modify terminal functional groups of SAMs. These include nucleophilic substitutions, esterification, acylation and nucleophilic addition (Sullivan and Huck, 2003). Despite the advantages of chemical conjugation, the orientation of the immobilized protein is significantly affected by the choice of chemical linkers used to create a reactive intermediate-SAM as well as the conjugation sites in the protein targeted for covalent bonding (Fransconi et al., 2010; Gooding and Hibbert, 1999; Samanta and Sarkar, 2011). Conjugation of proteins through covalent binding lacks

regiospecificity and, hence, the immobilized proteins may not be correctly oriented. In addition, the reactive site of the protein may be blocked by the immobilization procedure, resulting in the reduction or loss of protein activity (Fransconi et al., 2010; Rusmini et al., 2007; Wong et al., 2009).

During this study different absorbates were used to create SAMs on Au (111) film layers to determine which monolayer immobilizes lysozyme the best. The alkanethiol reagents used were 3-mercaptopropionic acid, 11-mercaptoundecanoic acid, 1-nonanethiol and 1-propanethiol. The dialkyl disulphide reagent was bis-(10-carboxydecyl) disulphide. Combinations of 3-mercaptopropionic acid/cysteamine, 3-mercaptopropionic acid/1-propanethiol and 11-mercaptoundecanoic acid/1-nonanethiol were used to control the surface loading of the immobilized lysozyme. Self-assembled monolayers were reacted with chemical linking reagents to form intermediates reactive towards primary amino groups. Self-assembled monolayers were characterized by AFM and FTIR spectroscopy. Immobilized lysozyme was characterized by AFM, FTIR spectroscopy, fluorescence microscopy and a BacLight^{TM} bacterial viability assay.

Materials and Methods

Substrate preparation

Silicon (100) wafers were cut into 1 x 1 cm sizes and sonicated for 10 min in acetone, followed by sonication for 10 min in absolute ethanol and 10 min in distilled H_2O. The wafers were dried under N_2 and placed on a hot plate at 110 °C for 5 min. A 10 nm titanium (Ti) film layer was deposited by RF cylindrical magnetron sputtering at 2 x 10^{-2} mbar in the presence of 60 % argon at 50 V, - 400 V, 0.5 A, 100 W, 21 kHz and 100 W.

Substrates were cleaned by immersion in absolute ethanol for 10 sec, dried under N_2 (99.9 %) and placed on a hot plate at 110 °C for 5 min. Substrates were then coated with a thin film of Au (20 nm), by using a Quorum sputter coater (Quorum Technologies Ltd, West Sussex, UK) set at 1.5 kV and 20 mA under 2 x 10^{-1} mbar pressure in the presence of argon. Gold coated substrates were then cleaned by immersion in gold cleaning solution (Sigma Aldrich, Missouri, USA) for 30 sec and rinsed with distilled H_2O for 30 sec and dried under N_2.

SAM formation

Glass containers were cleaned with piranha solution [30:70 v/v H_2O_2 and H_2SO_4] to avoid contamination and rinsed three times with either absolute ethanol or dimethyl sulfoxide (DMSO, ≥ 99 %), depending on the SAM that was used. All absorbates used for SAM formation were ≥ 99 % purity, unless otherwise stated. The alkanethiols used for SAM formation were 3-mercaptopropionic acid, 11-mercaptoundecanoic acid, 1-nonanethiol and 1-propanethiol. The dialkyl disulphide used was bis-(10-carboxydecyl) disulphide (≥ 98 %).

Self-assembled monolayers were dissolved in absolute ethanol, with the exception of bis-(10-carboxydecyl) disulphide, which was dissolved in DMSO at 1 mM. Reaction solutions for carboxylic acid-terminated SAMs were adjusted to pH 2.0. Surface loading of the immobilized protein was assessed using combinations of SAMs, with one terminal group reactive and one inert that acted as a spacer. Combinations used for SAM formation contained 3-mercaptopropionic acid/cysteamine, 3-mercaptopropionic acid/propanethiol or 11-mercaptoundecanoic acid/nonanethiol, each at a ratio of 9:1 (reactive: inert group). The SAMs combinations were dissolved in absolute ethanol to 1 mM.

The solutions were sonicated at 25 °C for 5 min to dissolve the absorbate. The gold substrates were immersed in the SAM solution for 24 h at 25 °C under N_2. A vacuum was created in a Schlenk reaction vessel and filled with inert N_2. After incubation, SAM formation was terminated by rinsing the substrates three times with absolute ethanol or DMSO, depending on the solvent used during SAM formation, and dried under N2.

Protein immobilization

Carboxylic acid terminated SAMs were reacted with 5m M EDC [ethyl (dimethylaminopropyl) carbodiimide] and 5mM NHS (N-hydroxysuccinimide, ≥ 97 %) in absolute ethanol (pH 7.0) under N_2 at 25 °C for 3 h to form intermediates that would react with primary amino groups of lysozyme. EDC was used in combination with NHS to increase the coupling efficacy or to create a more stable reactive intermediate (Fig. 1 a).

Methyl terminal SAMs were reacted with 5 mM DSP (dithiobis [succinimidylpropionate]) in DMSO (pH 7) under N_2 at 25 °C for 3 h. Dithiobis

(succinimidylpropionate) exchanges with the bound SAMs for binding to the Au surface. The unreacted end of DSP reacted with the primary amino groups of lysozyme (Fig. 1 b).

Combined SAMs carboxylic acid functional groups reacted with NHS and EDC, as described before. The methyl and amine terminal groups were used as inert groups to control the immobilization rate of lysozyme.

Upon completion of SAM functionalization, substrates were rinsed with PBS solution (137 mM NaCl, 2.7 mM KCl, 10 mM $Na_2HPO_4 \cdot 2H_2O$, 2 mM KH_2PO_4, pH 7.2) for 10 sec. Substrates were placed in PBS solution containing 1 mg/ml lysozyme from hen egg white (Roche, Mannheim, Germany) and incubated at 4 °C for 24 h (in the presence of N_2). After immobilization of lysozyme, substrates were rinsed with PBS solution for 10 sec, dried under N_2 and stored at 4 °C in the presence of a N_2 atmosphere.

Characterization of SAM

The Au film layer crystal structure and phase composition was determined by XRD, using a Bruker AXS D8 Advance X-ray diffractometer operated in locked coupled mode (Bruker AXS, Frankfurt, Germany). The instrument was equipped with a Vantec-1 position sensitive detector optimized for Cu-Kα radiation with λ= 1.5406 Å. The X-ray tube was operated at 40 mA and 40 kV and the measurements were recorded at a scanning rate of 0.5 sec/step with a step size of 0.014° in a 2θ range extending from 31.28° to 149.3°.

Atomic force microscopy (AFM) images were collected with a Nanosurf AFM Easyscan 2 (Nanosurf Inc., California, USA) to assess the surface topology of the SAMs and to determine the surface roughness of the Au film layer. Images were acquired in tapping mode at a scan rate of 2 Hz with a Pt cantilever (spring constant of 0.06 N m^{-1}) with drive amplitude between 20-50 mV and set-points in the range of 0.14 V.

Infrared (IR) spectra of monolayers were obtained to confirm SAM formation and additionally to follow the chemical modification of the SAM functional groups. Attenuated Total Reflectance-Fourier-transform infrared (ATR-FTIR) spectra were recorded in the range of 500-4000 cm^{-1} by a Thermo Scientific Nicolet iS10 FTIR (Thermo Scientific Inc., Massachusetts, USA) spectrometer. ATR-FTIR spectra were collected using 250 scans with a

4 cm^{-1} resolution. FTIR spectra were background subtracted and corrected for atmospheric suppression using the OMNIC software (Thermo Scientific Inc., Massachusetts, USA).

Characterization of protein immobilization

Atomic force microscopy was used to measure the height increase in the SAMs after lysozyme had been immobilized. A Nanosurf AFM Easyscan 2 was used to characterize the SAMs, as describe before. Attenuated Total Reflectance-Fourier-transform infrared spectroscopy was used to determine if amide bond formation occurred and to assess the intensity of the remaining reactive intermediates which indicates the degree of protein immobilization. Attenuated Total Reflectance-Fourier-transform infrared spectra were collected with a Thermo Scientific Nicolet iS10 FTIR spectrometer, as described before.

Fluorescence microscopy was used to study the surface coverage of the immobilized protein. Lysozyme-SAM-Au substrates were incubated with 100 µg/ml rabbit primary lysozyme antibody serum (Rockland Immunochemicals Inc., Pennsylvania, USA) in casein-PBS solution (1 % casein in PBS solution, pH 7.2) for 30 min at 25 °C and then washed for 5 min in casein-PBS solution. The antibody-lysozyme-SAM-Au substrates were incubated with 10 µg/ml Alexa Fluor 488 goat anti rabbit H+L IgG (Life Technologies, California, USA) in casein-PBS solution for 30 min at 25 °C in the dark and then washed for 5 min in casein-PBS solution in the dark. Confocal images were acquired with a Carl Zeiss Confocal LSM 780 Elyra S1 scanning laser microscope equipped with a SR-SIM super resolution platform (Carl Zeiss, Oberkochen, Germany) using a 100 X oil-immersion lens. An argon multiline laser excited the Alexa Fluor 488 at 488 nm and emitted light detected at 493-630 nm.

A BacLight™ (Life Technologies, California, USA) bacterial viability assay, using *Micrococcus luteus* ATCC 4698, was used to study the biological function of the immobilized lysozyme. The cell wall of *M. luteus* contains a thick outer peptidoglycan layer. Degradation of this layer by lysozyme results in cell lysis and cell death. By measuring the degree of cell death, the degree of protein activity could be inferred. The bacteria were grown in nutrient broth for 12 h, incubated on a rotating wheel at 30 °C. Mid-exponential phase cells (2 x 10^8/ml) were collected at 9000 x g and washed with saline solution (8.5% NaCl). The cells were labelled with a BacLight™ bacterial viability kit, as per manufacturer instructions. Stained *M. luteus* cells were added to the immobilized lysozyme-SAM-Au substrates and

followed by fluorescence microscopy for 3 h, using a Carl Zeiss Confocal LSM 780 Elyra S1 scanning laser microscope to determine the degree of lysozyme activity (cell death). An argon multiline laser was used to excite syto9 at 488 nm (green) and propidium iodide at 514 nm (red). Green fluorescence, which represented live bacteria, was detected at 517-572 nm, while red fluorescence indicated dead bacteria and was detected at 646-709 nm.

Results and Discussions

X-ray diffraction analysis was conducted to determine the crystal structure and phase composition of the Au film layer (Table 1). Formation of SAMs on Au (111) film layers yielded SAMs with highest density and highest degree of regularity (Hou et al., 1998). The majority of the Au atoms were oriented as (111) crystal planes [94.808 %], with few atoms being (200) [0.067 %], (220) [0.071 %], (311) [0.087 %], (222) [4.714 %] and (420) [0.253 %] crystal planes. Based on these results, a more single-crystalline Au (111) film layer was deposited as opposed to an amorphous Au film layer.

Three-dimensional topographic images of a clean Au surface, a SAM and immobilized lysozyme surface are shown in Fig. 2 a-c, respectively. The average height of the deposited Au atoms was 4.5-5.0 nm, while the average height of bound SAMs was 5.5-6.0 nm. Monolayer formation increased the height of the Au film layer by 1 nm. The distance between a C-C bond is 120-154 pm (Weast, 1984). Thus, if a SAM contains 11 C-C bonds such as 11-mercaptoundecanoic acid, an average height increase of 1.32-1.69 nm can be expected. Similar results were obtained for all SAMs bound to the Au film layer surface. SAMs covalently immobilized with lysozyme showed an average height of 8.0-9.0 nm. An average height increase of 2.5-3.0 nm was observed between the SAMs and the immobilized protein. The lysozyme molecule has an ellipsoidal shape with dimensions of 2.8 x 3.2 x 3.0 nm and a volume of 2.7 x 10^{-20} cm^{-3} (Steinrauf, 1959). Similar results were obtained for all SAMs immobilized with lysozyme. These results indicated that lysozyme was covalently bound to the SAM surface.

Attenuated Total Reflectance-Fourier-transform infrared studies were conducted on separate substrates to confirm changes in the surface chemistry occurring after each modification step. FTIR analysis has been used extensively to investigate SAM formation and the reactions involving interfacial functional groups (Li et al., 2007; Moraillon et al.,

2008; Ngunjiri et al., 2013; Nguyen, 2012; Techane et al., 2011). The FTIR spectra shown in Figs 3 to 5 were used to verify the monolayer formation, activation of the SAMs with EDC/NHS or addition of DSP to the monolayer, and immobilization of lysozyme through amide bond formation.

Carboxylic acid-terminated SAM formation (Figs 3 and 4) was confirmed by the presence of peaks characteristic to carboxylic acid functional groups. Before activation with EDC/NHS, the carboxylic acid-terminated SAM spectrums exhibited a strong peak at 1700 cm^{-1}, which corresponds to the υ(C=O) free carboxylic acid stretch of carbonyls. Carbonyl stretching frequencies in this range are characteristic of dimerization or other intermolecular hydrogen bonding processes available to the carbonyl terminated SAM (Nuzzo et al., 1990). Additional peaks at 1310 and 1465 cm^{-1} were observed which belongs to alkane groups. The peak at 1310 cm^{-1} is assigned to the C-H scissor vibration mode for alkanes and the peak at 1465 cm^{-1} to methylene CH bending of methylene chains in the SAMs. The presence of these characteristic peaks indicates that carboxylic acid terminated SAMs formed on the Au surface.

Carboxylic acid-terminated SAMs, 3-mercaptopropionic acid (Fig. 3 a), 3-mercaptopropionic acid/1-propanethiol (Fig. 3 b), 3-mercaptopropionic acid/1-nonanethiol (Fig. 3 c), 11-mercaptoundecanoic acid (Fig. 4 a), 11-mercaptoundecanoic acid/1-nonanethiol (Fig. 4 b) and bis-(10-carboxydecyl) disulphide (Fig. 4 c) that underwent EDC/NHS esterification displayed different FTIR profiles. A strong peak at 1742 cm^{-1} was present which corresponded to the υ(C=O) asymmetric carbonyl stretch of NHS esters formed by the succinimidyl carbonyl group. Two smaller peaks were visible at 1830 cm^{-1} (NHS-ester carbonyl stretch) and 1782 cm^{-1} (NHS-ester C=O symmetric stretch), which are attributed to the band splitting of the ester carbonyl C=O stretching vibration. Additional bands appeared at 1733 cm^{-1} (ester C=O stretch of N-acylurea), 1760 cm^{-1} (anhydride antisymmetric C=O stretch) and 1804 cm^{-1} (anhydride symmetric C=O stretch) which are by-products of the EDC/NHS esterification. The presence of these characteristic peaks indicated that NHS esterification of the carboxylic acid groups formed. EDC reacts with the carboxylic acid functional groups to form *O*-acylurea intermediates which are converted to NHS-esters by reaction with NHS (Wang et al., 2011). Additionally, *O*-acylurea can also be converted to anhydrides by coupling with a neighbouring carboxylic acid group. Both NHS-esters and anhydrides couple with amine containing biomolecules to form a stable amide bond (Wang et al., 2011).

Formation of SAMs terminated with methyl functional groups were confirmed by the presence of characteristic peaks (Fig. 5). Methyl-terminated SAMs, 1-nonanethiol (Fig. 5 a) and 1-propanethiol (Fig. 5 b) showed a strong peak at 1430 cm^{-1}, which corresponds to $\delta(CH_3)$, the methyl deformation, and to $\rho_s(CH_2)$, the methylene scissor motions (Fig. 5). The presence of the 1430 cm^{-1} peak indicates that methyl-terminated SAMs are bound to the Au surface. Chemical modification of methyl terminated SAMs by the competition of DSP for binding sites to the Au surface showed different FTIR spectrums. Following the addition of DSP to the monolayer (Fig. 5), three bands appeared at 1809 cm^{-1} (anhydride symmetric C=O stretch), 1782 cm^{-1} (anhydride symmetric C=O stretch), and 1739 cm^{-1} (N-acylurea C=O stretch). The frequency of these bands corresponded to the C=O stretching vibration of ester groups. The presence of these characteristic bands confirms the binding of DSP to the Au surface.

For all SAMs (Fig. 3-5) the addition of lysozyme to the chemically activated surface resulted in the presence of characteristic bands at 1540 and 1650 cm^{-1}. The peak at 1650 cm^{-1} can be assigned to amide I (C=O stretch) and 1540 cm^{-1} to amide II (NH bend and CN stretch combined) modes. The presence of these two peaks indicated that lysozyme was covalently immobilized to the SAM and thus subsequently immobilized to the Au surface.

Fluorescence microscopy was used to assess the surface loading of lysozyme during use of different SAMs. The gold film layers immobilized with lysozyme were incubated with primary lysozyme antibodies and secondary lysozyme fluorescent antibody conjugates. The use of different SAMs resulted in different degrees of protein immobilization (Fig. 6). The length of the SAMs influences the compactness of the monolayer, and thus the amount of binding sites available for covalent immobilization (Vericat et al., 2010).

Fluorescence microscopy images of the different SAMs immobilized with lysozyme is shown in Fig. 6. The fluorescence intensity of the immobilized protein monolayer was determined to elucidate which SAM results in the most immobilized lysozyme. Self-assembled monolayer 3-mercaptoundecanoic acid (Fig. 6 a) had the highest relative fluorescence intensity at 11764 RFU (Relative fluorescence units), 3-mercaptoundecanoic acid/cysteamine (Fig. 6 b) at 8364 RFU, 3-mercaptoundecanoic acid/propanethiol (Fig. 6 c) at 10150 RFU, 11-mercaptoundecanoic acid (Fig. 6 d) at 5159 RFU, 11-mercaptoundecanoic acid/nonanethiol (Fig. 6 e) at 2381 RFU, bis-(10-carboxydecyl) disulphide (Fig. 6 f) at 8212 RFU, 1-nonanethiol (Fig. 6 g) at 11285 RFU and propanethiol (Fig. 6 h) at 8496 RFU.

A negative control was included to assess the non-specific binding of the fluorescent antibody conjugate to the Au surface (Fig. 6 i). The relative fluorescence intensity measured for non-specific binding of the fluorescent antibody conjugate was 30 RFU. These results indicated that fluorescence observed is due to the binding of the secondary antibody to the primary antibody that, in turn, is bound to the lysozyme molecule. An additional control was included in which the non-specific binding of lysozyme to the Au surface was assessed (Fig. 6 j). Lysozyme bound to a certain degree to the Au surface through non-specific interactions, i.e. electrostatic interactions, hydrogen bonding and hydrophobic interactions (Fransconi et al., 2010). However, compared to the relative fluorescence intensity of the SAMs (Fig. 6 a-h), the intensity for non-specific binding of lysozyme was low (587 RFU). These results indicated that the relative fluorescence intensities observed for the SAMs (Fig. 6 a-h) are due to the immobilization of the lysozyme to the SAMs, and not as a result of non-specific binding of lysozyme to the Au surface.

Sel-assembled monolayer 3-mercaptoundecanoic acid immobilized lysozyme the best, whereas combined SAM 11-mercaptoundecanoic acid/nonanethiol resulted in the lowest levels of immobilization. Controlling the surface loading of the protein, combined SAMs are used that utilizes one reactive functional group and one inert functional group. The reactive group is used to immobilize the protein, and the inert group is used as a spacer molecule (Fransconi et al., 2010). Combined SAMs 3-mercaptoundecanoic acid/cysteamine, 3-mercaptoundecanoic acid/propanethiol and 11-mercaptoundecanoic acid/nonanethiol resulted in lower relative fluorescence intensities as opposed to homogeneous SAMs 3-mercaptoundecanoic acid and 11-mercaptoundecanoic acid, respectively. SAM 3-mercaptoundecanoic acid had higher surface loading as opposed to 11-mercaptoundecanoic acid.

Longer SAMs with longer alkyl chains are more prone to oxidation as opposed to shorter chain SAMs (Wang et al., 2003; Zamborini and Crooks, 1998). Thus a lower surface loading is observed for SAM 11-mercaptoundecanoic acid. Self-assembled monolayer bis-(10-carboxydecyl) disulphide yielded high levels of protein immobilization (8212 RFU). However, the monolayer contained islands of high protein density which may be due to leaching of the protein from the surface or the immobilization of multiple lysozyme molecules by one bis-(10-carboxydecyl) disulphide molecule. Self-assembled monolayers nonanethiol and propanethiol resulted in high levels of protein immobilization. However, protein leaching from the surface was evident. For nonanethiol and propanethiol SAMs (Fig.

6 g-h, respectively) dark islands were present which represents areas of less surface loading or areas of protein leaching.

The immobilized lysozyme activity was assessed using a BacLight™ bacterial viability assay. *Micrococcus luteus* ATCC 4698 was deposited onto the gold film layers immobilized with lysozyme and examined for 3 h by fluorescence microscopy (Fig. 7-8). *Micrococcus luteus* has a thick peptidoglycan layer. Lysozyme hydrolyses alternating polysaccharide copolymers of *N*-acetyl glucosamine and *N*-acetyl muramic acid which is the basic subunits of peptidoglycan the polysaccharide structure of the bacterial cell wall (Schlegel, 1993; Seltmann and Holst, 2002).

Green cells indicate bacteria that are alive and red cells indicate bacteria that are dead. The green fluorescence intensities of the cells decreased over time with no significant increase in the presence of red cells (Fig. 7-8). Lysozyme cleaves the cell wall component of the bacterial cells leaving the plasma membrane exposed. The red fluorescence stain propidium iodide only binds to membranes that are compromised. Degradation of the cell walls by lysozyme would result in the formation of protoplast; which would undergo cytolysis resulting in the binding of the red fluorescence stain.

Red cells were present for SAMs; 3-mercaptopropionic acid (Fig. 7 a), 3-mercaptopropionic acid/1-propanethiol (Fig. 7 c), 11-mercaptoundecanoic acid (Fig. 7 d), 11-mercaptoundecanoic acid/1-nonanethiol (Fig. 7 e), bis-(10-carboxydecyl) disulphide (Fig. 8 a) and 1-nonanethiol (Fig. 8 b) that were immobilized with lysozyme. No red cells were observed for SAMs, 3-mercaptopropionic acid/cysteamine (Fig. 7 b) and 1-propanethiol (Fig. 8 c). The death of these cells may be due to either lysozyme degradation of the cell wall or due to the exposure to the antibacterial Au film layer surface.

Table 2 contains the measured relative green fluorescence intensities of the *M. luteus* cells suspended on different SAMs immobilized with lysozyme, which were followed for 1-3 hours by fluorescence microscopy. A general trend was observed in which the green fluorescence intensity decreases over time. The decrease in the fluorescence intensities may be attributed to the hydrolysis of cell walls by lysozyme, the exposure to the antibacterial Au surface or quenching of the fluorescent dye.

M. luteus cells were suspended on a clean gold sample to act as a control (Fig. 8 d). *M. luteus* cells die faster than cells suspended on Au film layers immobilized with lysozyme. It

seems that the immobilized lysozyme film and SAM protects the bacterial cells from direct contact with the Au film layer. It is well know that Au has antibacterial properties. Gold nanoparticles exert their antibacterial activities mainly by causing a collapse of the membrane potential, inhibiting ATPase activities which results in the decrease in ATP levels, and inhibit the ribosome subunit from binding tRNA (Cui et al., 2012). Thus, in essence the use of a bacterial viability assay to determine the enzyme activity is trivial. *M. luteus* cells die much faster on Au film layers as opposed to cells suspended on lysozyme film layers. The decrease in cell viability could be due to the exposure to lysozyme, exposure to the antibacterial Au film layer or due to quenching of the fluorescent dye. Alternative methods should be employed to study the immobilized lysozyme activity. Techniques which assess the degradation of peptidoglycan could be used to determine the activity of the immobilized protein, or techniques which determine the three-dimensional structure could be used to assess the stability of the immobilized protein.

Conclusion

Self-assembled monolayers 3-mercaptopropionic acid, 3-mercaptopropionic acid/cysteamine, 3-mercaptopropionic acid/1-propanethiol, 11-mercaptoundecanoic acid, 11-mercaptoundecanoic acid/1-nonanethiol, bis-(10-carboxydecyl) disulphide, 1-nonanethiol and 1-propanethiol were formed on Au (111) film layers. Atomic force microscopy studies confirmed the binding of SAMs to the Au (111) surface as well as the covalent immobilization of lysozyme to the SAMs. Attenuated Total Reflectance-Fourier-transform infrared spectroscopy studies also indicated the binding of SAMs to the Au surface, chemical modification of the SAMs by EDC/NHS or the addition of DSP to the monolayer, and the covalent immobilization of lysozyme to the SAMs. Fluorescence microscopy concluded that a high degree of lysozyme was immobilized.

Self-assembled monolayer 3-mercaptopropionic acid resulted in the most immobilized lysozyme. Whereas 11-mercaptoundecanoic acid/1-nonanethiol SAM resulted in the worst immobilization. The use of combined SAMs resulted in the decrease in the surface loading of the lysozyme. Self-assembled monolayer bis-(10-carboxydecyl) disulphide resulted in a high degree of protein immobilization, however, islands containing high levels of protein loading was observed. This is as a result of two attachment sites on the SAM molecule being available for covalent attachment. Self-assembled monolayers 1-nonanethiol and 1-

propanethiol resulted in high degrees of protein immobilization, however, numerous gold vacancy islands were present which suggested that protein leaching occurred or the absorbates bound less strongly to the Au surface. A BacLight^{TM} bacterial viability assay used to determine the lysozyme enzyme activity was inconclusive as the gold layer possesses antibacterial properties. The decrease in the green fluorescent intensity of *M. luteus* cell could be attributed to cell wall degradation by lysozyme, exposure to the antibacterial Au film surface or quenching of the fluorescent dye. Alternative techniques to assess the enzyme activity should be employed to study the activity of the immobilized enzyme. Techniques which follow the degradation of peptidoglycan or which assesses the three-dimensional structure could elucidate the activity and stability of the immobilized enzyme. These findings have shown that the type of absorbate used for SAM formation has to be selected carefully. Chain length, molecular stability and the chemical reactions involved in activating the terminal functional groups determines the degree of protein immobilization.

References

Bain, C.D., Evall, J., Whitesides, G.M., 1989a. Formation of monolayers by the coadsorption of thiols on gold: variation in the head group, tail group, and solvent. J. Am. Chem. Soc. 111(18), 7155-7164.

Bain, C.D., Troughton, E.B., Tao, Y.T., Evall, J., Whitesides, G.M., Nuzzo, R.G., 1989b. Formation of monolayer films by the spontaneous assembly of organic thiols from solution onto gold. J. Am. Chem. Soc. 111(1), 321-335.

Bensebaa, F., Voicu, R., Huron, L., Ellis, T.H., Kruus, E., 1997. Kinetics of formation of long-chain n-alkanethiolate monolayers on polycrystalline gold. Langmuir 13(20), 5335-5340.

Chen, S., Li, L., Boozer, C.L., Jiang, S., 2000. Controlled chemical and structural properties of mixed self-assembled monolayers of alkanethiols on Au(111). Langmuir 16(24), 9287-9293.

Creager, S.E., Hocket, L.A., Rowe, G.K., 1992. Consequences of microscopic surface roughness for molecular self-assembly. Langmuir 8(3), 854-861.

Cui, Y., Zhao, Y., Tian, Y., Zhang, W., Lü, X., Jiang, X., 2012. The molecular mechanism of action of bactericidal gold nanoparticles on Escherichia coli. Biomaterials 33, 2327-2333.

Dannenberger, O., Wolff, J.J., Buck, M., 1998. Solvent dependence of the self-assembly process of an endgroup-modified alkanethiol. Langmuir 14(17), 4679-4682.

De Groot, M.T., Evers, T.H., Merkx, M., Koper, M.T.M., 2007. Electron transfer and ligand binding to cytochrome c immobilized on self-assembled monolayers. Langmuir 23(2), 729-736.

Flink, S., van Veggel, F.C.J.M., Reinhoudt, D.N., 2000. Sensor functionalities in self-assembled monolayers. Adv. Mater. 12(18), 1315-1328.

Fransconi, M., Mazzei, F., Ferri, T., 2010. Protein immobilization at gold-thiol surfaces and potential for biosensing. Anal. Bioanal. Chem. 398(4), 1545-1564.

Godin, M., Williams, P.J., Tobard-Cossa, V., Laroche, O., Beaulieu, L.Y., Lennox, R.B., Grütter, P., 2004. Surface stress, kinetics, and structure of alkanethiol self-assembled monolayers. Langmuir 20(17), 7090-7096.

Gooding, J.J., Hibbert, D.B., 1999. The application of alkanethiol self-assembled monolayers to enzyme electrodes. Trends in Analytical Chem. 18(8), 525-533.

Gooding, J.J., Mearns, F., Yang, W., Liu, J., 2003. Self-assembled monolayers into the 21st century: recent advances and applications. Electroanalysis 15(2), 81-96.

Guo, L., Facci, J.S., McLendon, G., Mosher, R., 1994. Effect of gold topography and surface pretreatment on the self-assembly of alkanethiol monolayers. Langmuir 10(12), 4588-4593.

Hong, H., Park, W., 2001. Electrochemical characteristics of hydroquinone-terminated self-assembled monolayers on gold. Langmuir 17(8), 2485-2492.

Hoogvliet, J.C., Dijksma, M., Kamp, B., van Bennekom, W.P., 2000. Electrochemical pretreatment of polycrystalline gold electrodes to produce a reproducible surface roughness for self-assembly: a study in phosphate buffer pH 7.4. Anal. Chem. 72(9), 2016-2021.

Hou, Z., Abbott, N.L., Stroeve, P., 1998. Electroless gold as a substrate for self-assembled monolayers. Langmuir 14(12), 3287-3297.

Jonkheijm, P., Weinrich, D., Schröder, H., Niemeyer, C.M., Waldmann, H., 2008. Chemical strategies for generating protein biochips. Angew. Chem. Int. Ed. 47(50), 9618-9647.

Kang, H., Lee, N., Ito, E., Hara, M., Noh, J., 2010. Formation and superlattice of long-range-ordered self-assembled monolayers of pentafluorobenzenethiols on Au(111). Langmuir 26(5), 2983-2985.

Katz, E., Schlereth, D.D., Schmidt, H., 1994. Electrochemical study of pyrroloquinoline quinone covalently immobilized as a monolayer onto cystamine-modified gold electrode. J. Electroanal. Chem. 367(1-2), 59-70.

Kim, Y.T., McCarley, R.L., Bard, A.J., 1993. Observation of n-octadecanethiol multilayer formation from solution onto gold. Langmuir 9(8), 1941-1944.

Korolkov, V.V., Allen, S., Roberts, C.J., Tendler, S.J.B., 2010. Subsecond self-assembled monolayer formation. J. Phys. Chem. C. 114(45), 19373-19377.

Lee, M., Hsueh, C., Freund, M.S., Ferguson, G.S., 1998. Air oxidation of self-assembled monolayers on polycrystalline gold: the role of the gold substrate. Langmuir 14(22), 6419-6423.

Leopold, M.C., Bowden, E.F., 2002. Influence of gold substrate topography on the voltammetry of cytochrome c absorbed on carboxylic acid terminated self-assembled monolayers. Langmuir 18(6), 2239-2245.

Li, D., He, Q., Cui, Y., Duan, L., Li, J., 2007. Immobilization of glucose oxidase onto gold nanoparticles with enhanced thermostability. Biochem. Bioph. Res. Co. 355(2), 488-493.

Love, J.C., Estroff, L.A., Kriebel, J.K., Nuzzo, R.G., Whitesides, G.M., 2005. Self-assembled monolayers of thiolates on metals as a form of nanotechnology. Chem. Rev. 105(4), 1103-1170.

Mamun, A.H.A., Hahn, J.R., 2012. Effects of immersion temperature on self-assembled monolayers of octanethiol on Au(111). Surface Science 606(5-6), 664-669.

Moraillon, A., Gouget-Laemmel, A.C., Ozanam, F., Chazalviel, 2008. Amidation of monolayers on silicon in physiological buffers: a quantitative IR study. J. Phys. Chem. C 112, 7158-7167.

Mrksich, M., 2005. Dynamic substrates for cell biology. MRS Bull. 30(3), 180-184.

Ngunjiri, J.N., Stark, D.J., Tian, T., Briggman, K.A., Garno, J.C., 2013. Immobilization of proteins on carboxylic acid functionalized nanopatterns. Anal. Bioanal. Chem. 405, 1985-1993.

Nguyen, K.C., 2012. Quantitative analysis of COOH-terminated alkanethiol SAMs on gold nanoparticle surfaces. Adv. Nat. Sci.: Nanosci. Nanotechnol. 3, 045008.

Nuzzo, R.G., Dubois, L.H., Allara, D.L., 1990. Fundamental studies of microscopic wetting on organic surfaces, formation and structural characterization of a self-consistent series of polyfunctional organic monolayers. J. Am. Chem. Soc. 112(2), 558-569.

Nuzzo, R.G., Zegarski, B.R., Dubois, L.H., 1987. Fundamental studies of the chemisorption of organosulfur compounds on gold(111), implications for molecular self-assembly on gold surfaces. J. Am. Chem. Soc. 109(3), 733-740.

Ron, H., Rubinstein, I., 1998. Self-assembled monolayers on oxidized metals, alkylthiol and dialkyl disulphide assembly on gold under electrochemical conditions. J. Am. Chem. Soc. 120(51), 13444-13452.

Rusmini, F., Zhong, Z., Feijen, J., 2007. Protein immobilization strategies for protein biochips. Biomarcomolecules 8(6), 1775-1789.

Samanta, D., Sarkar, A., 2011. Immobilization of bio-macromolecules on self-assembled monolayers: methods and sensor applications. Chem. Soc. Rev. 40, 2567-2592.

Sarma, A.K., Vatsyayan, P., Goswami, P., Minteer, S.D., 2009. Recent advances in material science for developing enzyme electrodes. Biosens. Bioelectron. 24(8), 2313-2322.

Schlegel, H.G., 1993. General Microbiology, 2nd edition Cambridge University Press, United Kingdom.

Schneider, T.W., Buttry, D.A., 1993. Electrochemical quartz crystal microbalance studies of adsorption and desorption of self-assembled monolayers of alkyl thiols on gold. J. Am. Chem. Soc. 115(26), 12391-12397.

Schreiber, F., 2000. Structure and growth of self-assembling monolayers. Prog. Surf. Sci. 65(5-8), 151-257.

Schwartz, D.K., 2001. Mechanisms and kinetics of self-assembled monolayer formation. Annu. Rev. Phys. Chem. 52, 107-137.

Seltmann, G., Holst, O., 2002. The bacterial cell wall, Springer-Verlag, Germany.

Steinrauf, L.K., 1959. Preliminary X-ray data for some new crystalline forms of β-lactoglobulin and hen-egg-white lysozyme. Acta Crystallogr. 12, 77-79.

Sullivan, T.P., Huck, W.T.S., 2003. Reactions on monolayers: organic synthesis in two dimensions. Eur. J. Org. Chem. 2003(1), 17-29.

Techane, S.D., Gamble, L.J., Castner, D.G., 2011. Multitechnique characterization of self-assembled carboxylic acid-terminated alkanethiol monolayers on nanoparticle and flat gold surfaces. J. Phys. Chem. C 115, 9432-9441.

Tsuneda, S., Ishida, T., Nishida, N., Hara, M., Sasabe, H., Knoll, W., 1999. Tailoring of a smooth polycrystalline gold surface as a suitable anchoring site for self-assembled monolayer. Thin Solid Films 339(1-2), 142-147.

Ulman, A., 1996. Formation and structure of self-assembled monolayers. Chem. Rev. 96(4), 1533-1554.

Vericat, C., Vela, M.E., Benitez, G., Carro, P., Salvarezza, R.C., 2010. Self-assembled monolayers of thiols and dithiols on gold: new challenges for a well-known system. Chem. Soc. Rev. 39, 1805-1834.

Vericat, C., Vela, M.E., Salvarezza, R.C., 2005. Self-assembled monolayers of alkanethiols on Au(111): surface structures, defects and dynamics. Phys. Chem. Chem. Phys. 7, 3258-3268.

Vos, J.G., Forster, R.J., Keyes, T.A., 2003. Interfacial Supramolecular Assemblies, Wiley, New York.

Wang, C., Yan, Q., Liu, H., Zhou, X., Xiao, S., 2011. Different EDC/NHS activation mechanisms between PAA and PMMA brushes and the following amidation reactions. Langmuir 27(19), 12058-12068.

Wang, M.C., Liao, J.D., Weng, C.C., Klauser, R., Shaporenko, A., Grunze, M., Zharnikov, M., 2003. Modification of aliphatic monomolecular films by free radical dominant plasma: the effect of the alkyl chain length and the substrate. Langmuir 19(23), 9774-9780.

Wasserman, S.R., Tao, Y.T., Whitesides, G.M., 1989. Structure and reactivity of alkylsiloxane monolayers formed by reaction of alkyltrichlorosilanes on silicon substrates. Langmuir 5(4), 1074-1087.

Weast, R.C., 1984. Handbook of Chemistry and Physics, 65 th edition CRC Press, Florida, USA.

Wong, L.S., Khan, F., Micklefield, J., 2009. Selective covalent protein immobilization: strategies and applications. Chem. Rev. 109(9), 4025-4053.

Yamada, R., Sakai, H., Uosaki, K., 1999. Solvent effect on the structure of the self-assembled monolayer of alkanethiol. Chem. Lett. 28(7), 667-668.

Yamada, R., Wano, H., Uosaki, K., 2000. Effect of temperature on structure of the self-assembled monolayer of decanethiol on Au(111) surface. Langmuir 16(13), 5523-5525.

Yang, Z., Gonzalez-Cortes, A., Jourquin, G., Viré, J., Kauffmann, J., Delplancke, J., 1995. Analytical application of self assembled monolayers on gold electrodes: critical importance of surface pretreatment. Biosens. Bioelectron. 10(9-10), 789-795.

Yue, H., Waldeck, D.H., Schrock, K., Kirby, D., Knorr, K., Switzer, S., Rosmus, J., Clark, R.A., 2008. Multiple sites for electron tunnelling between cytochrome c and mixed self-assembled monolayers. J. Phys. Chem. C. 112(7), 2514-2521.

Zamborini, F.P., Crooks, R.M., 1998. Corrosion passivation of gold by n-alkanethiol self-assembled monolayers: effect of chain length and end group. Langmuir 14, 3279-3286.

Table 1. XRD spectrum of deposited Au film layer.

2-theta	hkl	Intensity (%)
38.18	111	94.808
44.39	200	0.067
64.58	220	0.071
77.54	311	0.087
81.72	222	4.714
115.26	420	0.253

Table 2. Relative green fluorescence intensities of *M. luteus* cells suspended on different SAMs immobilized with lysozyme, and followed for 1-3 hours by fluorescence microscopy.

	RFU*			
Self-assembled monolayer (SAM)	T=0	T=1	T=2	T=3
3-mercaptoundecanoic acid	75.46	17.31	9.65	7.1
3-mercaptoundecanoic acid/cysteamine	110	25.92	13.9	9.14
3-mercaptoundecanoic acid/propanethiol	123	27.36	14.7	9.44
11-mercaptoundecanoic acid	122	21.56	12.4	9.53
11-mercaptoundecanoic acid/nonanethiol	157	10.19	8.26	0.02
bis-(10-carboxydecyl) disulphide	82.67	11.72	5.52	1.08
1-nonanethiol	72	16.82	10.1	4.19
1-propanethiol	96	14.34	11	4.53

* Relative fluorescence units

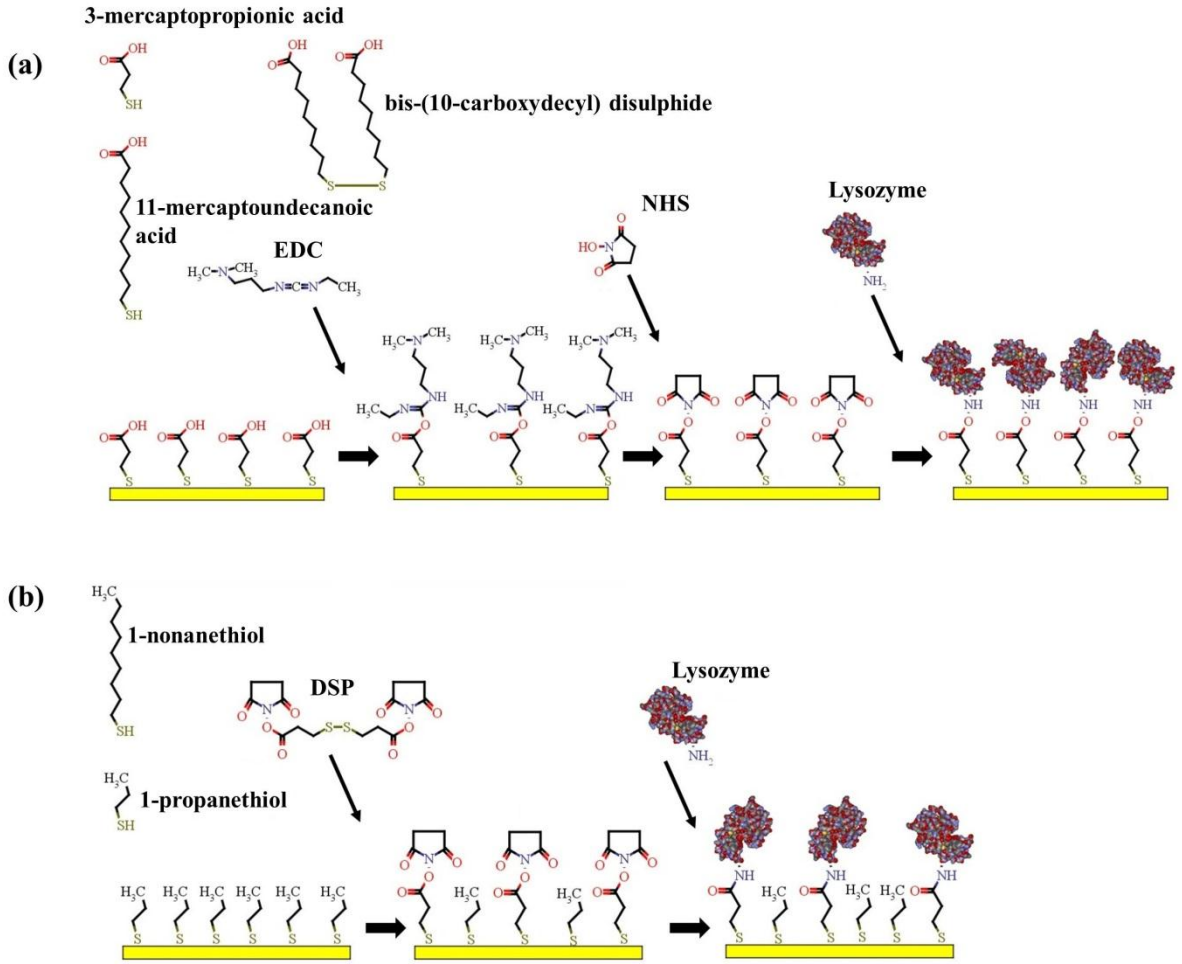

Fig. 1. Schematic representation of the lysozyme immobilization procedures. (**a)** Carboxylic acid terminated SAMs reacted with EDC (ethyl [dimethylaminopropyl] carbodiimide) and NHS (N-hydroxysuccinimide) to form SAM-intermediates reactive towards primary amino groups of lysozyme. (**b**) Methyl terminated SAMs reacted with DSP which exchanges with the bound SAM for binding sites on the Au surface. The unreacted end of DSP (dithiobis-[succinimidylpropionate]) reacts with the primary amino groups of lysozyme to form a covalent amide bond.

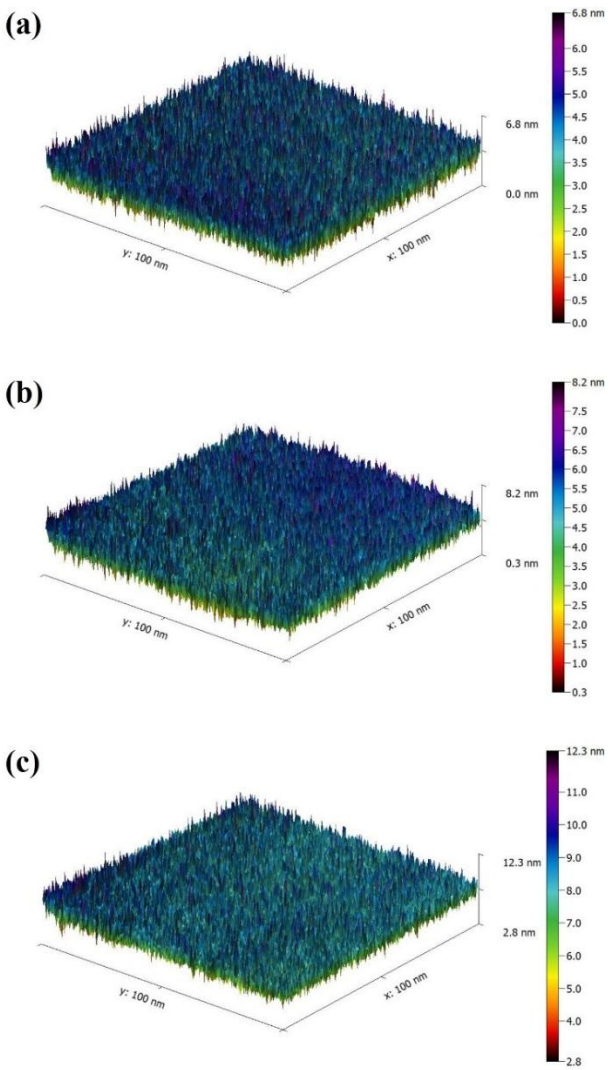

Fig. 2. Three-dimensional AFM topographic image of (**a**) clean Au film layer, (**b**) bound self-assembled monolayer (SAM) and (**c**) immobilized lysozyme.

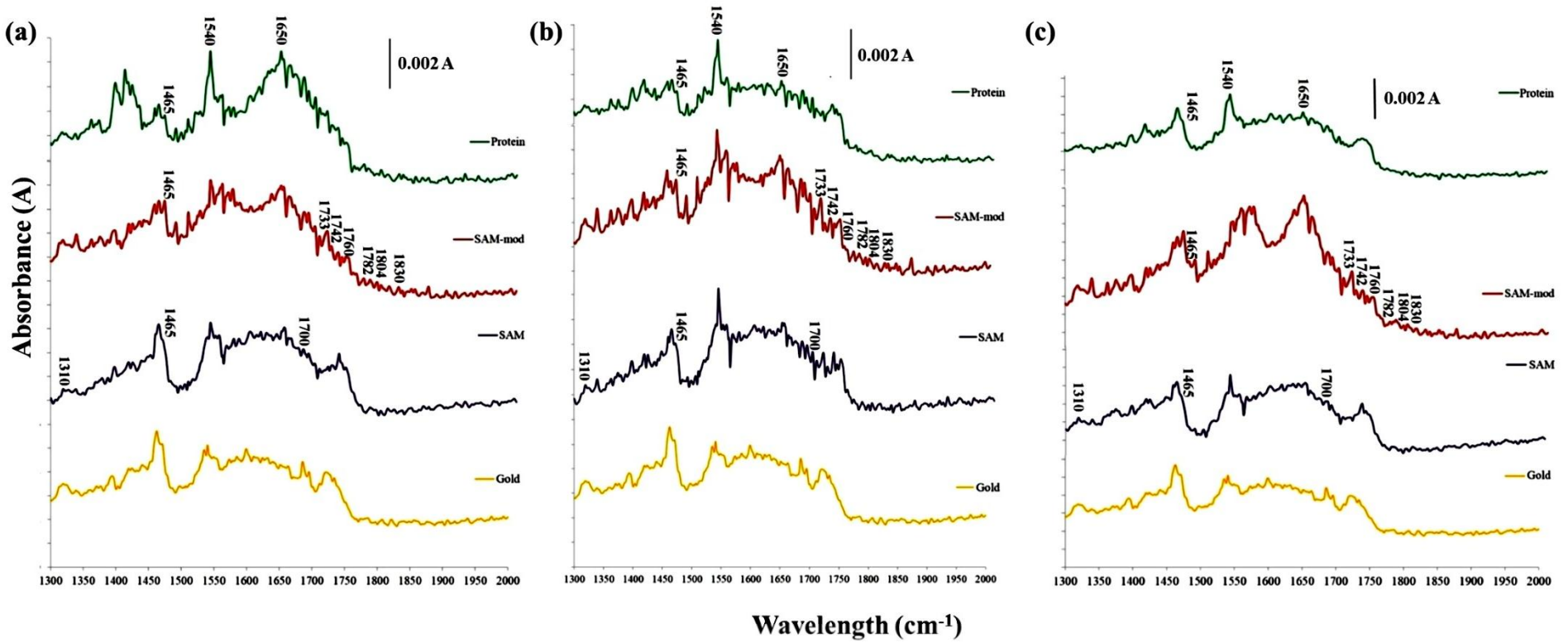

Fig. 3. FTIR spectrum of SAMs (**a**) 3-mercaptopropionic acid, (**b**) 3-mercaptopropionic acid/cysteamine, (**c**) 3-mercaptopropionic acid/1-propanethiol with their respective EDC/NHS esterification and lysozyme immobilization FTIR spectrums. A gold film layer spectrum is included as reference.

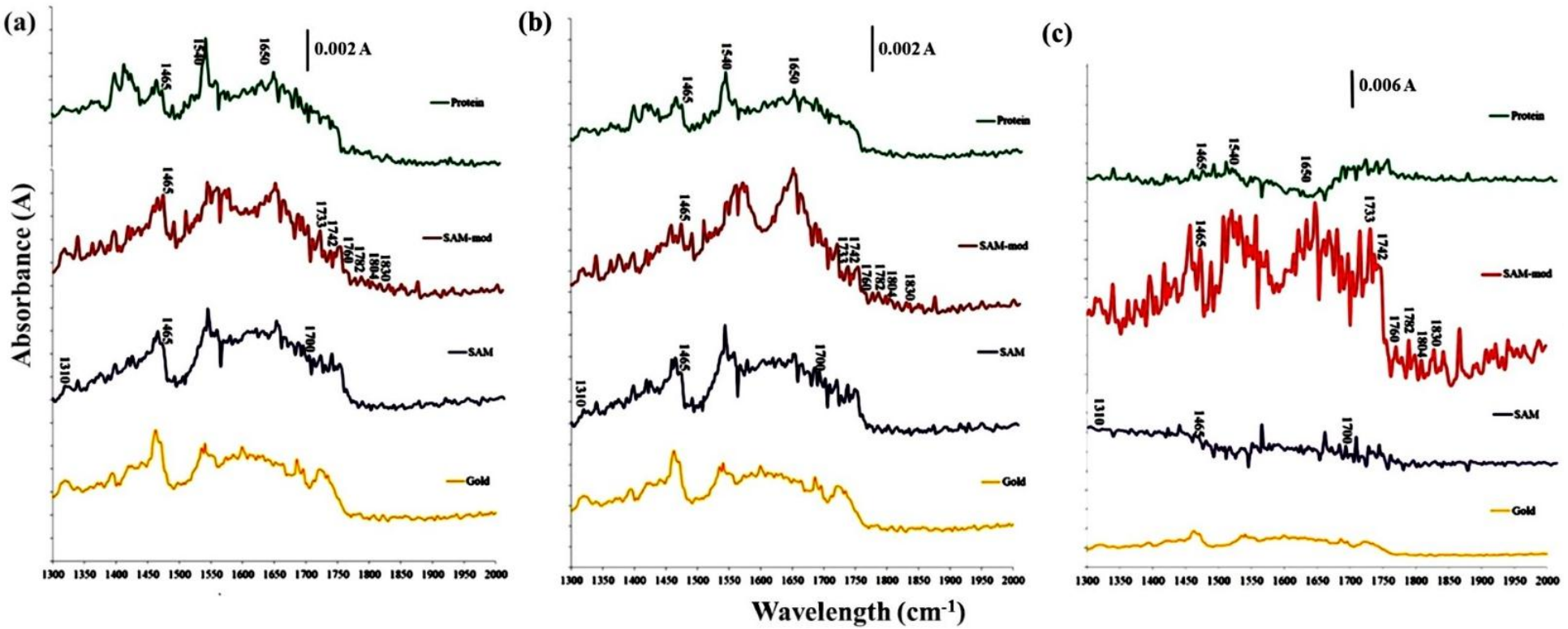

Fig. 4. FTIR spectra of (**a**) 11-mercaptoundecanoic acid, (**b**) 11-mercaptoundecanoic acid/1-nonanethiol, and (**c**) bis-(10-carboxydecyl) disulphide with their respective EDC/NHS esterification and lysozyme immobilization FTIR spectrums. A gold film layer FTIR spectrum is included as reference.

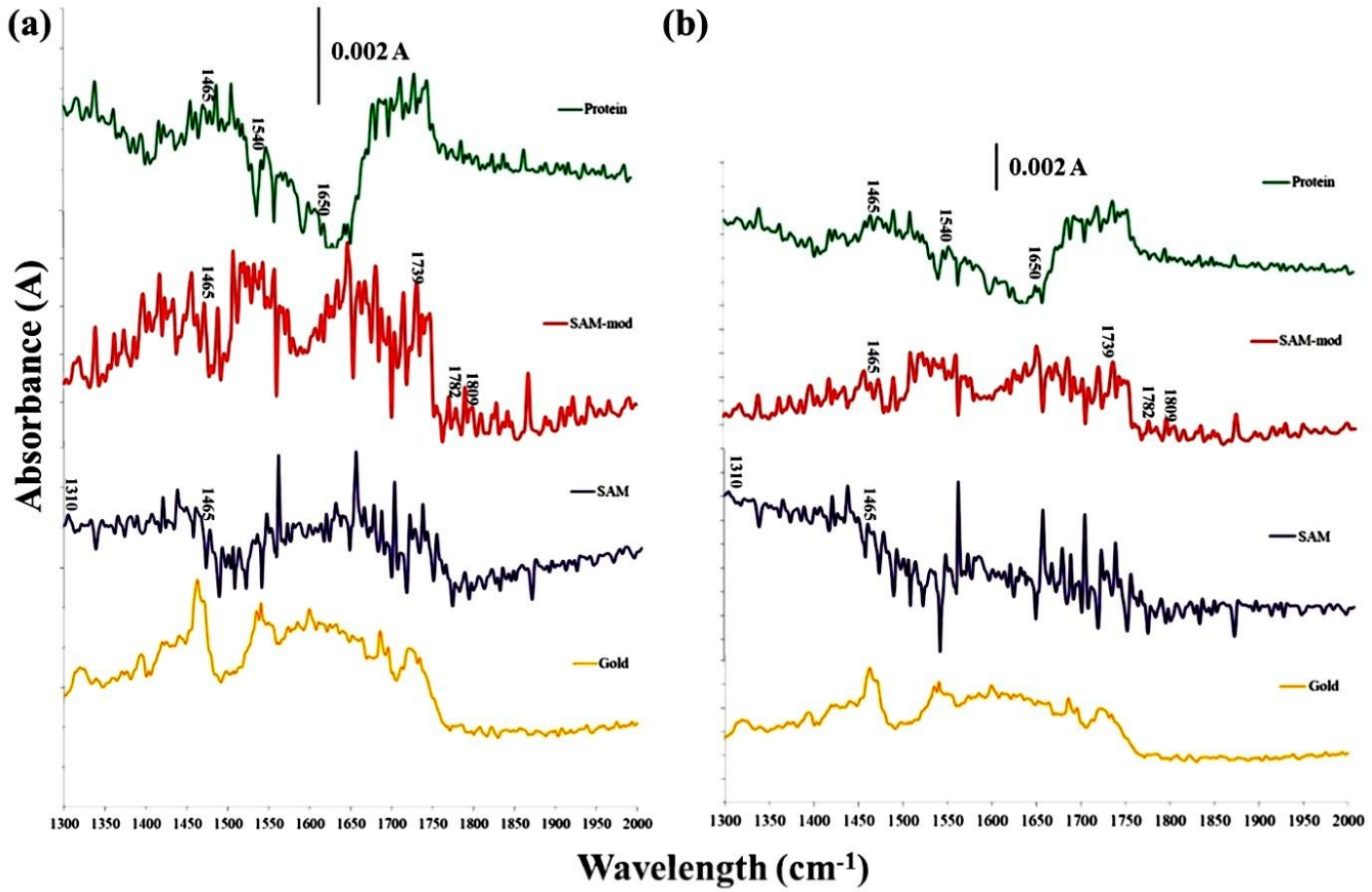

Fig. 5. FTIR spectrum of SAMs (**a**) 1-nonanethiol and (**b**) 1-propanethiol, with their respective FTIR spectrums for modification with DSP and lysozyme immobilization. A gold FTIR spectrum is included as reference.

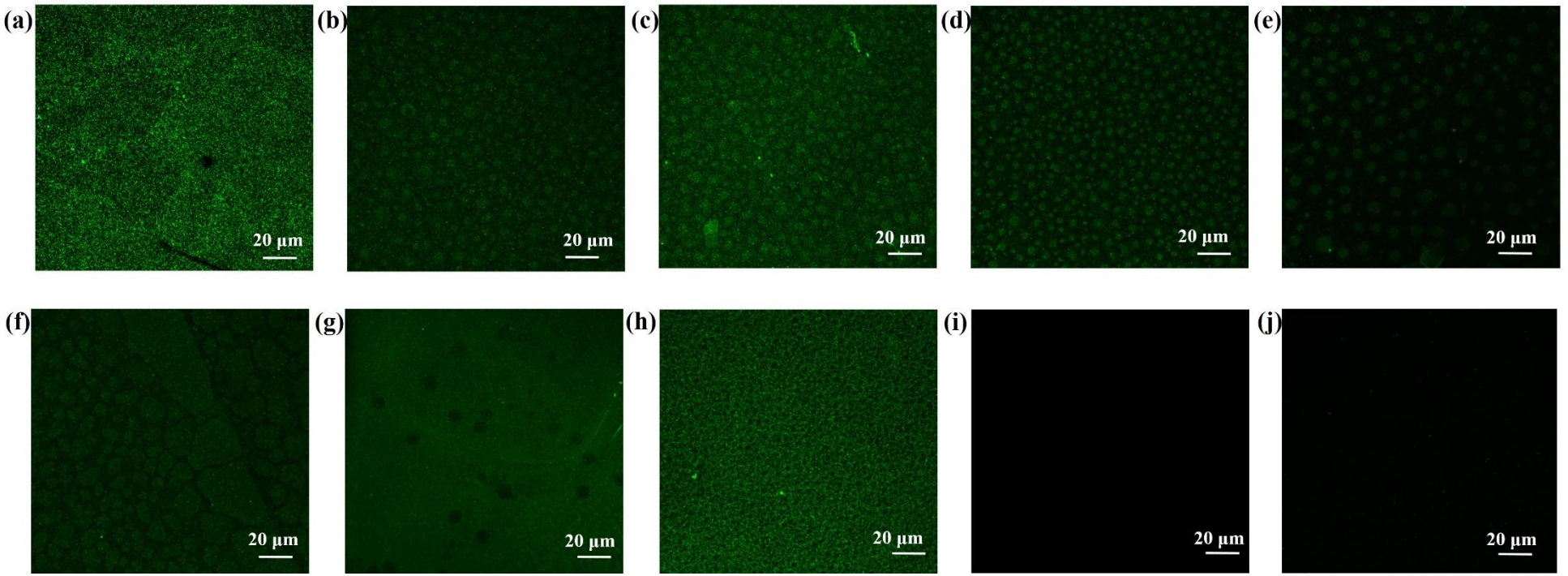

Fig. 6. Fluorescence microscopy images of lysozyme immobilized to SAMs (**a**) 3-mercaptopropionic acid, (**b**) 3-mercaptopropionic acid/cysteamine, (**c**) 3-mercaptopropionic acid/1-propanethiol, (**d**) 11-mercaptoundecanoic acid, (**e**) 11-mercaptoundecanoic acid/1-nonanethiol, (**f**) bis-(10-carboxydecyl) disulphide, (**g**) 1-nonanethiol and (**h**) 1-propanethiol. Non-specific binding of lysozyme to (**i**) Au film layers is shown. Non-specific binding of the lysozyme fluorescent antibody conjugate (**j**) to Au film layers is shown.

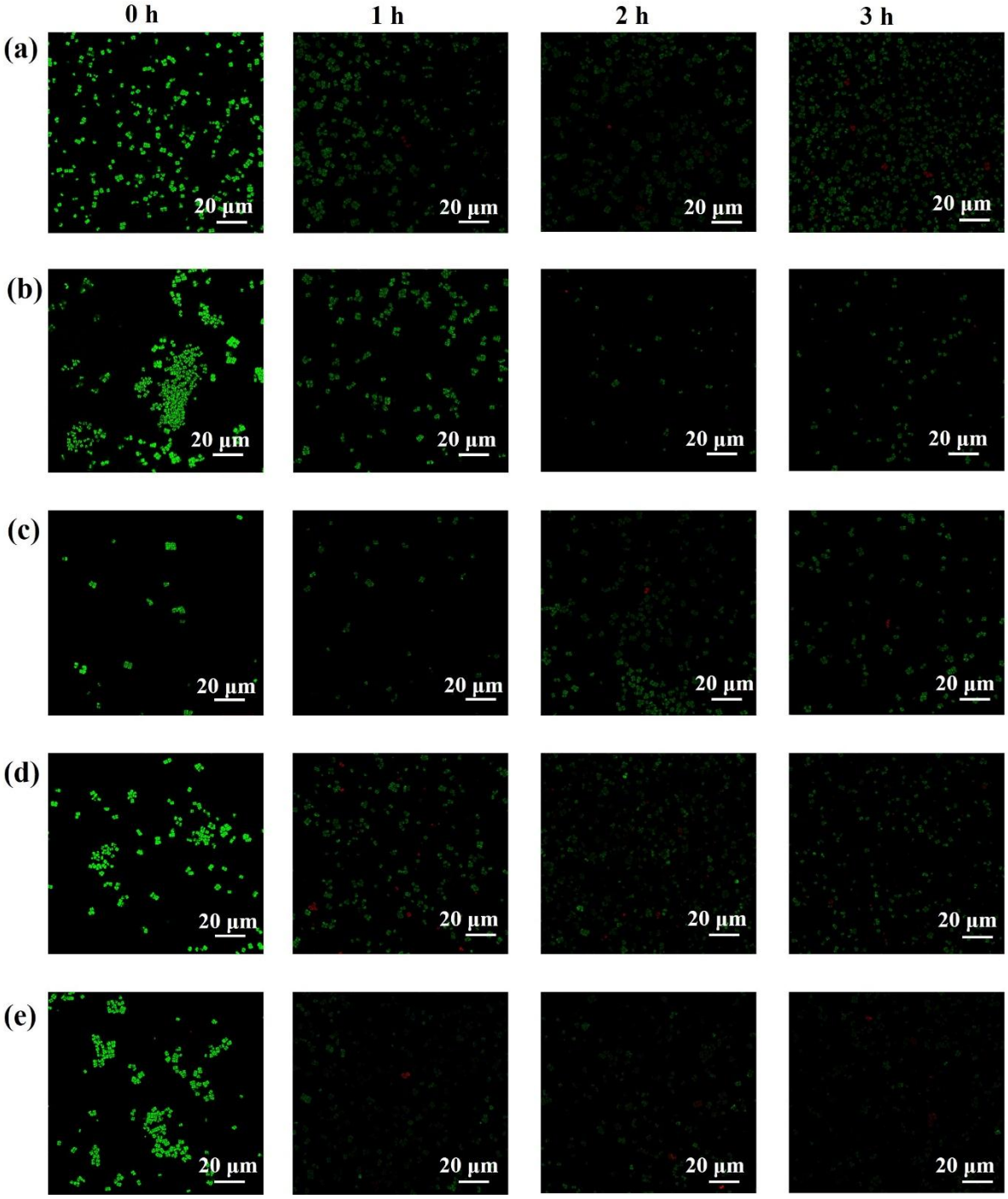

Fig. 7. Fluorescence microscopy images of *Micrococcus luteus* suspended for 1-3 hours on an Au film layer immobilized with lysozyme using SAMs (**a**) 3-mercaptopropionic acid, (**b**) 3-mercaptopropionic acid/cysteamine, (**c**) 3-mercaptopropionic acid/1-propanethiol, (**d**) 11-mercaptoundecanoic acid and (**e**) 11-mercaptoundecanoic acid/1-nonanethiol.

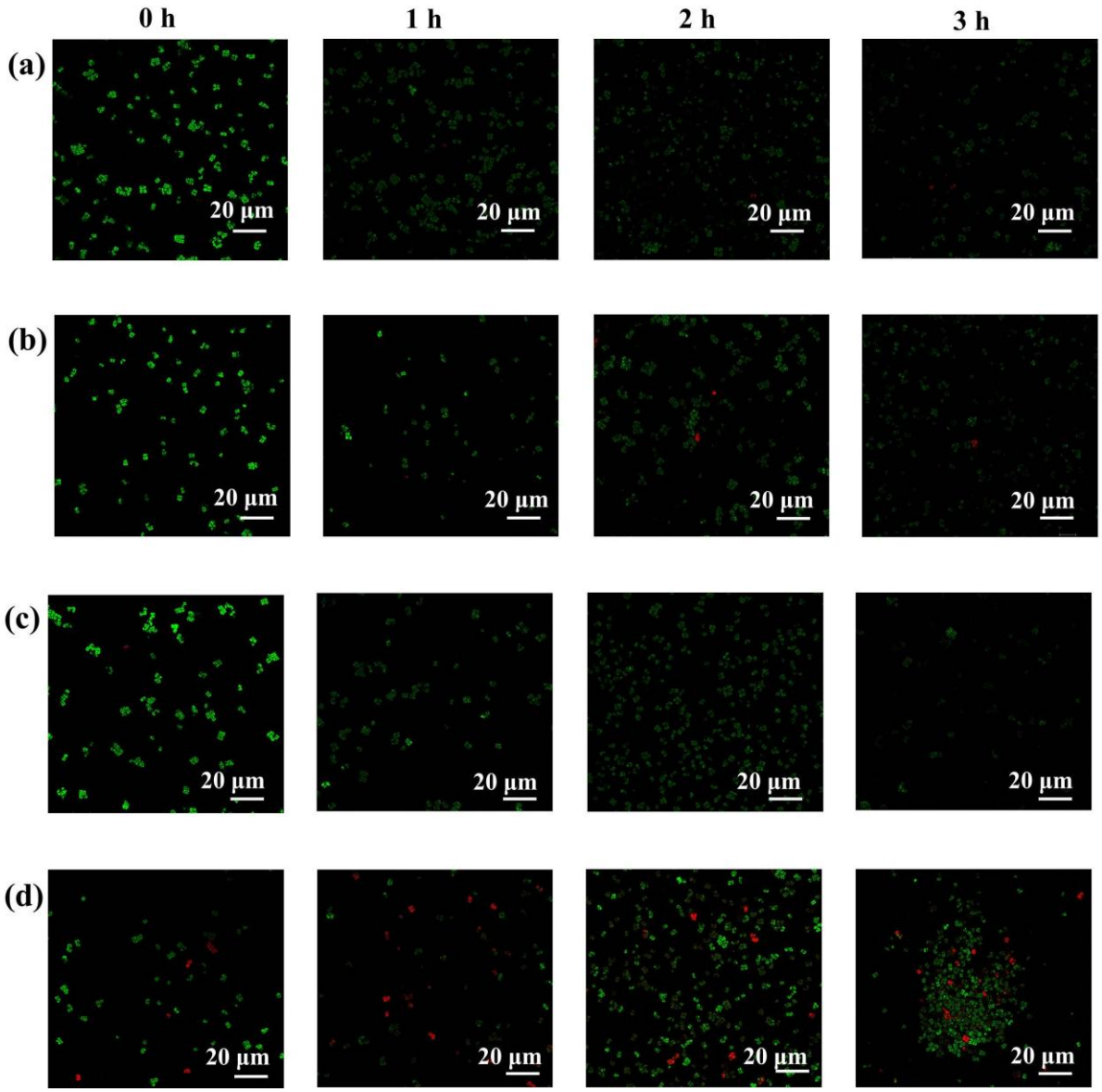

Fig. 8. Fluorescence microscopy images of *Micrococcus luteus* suspended for 1-3 hours on an Au film layer immobilized with lysozyme using SAMs (**a**) bis-(10-carboxydecyl) disulphide, (**b**) 1-nonanethiol and (**c**) 1-propanethiol. *M. luteus* cells suspended on a (**d**) clean Au film layer is included as negative control.

CHAPTER 5

A nanoforce ZnO nanowire-array biosensor for the detection and quantification of immunoglobulins

A nanoforce ZnO nanowire-array biosensor for the detection and quantification of immunoglobulins

[1] D.P. Neveling, [2] T.S. van den Heever, [2] W.J. Perold, [1] L.M.T. Dicks

[1] Department of Microbiology, University of Stellenbosch, Private Bag X1, Matieland 7602, Stellenbosch, South Africa

[2] Department of Electrical and Electronic Engineering, University of Stellenbosch, Private Bag X1, Matieland 7602, Stellenbosch, South Africa

Abstract

A nanoforce ZnO nanowire-array biosensor was developed to detect immunoglobulins. Hydrothermally synthesized ZnO nanowires and the constructed biosensor were characterized by atomic force microscopy (AFM), scanning electron microscopy (SEM), transmission electron microscopy (TEM) and X-ray diffraction (XRD). Lysozyme antigens and antibodies were used as a model to evaluate the sensitivity of the biosensor. Lysozyme was covalently immobilized onto the Au-coated/ZnO nanowire constructs by using self-assembled monolayers (SAMs) prepared with alkanethiol, 3-mercaptopropionic acid. Protein immobilization was characterized by AFM, Fourier transform infrared (FTIR) spectroscopy and fluorescence microscopy. *In vitro* tests were conducted with different concentrations of lysozyme antibodies. An increase in antibody concentration resulted in an increase in the piezoelectric signal and, subsequently, an increase in voltage. The piezoelectric potential is created due to disturbances induced in the nanowires, which in turn leads to the displacement of Zn^{2+} and O^{2-} in the crystal structure. This is the first report on the detection of antibodies using ZnO nanowires as piezoelectric transducers. Further research is in progress to optimize the biosensor.

Introduction

Detection of specific metabolites, nucleic acids, proteins and pathogens are essential in the diagnosis of diseases. Infectious diseases are responsible for approximately 40 % of the 50 million deaths recorded world-wide (Ivnitski et al., 1999). Waterborne pathogens cause 10-20 million of these deaths. Per annum more than 200 million people suffer from non-fatal infections (Ivnitski et al., 1999). Many of these cases could have been treated if the diagnosis had been made sooner. With the advances in nanotechnology, it should be possible to develop a rapid, sensitive and portable, but power-efficient and low cost biosensor.

The biosensor has to be sensitive enough to provide quantitative, or at least semi-quantitative, data. This means the device has to detect small changes in the concentration of molecules that react with a transducer (Strehlitz et al., 2008). Major developments have been made to increase the performance of biosensors by incorporating various nanostructured material (Ansari et al., 2008; Hrapovic et al., 2004; Lin et al., 2004, Rout et al., 2006; Wang et al., 2008; Zhang et al., 2008).

Nanostructures such as nanobelts (Gao et al., 2005; Pan et al., 2001), nanosprings (Kong and Wang, 2003), nanorings (Kong and Wang, 2003), nanohelixes (Gao et al., 2005) nanobows (Hughes and Wang, 2004), nanowires (Huang et al., 2001b), nanotubes (Sun et al., 2005), nanocages (Snure and Ashutosh, 2007), nanoshells (Leung et al., 2005), nanospheres (Zhang et al., 2009), nanofibers (Fang et al., 2006), nano-tetrapods (Newton and Warburton, 2007), nanonails and nanobridges (Lao et al., 2003) have been synthesized. The inherently larger surface area of the nanostructured material offers a higher enzyme loading capacity, which improves the sensitivity of the biosensor (Ramirez-Vick, 2012). The diameter of nanostructured material is usually comparable to the size of the biomolecule being sensed, which intuitively makes them excellent transducers for producing a signal. Biosensors offer several advantages over standard antibody detection methods (i.e. enzyme-linked immunosorbent assays, magnetic immunoassay, immunoprecipitation, radial immunodiffusion and Western blotting), such as, rapid detection, ease of use, low production cost, simplicity, portability, and ease of mass manufacturing (Strehlitz et al., 2008).

ZnO nanostructures are ideal transducers for biosensors in that they have polar surfaces and no centre symmetry (Wang, 2008). The interaction of polar surfaces makes the growth of diverse ZnO nanostructures possible (Wang et al., 2004). The lack of centre symmetry gives ZnO its piezoelectric properties (Wang, 2007 and 2008). At ambient temperature and

pressure, ZnO crystalizes in a wurtzite structure with a hexagonal lattice that has two interconnecting sub-lattices of Zn^{2+} and O^{2-} with the zinc ion surrounded by tetrahedral oxygen ions and *vice versa* (Coleman and Jagadish, 2006; Özgür et al., 2005). This tetrahedral coordination gives rise to a polar symmetry along the hexagonal axis, which is responsible for the piezoelectric and spontaneous polarization properties (Wang, 2004). Another important property of ZnO is that it is a semiconductor with high bandgap energy of 3.37 eV at room temperature (Zhao et al., 2007). ZnO nanostructured material are also biocompatible (Li et al., 2008), chemically stable, non-toxic, biomimetic and possess high electron communication features (Tian et al., 2002; Sberveglieri et al., 1995; Rodriquez et al., 2000) which makes them excellent candidates as transducers for biosensors.

ZnO nanostructures have enormous applications in electrochemical, electromechanical and optoelectronic devices, but also as photocatalysts. ZnO electrochemical devices that have been developed include field-effect transistors (FET), gas sensors, pH sensors and humidity sensors. In FETs, the ZnO nanostructures are laterally bonded on a substrate that serves as a gate electrode. Current transported from the drain to the source along the nanowire is controlled by applied gate voltage. ZnO nanowire field-effect transistors have been developed for sensing of oxygen (Fan et al., 2004), carbon monoxide gas (Khoang et al., 2013), riboflavin (Hagen et al., 2011) and streptavidin (Kim et al., 2006) amongst others.

Gas sensors have been developed for the detection of H_2 (Lupan et al., 2007), CO (Wang et al., 2007a), H_2S (Wang et al., 2006a), NH_3 (Wen et al., 2005), CH_4 (Gruber et al., 2003), NO_2 (Fan and Lu, 2005), NO (Farmakis et al., 2008), O_3 (Martins et al., 2004), and O_2 (Li et al., 2004) amongst others. pH sensors using ZnO nanostructures have also been developed. Exposure to electrolytic solutions results in the formation of a surface charge which alters the ZnO nanostructure conductive properties (Al-Hilli et al., 2007). ZnO nanostructures have also been proposed as humidity sensors. With the increase in the relative humidity, the resistance of some sensors decreased (Fang et al., 2009; Park et al., 2010; Zhang et al., 2005).

Electromechanical devices that have been developed include acoustic wave based sensors, nanogenerators, piezoelectric-FETs (PE-FET), and piezodiodes. Acoustic wave biosensors are mass sensors which operate with mechanical acoustic waves as their transduction signal (Rocha-Gaso et al., 2009). Interaction at the surface interface causes changes in the acoustic wave properties (i.e. wave propagation, velocity, amplitude, or

resonant frequency). Surface acoustic wave (SAW) pressure sensors (Talbi et al., 2006), film bulk acoustic resonators (FBAR) (Chen et al., 2009b) and lateral extensional mode (LEM) piezoelectric resonators (Pang et al., 2006) based on ZnO nanostructures have been used to detect changes in mass or pressure.

Nanogenerators have been developed by utilizing the piezoelectric effect of ZnO nanowires (Chang et al., 2010; Wang and Song, 2006; Wang et al., 2007b; Xu et al., 2010). The combination of the piezoelectric and semiconducting properties of ZnO, and the gating effect of a Schottky barrier, transforms the mechanical displacement to an electrical signal. Piezoelectric-FET (PE-FET) has been developed by coupling the semiconductive and piezoelectric properties of ZnO, which is defined as the piezotronic effect (Gao et al., 2009; Kwon et al., 2008; Wang et al., 2006b). The working principle of PE-FET relies on the piezoelectric potential of the nanowire under straining and serves as the gate voltage for controlling the current flow from the drain to source (Fei et al., 2009; Wang et al., 2006b).

Optoelectronic devices with ZnO nanostructures as transducers are UV detectors, UV lasers (Huang et al. 2001a), solar cells and field emission devices. UV detectors rely on changes in electric potential of the ZnO nanostructures when irradiated with UV (Bai et al., 2011; Chen et al., 2009a; Fang et al., 2009; Lu et al., 2009). ZnO nanostructure-based light emitting diodes (LEDs) have also been developed (Chen et al., 2011; Djurišić et al., 2010; Hsu et al., 2008; Sadaf et al., 2011; Willander et al., 2009; Yang et al., 2008). ZnO-based dye-sensitized solar cells (DSSCs) have been developed using ZnO nanostructures which transports electrons fasters, with less recombination loss (Law et al., 2005). ZnO nanostructures are also considered good candidates for field emitters due to their high melting point and high stability under oxygen environments (Hwang et al., 2011; Zhao et al., 2011).

ZnO nanostructures as photocatalysts have been reported (Kenanakis and Katsarakis, 2010; Ma et al., 2011; Sugunan et al., 2010), and exhibit high photocatalytic efficiency for dye degradation (Hariharan, 2006). Photocatalytic dye degradation by ZnO occurs due to the production of charge transferred photogenerated carriers and reactive oxygen species (ROS) due to UV illumination of the nanostructures (Guo et al., 2011).

In the present study, a nanoforce ZnO nanowire-array biosensor was developed for the detection of immunoglobulins. The antigen-antibody recognition event is sensed by immobilizing the antigen onto the Au-coated/ZnO nanowire constructs. Binding of antibodies to the constructs results in the bending of the ZnO nanowires, and subsequently, the

displacement of the Zn cations and O anions in the crystal resulting in the generation of piezoelectricity. The semiconductor-metal interface between the ZnO nanowires and Au electrode forms a Schottky barrier which rectifies the piezoelectric effect making it possible to measure the resulting output voltage across a resistor.

Lysozyme and anti-lysozyme was used as a model for the development of a prototype sensor capable of detecting biorecognition events. Hydrothermally synthesized ZnO nanowires and constructed biosensors were characterized by atomic force microscopy (AFM), scanning electron microscopy (SEM), transmission electron microscopy (TEM) and X-ray diffraction (XRD). The antigen was covalently immobilized onto the Au coated/ZnO nanowire constructs using self-assembled monolayers (SAMs). Immobilization of the antigen was characterized by atomic force microscopy (AFM), fourier transform infrared (FTIR) spectroscopy and fluorescence microscopy. *In vitro* studies were conducted to determine whether different levels of antibody binding results in different voltage production, due to the bending of the ZnO nanowires and subsequent piezoelectricity production.

Materials and Methods

Biosensor construction

Substrate preparation

Silicon (100) wafers were cut into 1 x 1 cm sizes and sonicated for 10 min in acetone, followed by 10 min in absolute ethanol and 10 min in distilled H_2O. The wafers were dried under nitrogen gas and placed on a hot plate at 110 °C for 5 min. A 20 nm titanium (Ti) film layer was deposited by RF cylindrical magnetron sputtering at 2 x 10^{-2} mbar pressure in the presence of 60 % argon at 50 V, - 400 V, 0.5 A, 100 W, 21 kHz and 100 W.

The coated wafers were cleaned by immersion in absolute ethanol for 10 sec, dried under nitrogen gas, placed on a hot plate at 110 °C for 5 min and then coated with a 40 nm layer of Au. Coating was done using a Quorum sputter coater (Quorum Technologies Ltd, West Sussex, UK), set at 1.5 kV and 20 mA and operated under 2 x 10^{-1} mbar pressure in the presence of argon. The Au coated substrates were then cleaned by immersion in gold cleaning solution (Sigma Aldrich, Missouri, USA) for 30 sec, rinsed with distilled H_2O for 30 sec and dried under N_2 gas. ZnO seed layers were deposited by using the sol-gel spin

coating technique. In short, this involved the following: zinc acetate dehydrate (0.75 M) was dissolved in a mixture of 2-methoxyethanol and monoethanolamine at 25 °C, the molar ratio of monoethanolamine to zinc acetate was 1:1. The solution was stirred for 1 h at 60 °C, after which 25 µl was placed onto the gold-plated Si wafers and spun in a Laurell WS-400-6NPP spin coater (Laurell Technologies, Pennsylvania, USA) at 6000 rpm for 30 sec. After spin-coating, the wafers were dried at 200 °C for 5 min on a hot plate to evaporate the solvents and remove the residual organic components from the film layer. The ZnO seed layers were then annealed in air at 700 °C for 10 min.

Synthesis of ZnO nanowires

Zinc oxide nanowires were synthesized using the hydrothermal growth method. Wafers coated with a ZnO seed layer were placed facing down on a solution of 0.01 M zinc nitrate hexahydrate [$Zn(NO_3)_2 \cdot 6H_2O$] and 0.01 M hexamethylenetetramine [$C_6H_{12}N_4$] in distilled H_2O for 7 h in an oven at 90 °C. The coated wafers were then washed with distilled water to remove the residual salts and amino complexes, dried under nitrogen gas and placed on a hotplate at 110 °C for 5 min. The ZnO-coated wafers were then baked at 350 °C for 30 min.

Schottky barrier formation

The ZnO-coated wafers were spun coated with 50 µl of poly(1-vinylpyrrolidone-co-2-dimethylaminoethyl methacrylate) (PMMA; 3.04 % w/w), using a Laurell WS-400-6NPP spin coater at 7000 rpm for 30 sec. The PMMA layer acts as a barrier to prevent contact between the two Au film layers. Contact which each other would result in an electrical shortage of the diode. The wafers were dried at 120 °C for 5 min and then coated with a 10 nm layer of Au at 70°, using a Quorum sputter coater at 1.5 kV and 20 mA, operated under 2 x 10^{-1} mbar pressure in the presence of argon. A metal-semiconductor junction formed between the Au film layer and the ZnO nanowires, creating a Schottky barrier. The Au side of the biosensor acts as the anode and the ZnO semiconductor acts as the cathode (Fig. 1).

Protein immobilization

Glass containers were cleaned with piranha solution [30:70 v/v H_2O_2 and H_2SO_4] to avoid contamination and rinsed 3 times with absolute ethanol. Alkanethiol, 3-mercaptopropionic acid (1 mM) was dissolved in absolute ethanol (pH 2.0) by sonication for 5 min at 25 °C. The Au coated/ZnO nanowire substrates were immersed in the SAM solution for 24 h at 25 °C under N_2 atmosphere (99.9 %). Oxygen-free environments were created using a Schlenk reaction vessel. A vacuum was created within the vessel and the vessel filled with inert N_2 gas. Upon completion of SAM formation, the reaction was terminated by rinsing the substrates three times with absolute ethanol.

The sensor surface bound with SAMs were incubated in the presence of chemical linkers to form SAM-intermediates reactive towards primary amino groups of proteins. The SAMs were reacted with 5 mM EDC (> 99 %) [ethyl (dimethylaminopropyl) carbodiimide] and 5 mM (≥ 97 %) NHS (N-hydroxysuccinimide) in absolute ethanol (pH 7.0), under N_2 atmosphere at 25 °C for 3 h. EDC is used in combination with NHS to increase the coupling efficacy or to create a more stable reactive intermediate.

After SAM-intermediate formation, the sensors were rinsed with PBS solution (137 mM NaCl, 2.7 mM KCl, 10 mM $Na_2HPO_4 \cdot 2H_2O$, 2 mM KH_2PO_4, pH 7.2) for 10 sec. The sensors were then placed in PBS solution containing lysozyme (1 mg/ml) from hen egg white (Roche, Mannheim, Germany), under N_2 atmosphere at 4 °C for 24 h. Upon completion of protein immobilization, the functionalized biosensors were rinsed with PBS solution for 10 sec, dried with N_2 gas and stored at 4 °C under N_2 atmosphere. A schematic representation of the lysozyme functionalized nanoforce ZnO nanowire-array biosensor is shown in Fig. 1.

Biosensor characterization

Characterization of ZnO nanowires

A Nanosurf AFM Easyscan 2 (Nanosurf Inc., California, USA) was used to characterize the surface topology of the deposited ZnO seed layers and to determine the surface roughness. The surface morphology, diameter and density of the synthesized ZnO nanowires were evaluated using a FEI Nova NanoSEM 230, equipped with a TLD detector (FEI, Oregon,

USA). The purity and elemental composition of the ZnO nanowires were analysed using a FEI Nova NanoSEM 230, equipped with an X/Max Oxford energy-dispersive x-ray (EDX) detector (Oxford Instruments, Oxfordshire, UK) with a detector area of 20 mm^2. EDX spectrums were analysed using INCA software (Inca Software, Berkshire, UK).

Transmission electron microscopy micrographs and selected area electron diffraction (SAED) patterns were collected with a Philips Tecnai TF20 TEM (FEI, Oregon, USA), equipped with a field emission gun and operated at an accelerating voltage of 200 kV. High resolution transmission electron microscopy (HRTEM) images were also obtained to analyse the crystal structure of the ZnO nanowires and to determine the axial growth direction. The mean length and diameter of the synthesized ZnO nanowires were also assessed using TEM micrographs. For TEM analysis, ZnO nanowires were scratched off the substrate surface, dissolved in absolute ethanol and ultrasonicated for 10 sec. A drop of the liquid was placed on a Cu grid of which the back was covered with a carbon film layer. The samples were allowed to air dry prior to analysis.

The Au film layer and the ZnO nanowire crystal structures and phase compositions were determined by XRD using a Bruker AXS D8 Advance X-ray diffractometer operated in locked coupled mode (Bruker AXS, Frankfurt, Germany). The instrument was equipped with a Vantec-1 position sensitive detector optimized for Cu-Kα radiation with λ= 1.5406 Å. The X-ray tube was operated at 40 mA and 40 kV and the measurements were recorded at a scanning rate of 0.5 sec/step with a step size of 0.014° in a 2θ range extending from 31.28° to 149.3°.

Characterization of protein immobilization

Atomic force microscopy (AFM) images were collected with a Nanosurf AFM Easyscan 2 (Nanosurf Inc., California, USA) to assess the surface topology of the immobilized lysozyme and to determine the surface roughness of the deposited Au film layers. Images were acquired in tapping mode at a scan rate of 2Hz with a Pt cantilever (spring constant of 0.06 N m^{-1}) with drive amplitude between 20-50 mV and set-points in the range of 0.14 V.

Infrared (IR) spectra of the monolayers were obtained to confirm SAM formation, follow the chemical modification of the SAM functional groups and the immobilization of lysozyme. Attenuated Total Reflectance-Fourier-transform infrared (ATR-FTIR) spectra

were recorded in the range of 500-4000 cm^{-1} by a Thermo Scientific Nicolet iS10 FTIR (Thermo Scientific Inc., Massachusetts, USA) spectrometer. Attenuated Total Reflectance-Fourier-transform infrared spectra were collected using 300 scans with a 4 cm^{-1} resolution. FTIR spectra were background subtracted and corrected for atmospheric suppression using the OMNIC software (Thermo Scientific Inc., Massachusetts, USA).

Surface coverage of the immobilized lysozyme was studied using fluorescence microscopy. Lysozyme functionalized biosensors were incubated with 100 µg/ml rabbit primary lysozyme antibody serum (Rockland Immunochemicals Inc., Pennsylvania, USA) in casein-PBS solution (1 % casein in PBS solution, pH 7.2) for 30 min at 25 °C and thereafter washed for 5 min in casein-PBS solution. The biosensor bound with primary antibodies were then incubated with 10 µg/ml Alexa Fluor 488 goat anti rabbit H+L IgG (Life Technologies, California, USA) in casein-PBS solution for 30 min at 25 °C in the dark and thereafter washed for 5 min in casein-PBS solution in the dark. Confocal images were acquired with a Carl Zeiss Confocal LSM 780 Elyra S1 scanning laser microscope equipped with a SR-SIM super resolution platform (Carl Zeiss, Oberkochen, Germany) using a 100 X oil-immersion lens. An argon/krypton laser excited the Alexa Fluor 488 at 488 nm and emitted light detected at 493-630 nm.

In vitro testing of the biosensor

The lysozyme functionalized biosensors were fixed to a test-board as shown in Fig. 2. The biosensor is placed in the centre and the four corners are connected to one of the conducting lines, using silver paste. Conducting wires are also added to the lines to be connected to the measuring equipment. The area of the biosensor containing only Au (anode) is connected to ground and the area with the nanowires (diode) connected to the positive terminal of the measurement equipment. Binding of antibodies to the functionalized Au coated/ZnO nanowire constructs results in bending of the nanowires, which in turn creates a piezoelectric potential and a voltage reading.

Voltage readings were taken using an amplifier with a gain of 100 V/V. Binding of the antibodies to the lysozyme-coated nanowires generated low electronic voltages. The amplified signal in analog format was converted to a digital signal using a LabJack U6

converter (LabJack Corporation, Colorado, USA). The digital signal was analysed using DAQFactory software (Azeotech Inc., Oregon, USA).

Lysozyme functionalized biosensors were exposed to monospecific lysozyme antiserum at a concentration of 10 ng/ml, 50 ng/ml, 500 ng/ml, 1 µg/ml, 10 µg/ml and 20 µg/ml (Rockland Immunochemicals Inc., Pennsylvania, USA). Antibodies were suspended in PBS solution, placed on the biosensor surface, incubated for 1 h at 25 °C, washed with PBS solution for 30 sec, dried with N_2 gas and analyzed.

Results and Discussion

Two-dimensional and three-dimensional AFM surface topology images of deposited ZnO seed layers are shown in Fig. 3. According to two-dimensional surface topology (Fig. 3 a), the mean grain diameter of the deposited ZnO seed layer was 89 nm (σ= 22), with a root-mean-square surface roughness of 2 nm. The three-dimensional topology images revealed that the average length of the ZnO grains ranged between 8 and 9 nm (Fig. 3 b). The mean diameter of the synthesized ZnO nanowires was calculated from the relative diameter abundance of 1000 ZnO nanowires. The nanowires had an average diameter of 78 nm (σ= 35), with a density of 108 per μm^2 (Fig. 4 a). The hexagonal structure of ZnO nanowires was visible by SEM image (Fig. 4 a). The ZnO nanowires were uniformly distributed; mainly c-axis oriented (Fig. 4 b) and retained their hexagonal structure after PMMA and Au deposition (Fig. 4 c). Filling of the spaces between the ZnO nanowires with PMMA is clearly visible in Fig. 4 d. The average length of the parturition of the nanowires from the PMMA layer was 180 nm (σ= 45).

The elemental composition of individual ZnO nanowires was determined by EDS analysis, which indicated that the Zn (51 %) and O (49 %) were nearly stoichiometric with a ratio a ratio of 1:1. TEM micrographs indicated that hexagonal ZnO nanowires were synthesized with an average diameter of 93 nm (Fig. 5 a) and an average length of 2.3 µm (Fig. 5 d). The HRTEM image of the synthesized ZnO nanowires (Fig. 5 b) revealed the major lattice spacing of 0.28 nm which corresponds with the distance of the (002) crystal plane of wurtzite ZnO. The HRTEM image also confirmed the perfection of the atomic arrangements within the ZnO nanowires. The ZnO nanowires had a single-crystal hexagonal wurtzite structure (Fig. 5 c). By indexing the diffraction pattern the main axis of the ZnO

nanowires equivalent to the growth direction can be determined. According to the indexed SEAD pattern, the ZnO nanowires grew along the [0001] direction. Based on TEM analysis, the average length of ZnO nanowire protrude from the PMMA layer was 216 nm (Fig. 5 e). Coating of the ZnO nanowire parturitions with Au is also clearly visible.

XRD analyses of synthesized ZnO nanowires were used to assess whether the ZnO nanowires were c-axis oriented by looking at the relative abundance of the ZnO diffraction peaks (Table 1). Since the surface of the sample lies in the scattering plane of the instrument, a set of perfectly aligned nanowires, orientated perpendicular to the surface, would result in a single diffraction peak, the 002 peak. Hence, the relative distribution of the ZnO diffraction peaks will indicate whether the ZnO nanowires are oriented along the [0001] direction. The ZnO diffraction peaks that did not overlap with the Au film layer and Si substrate peaks are listed in Table 1. The XRD pattern of the ZnO nanowires was indexed using the JCPDS database and corresponded to hexagonal ZnO. XRD analysis indicated that the major crystal growth plane was (002) with low abundance of other crystal planes such as (100), (101), (102), (103), (004), (202), (104), (203), (105) and (006) indicating high orientation in the c-axis.

Atomic force microscopy was used to assess the constructed biosensor surface and the immobilization of lysozyme to the surface. Figure 6 shows the three-dimensional topographic images of the constructed biosensor (Fig. 6 a); a smooth area of the biosensor (Fig. 6 b) and a smooth area of the biosensor immobilized with lysozyme (Fig. 6 c). From these results it is clear that the ZnO nanowires protruded from the PMMA layer and that some were totally covered. A smooth surface was used to determine whether protein immobilization occurred as protruding nanowires would overshadow their signal. From Fig. 6 it is evident that protein immobilization occurred as an increase in the root mean square surface roughness was observed from 0.65 nm to 0.90 nm for unlabelled and labelled smooth biosensor surfaces, respectively.

Attenuated Total Reflectance-Fourier-transform infrared spectroscopy studies were conducted on separate substrates to confirm changes in the surface chemistry that occurred after each modification step. The FTIR spectra shown in Fig. 7 were used to verify monolayer formation, the activation of the SAM with EDC/NHS as well as the immobilization of lysozyme. SAM formation was confirmed by the presence of peaks characteristic to carboxylic acid groups. The spectrum exhibited a strong peak at 1700 cm^{-1}

which corresponds to the υ(C=O) free carboxylic acid stretch of carbonyls. Carbonyl stretching frequencies in this range are characteristic of dimerization or other intermolecular hydrogen bonding processes available to the carbonyl terminated SAM (Nuzzo et al., 1990). Additional peaks at 1310 and 1465 cm^{-1} were observed which belong to alkane groups. The peak at 1310 cm^{-1} is assigned to the C-H scissors vibration mode for alkanes and 1465 cm^{-1} assigned to methylene CH bending of methylene chains. The presence of these characteristic peaks indicated that carboxylic acid terminated SAM 3-mercaptopropionic acid formed on the Au surface.

The EDC/NHS esterification spectra displayed a different FTIR profile. A strong peak at 1742 cm^{-1} was present which corresponded to the υ(C=O) asymmetric carbonyl stretch of NHS esters that are contributed by the succinimidyl carbonyl group. Two weak peaks formed at 1830 cm^{-1} (NHS-ester carbonyl stretch) and 1782 cm^{-1} (NHS-ester C=O symmetric stretch). These peaks are attributed to the band splitting of the ester carbonyl C=O stretching vibration. Additional bands appeared at 1733 cm^{-1} (ester C=O stretch of N-acylurea), 1760 cm^{-1} (anhydride antisymmetric C=O stretch) and 1804 cm^{-1} (anhydride symmetric C=O stretch) which are by-products of the EDC/NHS esterification chemistry. The presence of these characteristic peaks indicated that EDC/NHS esterification of the carboxylic acid groups occurred. The addition of lysozyme to the chemically activated surface resulted in the presence of characteristic bands at 1540 and 1650 cm^{-1}. The peak at 1650 cm^{-1} can be assigned to amide I (C=O stretch) and 1540 cm^{-1} to amide II (NH bend and CN stretch combined) modes. The presence of these two peaks indicated that lysozyme was covalently immobilized to the SAM and thus subsequently to the Au surface.

Fluorescence microscopy was used to assess the surface loading of lysozyme to the biosensor surface (Fig. 8). The lysozyme functional biosensor was incubated with primary lysozyme antibodies and secondary lysozyme fluorescent antibody conjugates. Lysozyme was immobilized to the biosensor surface. Non-specific binding of the secondary antibody conjugate and lysozyme to the surface was also assessed. The relative fluorescence intensity of the immobilized lysozyme biosensor surface was 287 RFU (Fig. 8 a), non-specific binding of the secondary antibody conjugates was 8 RFU (Fig. 8 b), and non-specific binding of lysozyme was 10 RFU (Fig. 8 c). Based on these results, lysozyme was immobilized to the SAMs, as the fluorescence intensity was not contributed by non-specific binding of the secondary antibody conjugate or lysozyme to the Au surface.

In vitro tests were conducted using monospecific antibody serum specific for lysozyme. Different concentrations were placed on the biosensor surface and incubated for 1 h to allow biorecognition. Voltage measured for biosensors prior to analysis and after incubation with different antibody concentrations is shown in Figs 9 and 10. The background voltage produced by the biosensor was measured to determine the voltage increase due to the binding of the antibodies to the nanowire constructs. The background signal arises from disoriented nanowires or pressure applied by the immobilized antigen. Prior to the addition of 10 ng/ml antibodies (Fig. 9 a) the biosensor produced an average voltage of 0.233 V. This increased to 0.497 V after the addition of antibodies. The average voltage produced from 50 ng/ml antibodies prior to addition was 0.928 V (Fig. 9 b), and increased to 1.347 V after the addition of antibodies. The biosensor incubated with 500 ng/ml (Fig. 9 c) antibodies produced an average voltage of 1.493 V prior to addition and an average voltage of 2.063 V after the addition. Prior to the addition of 1 µg/ml (Fig. 9 d) antibodies the biosensor produced an average voltage of 1.551 V and after the addition produced an average voltage of 2.321 V. For 10 µg/ml (Fig. 10 a) antibodies the biosensor produced an average voltage of 1.484 V prior to addition and an average voltage of 2.312 V after the addition of antibodies. For 20 µg/ml (Fig. 10 b) antibodies the biosensor produced an average voltage of 1.838 V prior to addition and an average voltage of 2.882 V after addition. For the negative control (Fig. 10 c) in which only PBS-solution was added, the biosensor produced an average voltage of 0.713 V prior to analysis and an average voltage of 0.517 V after the addition. These results indicate that increasing the antibody concentration results in the increase in voltage generation, which is attributed to the increased binding of the antibodies to the ZnO nanowire constructs. The increased binding will induce more disturbances in the ZnO nanowire structure which would result in the increase in the piezoelectric potential, and subsequently the increase in voltage generation. A field effect transistor (FET) developed by Kim et al. (2006) for the detection of streptavidin could detect concentrations ranging from 25 nM to 2.5 µM (Kim et al., 2006). Another ZnO nanowire FET developed by Choi et al. (2010) for streptavidin detection could detect concentrations ranging from 2.5 nM to 250 nM (Choi et al., 2010). A piezoelectric-FET (PE-FET) recently developed by Yu et al. (2013) to detect immunoglobulin G, could sense concentrations ranging from 0.1 ng/ml to 10 µg/ml (Yu et al., 2013). Thus the designed nanoforce ZnO nanowire-array biosensor was able to detect concentration ranges as other previously designed ZnO nanowire biosensors.

The *in vitro* tests concluded that ZnO nanowires are promising piezoelectric transducers for the use in biosensors for the detection of biomolecular recognition events. This is the first report on the detection of antibodies using ZnO nanowires as piezoelectric transducers. Numerous types of ZnO nanowire biosensors have been developed for the detection of biomolecules, however, none have used nanowires soley as piezoelectric transducers to detect biorecognition events (Kumar and Chen, 2008; Liu, 2008; Ozgur et al., 2010).

Further research is in progress to optimize the biosensor. The site-specific growth and controlled dimensions of ZnO nanowire growth requires optimization. Crystallization of ZnO is a thermodynamic process and can only be controlled to a certain degree. The dimensions of the ZnO nanowires can be controlled by a ZnO seed layer. However, seed layer deposition techniques can only control the ZnO grain size to a certain degree, and thus the dimensions of the synthesized ZnO nanowires. Techniques for the deposition of more controlled ZnO seed layer grains should be sought to control the ZnO nanowire dimensions more accurately. Additionally the site specific growth of ZnO nanowires should be sought as uncontrolled growth would result in different nanowire densities which would influence the performance of the developed biosensor. It should also be noted that the spin coating of PMMA into the ZnO nanowires is not efficient as some areas of the biosensor are fully covered with PMMA. Such surface defects would greatly influence the biosensor performance, as different amounts of protruding ZnO nanowires would influence the output voltage capacity of the biosensor. In the near future if these problems can be resolved ZnO nanowires would be great candidates as transducers for biosensors for the detection of biomolecular recognition events.

Conclusions

A nanoforce ZnO nanowire-array biosensor was fabricated for the detection of immunoglobulins. Highly c-axis oriented ZnO nanowire-arrays were synthesized by the hydrothermal growth method. The constructed biosensor was successfully constructed as shown by AFM, SEM, TEM, XRD, FTIR, and fluorescence microscopy analysis. The performance of the biosensor was tested by incubating different antibody concentrations on the sensor surface for 1 hour. Results show that increasing the antibody concentration results in the increase in the voltage generated by the biosensors. This is due to the increased binding of the antibodies to ZnO nanowire constructs which results in the increase in piezoelectric potential and subsequently the increase in voltage generated. Binding of antibodies to the

ZnO nanowire constructs causes bending of the nanowires or tensile stress, which displaces Zn^{2+} and O^{2-} and generates piezoelectricty. However, crystallization of ZnO nanowires can only be controlled to a certain degree. Thus differences in site-specific growth, densities and average diameters of the synthesized ZnO nanowires occur. Additionally spin coating of PMMA results in areas fully covered with no ZnO nanowire protrusions. These variations would greatly influence the performance and reproducibility of the developed biosensor. ZnO nanowires are promising piezoelectric transducers for biosensors for the detection of biomolecular recognition events. These transducers could be used to detect disease-causing agents much more rapidly and may be of specific benefit to third-world countries. However, numerous hurdle needs to be overcome in order for ZnO nanowires to become successful transducers in biosensors.

References

Al-Hilli, S.M., Willander, M., Öst, A., Stralfors, P., 2007. ZnO nanorods as an intracellular sensor for pH measurements. J. Appl. Phys. 102, 084304.

Ansari, A.A., Solanki, P.R., Malhotra, D.B., 2008. Sol-gel derived nanostructured cerium oxide film for glucose sensor. Appl. Phys. Lett. 92, 263901-263903.

Bai, S., Wu, W., Qin, Y., Cui, N., Bayerl, D.J., Wang, X., 2011. High-performance integrated ZnO nanowire UV sensors on rigid and flexible substrates. Adv. Funct. Mater. 21, 4464-4469.

Chang, C., Tran, V.H., Wang, J., Fuh, Y., Lin, L., 2010. Direct-write piezoelectric polymeric nanogenerators with high energy conversion efficiency. Nano Lett. 10, 726-731.

Chen, K.J., Hung, F.Y., Chang, S.J., Young, S.J., 2009a. Optoelectronic characteristics of UV photodetector based on ZnO nanowire thin films. J. Alloys Compd. 479, 674-677.

Chen, X., Ng, A.M.C., Fang, F., Ng, Y.H., Djurišić, A.B., Tam, H.L., Cheah, K.W., Gwo, S., Chan, W.K., Fong, P.W.K., Lui, H.F., Surya, C., 2011. ZnO nanorod/GaN light-emitting diodes: The origin of yellow and violet emission bands under reverse and forward bias. J. Appl. Phys. 110, 094513.

Chen, Y., Reyes, P.I., Duan, Z., Saraf, G., Wittstruck, R., Lu, Y., Taratula, O, Galoppini, E., 2009b. Multifunctional ZnO-based thin-film bulk acoustic resonator for biosensors. J. Electron. Mater. 38, 1605-1611.

Choi, A., Kim, K., Jung, H., Lee, S.Y., 2010. ZnO nanowire biosensors for detection of biomolecular interactions in enhancement mode. Sensor. Actuat. B: Chem. 148, 577-582.

Coleman, V.A., Jagadish, C., 2006. Zinc Oxide Bulk, Thin Films and Nanostructures, Elsevier, Amsterdam.

Djurišić, A.B., Ng, A.M.C., Chen, X.Y., 2010. ZnO nanostructures for optoelectronics: Material properties and device applications. Prog. Quantum Electron. 34, 191-259.

Fan, Z., Lu, J.G., 2005. Gate-refreshable nanowire chemical sensors. Appl. Phys. Lett. 86, 123510-123512.

Fan, Z., Wang, D., Chang, P., Tseng W., Lu, J.G., 2004. ZnO nanowire field-effect transistor oxygen sensing property. Appl. Phys. Lett. 85, 5923-5925.

Fang, F., Futter, J., Markwitz, A., Kennedy, J., 2009. UV and humidity sensing properties of ZnO nanorods prepared by the arc discharge method. Nanotechnology 20(24), 245502.

Fang, Y., Pang, Q., Wen, X., Wang, J., Yang, S., 2006. Synthesis of ultrathin ZnO nanofibers aligned on a zinc substrate. Small 2, 612-615.

Farmakis, F.V., Speliotis, T., Alexandrou, K.P., Tsamis, C., Kompitsas, M., Fasaki, I., Jedrasik, P., Petersson, G., Nilsson, B., 2008. Field-effect transistors with thin ZnO as active layer for gas sensor applications. Microelectron. Eng. 85, 1035-1038.

Fei, P., Yeh, P., Zhou, J., Xu, S., Gao, Y., Song, J., Gu, Y., Huang, Y., Wang, Z.L., 2009. Piezoelectric potential gated field-effect transistor based on a free-standing ZnO wire. Nano Lett. 9, 3435-3439.

Gao, P.X., Ding, Y., Mai, W., Hughes, W.L., Lao, C., Wang, Z.L., 2005. Conversion of zinc oxide nanobelts into superlattice-structured nanohelices. Science 309, 1700-1704.

Gao, Z., Zhou, J., Gu, Y., Fei, P., Hao, Y., Bao, G., Wang, Z.L., 2009. Effects of piezoelectric potential on the transport characteristics of metal-ZnO nanowire-metal field effect transistor. J Appl. Phys. 105, 113707.

Gruber, D., Kraus, F., Müller, J., 2003. A novel gas sensor design based on $CH_4/H_2/H_2O$ plasma etched ZnO thin films. Sens. Actuators B: Chem. 92, 81-89.

Guo, M.Y., Ng, A.M.C., Liu, F., Djurišić, A.B., Chan, W.K., 2011. Photocatalytic activity of metal oxides- the role of holes and OH radicals. Appl. Catal. B 107, 150-157.

Hagen, J.A., Kim, S.N., Bayraktaroglu, B., Leedy, K., Chávez, J.L., Kelley-Loughnane, N., Naik, R.R., Stone, M.O., 2011. Biofunctionalized zinc oxide field effect transistors for selective sensing of riboflavin with current modulation. Sensors 11(7), 6645-6655.

Hariharan, A., 2006. Photocatalytic degradation of organic contaminants in water by ZnO nanoparticles: revisted. Appl. Catal. A 304, 55-61.

Hrapovic, S., Liu, Y., Male, K.B., Luong, J.H.T., 2004. Electrochemical biosensing platforms using platinum nanoparticles and carbon nanotubes. Anal. Chem. 76, 1083-1088.

Hsu, Y.F., Xi, Y.Y., Tam, K.H., Djurišić, A.B., Luo, J., Ling, C.C., Cheung, C.K., Ng, A.M.C., Chan, W.K., Deng, X., Beling, C.D., Fung, S., Cheah, K.W., Fong, P.W.K., Surya, C.C., 2008. Undoped p-type ZnO nanorods synthesized by a hydrothermal method. Adv. Funct. Mater. 18, 1020-1030.

Huang, M.H., Mao, S., Feick, H., Yan, H., Wu, Y., Kind, H., Weber, E., Russo, R., Yang, P., 2001a. Room-temperature ultraviolet nanowire nanolasers. Science 292, 1897-1899.

Huang, M.H., Wu, Y., Feick, H., Tran, N., Weber, E., Yang, P., 2001b. Magnetic force microscopy images of a nanometer-sized, purely organic high-spin polyradical. Adv. Mater. 13, 113-116.

Hughes, W.L., Wang, Z.L., 2004. Formation of piezoelectric single-crystal nanorings and nanobows. J. Am. Chem. Soc. 126, 6703-6709.

Hwang, J.O., Lee, D.H., Kim, J.Y., Han, T.H., Kim, B.H., Park, M., No, K., Kim, S.O., 2011. Vertical ZnO nanowires/grapheme hybrids for transparent and flexible field emission. J. Mater. Chem. 21, 3432-3437.

Ivnitski, D., Abdel-Hamid, I., Atanasov, P., Wilkins, E., 1999. Biosensors for detection of pathogenic bacteria. Biosens. Bioelectron. 14(7), 599-624.

Kenanakis, G., Katsarakis, N., 2010. Light-induced photocatalytic degradation of stearic acid by c-axis oriented ZnO nanowires. Appl. Catal. A: Gen. 378(2), 227-233.

Khoang, N.D., Hong, H.S., Trung, D.D., Duy, N.V., Hoa, N.D., Thinh, D.D., Hieu, N.V., 2013. On-chip growth of wafer-scale planar-type ZnO nanorod sensors for effective detection of CO gas. Sensors Actuat. B: Chem. 181, 529-536.

Kim, J.S., Park, W.I., Lee, C.H., Yi, G.C., 2006. ZnO nanorod biosensor for highly sensitive detection of specific protein binding. J. Korean Phys. Soc. 49(4), 1635-1639.

Kong, X.Y., Wang, Z.L., 2003. Spontaneous polarization-induced nanohelixes, nanosprings, and nanorings of piezoelectric nanobelts. Nano Lett. 3, 1625-1631.

Kumar, S.A., Chen, S., 2008. Nanostructured znic oxide particles in chemically modified electrodes for biosensor applications. Anal. Lett. 41(2), 141-158.

Kwon, S., Hong, W., Jo, G., Maeng, J., Kim, T., Song, S., Lee, T., 2008. Piezoelectric effect on the electronic transport characteristics of ZnO nanowire field-effect transistors on bent flexible substrates. Adv. Mater. 20, 4557-4562.

Lao, J.Y., Huang, J.Y., Wang, D.Z., Ren, Z.F., 2003. ZnO nanobridges and nanonails. Nano. Lett. 3, 235-238.

Law, M., Greene, L.E., Johnson, J.C., Saykally, R., Yang, P., 2005. Nanowire dye-sensitized solar cells. Nat. Mat. 4, 455-459.

Leung, Y.H., Tam, K.H., Djurišić, A.B., Xie, M.H., Chan, W.K., Lu, D., Ge, W.K., 2005. ZnO nanoshells: Synthesis, structure, and optical properties. J. Cryst. Growth 283, 134-140.

Li, Q.H., Liang, Y.X., Wan, Q., Wang, T.H., 2004. Oxygen sensing characteristics of individual ZnO nanowire transistors Appl. Phys. Lett. 85, 6389-6391.

Li, Z., Yang, R., Yu, M., Bai, F., Li, C., Wang, Z.L., 2008. Cellular level biocompatibility and biosafety of ZnO nanowires. J. Phys. Chem. C 112, 20114-20117.

Lin, Y., Lu, F., Tu, Y., Ren, Z., 2004. Glucose biosensors based on carbon nanotube nanoelectrode ensembles. Nano Lett. 4, 191-195.

Liu, A., 2008. Towards development of chemosensors and biosensors with metal-oxide-based nanowire or nanotubes. Biosensors and Bioelectronics 24(2), 167-177.

Lu, C., Chang, S., Chang, S., Hsueh, T., Hsu, C., Chiou, Y., Chen, I., 2009. A lateral ZnO nanowire UV photodetector prepared on a ZnO:Ga/glass template. Semicond. Sci. Technol. 24(7), 075005.

Lupan, O., Chai, G., Chow, L., 2007. Fabrication of ZnO nanorod-based hydrogen gas nanosensor. Microelectron. J. 38(12), 1211-1216.

Ma, C., Zhou, Z., Wei, H., Yang, Z., Wang, Z., Zhang, Y., 2011. Rapid large-scale preparation of ZnO nanowires for photocatalytic application. Nanoscale Res. Lett. 6, 536-540.

Martins, R., Fortunato, E., Nunes, P., Ferreira, I., Marques, A., Bender, M., Katsarakis, N., Cimalla, V., Kiriakidis, G., 2004. Zinc oxide as an ozone sensor. J. Appl. Phys. 96, 1398-1408.

Newton, M.C., Warburton, P.A., 2007. ZnO tetrapod nanocrystals. Mater. Today 10(5), 50-54.

Nuzzo, R.G., Dubois, L.H., Allara, D.L., 1990. Fundamental studies of microscopic wetting on organic surfaces, formation and structural characterization of a self-consistent series of polyfunctional organic monolayers. J. Am. Chem. Soc. 112(2), 558-569.

Özgür, Ü, Alivov, Y.I., Liu, C., Teke, A., Reshchikov, M.A., Doğan, S., Avrutin,V., Cho, S.J., Morkoç, H., 2005. A comprehensive review of ZnO materials and devices. J. Appl. Phys. 98, 041301.

Ozgur, U., Hofstetter, D., Morkoc, H., 2010. ZnO devices and applications: A review of current status and future prospects. Proceedings of the IEEE 98(7), 1255-1268.

Pan, Z.W., Dai, Z.R., Wang, Z.L., 2001. Nanobelts of semiconducting oxides. Science 291, 1947-1949.

Pang, W., Yan, L., Zhang, H., Yu, H., Kim, E.S., Tang, W.C., 2006. Femtogram mass sensing platform based on lateral extensional mode piezoelectric resonator. Appl. Phys. Lett. 88, 243503-243505.

Park, S., Wang, Y., Yeow, J.T.W., Yin, Y., Chen, L., 2010. Humidity sensing characteristics of ZnO nanowires aligned by dielectrophoresis method. Proceedings of 10th IEEE

International Conference on Nanotechnology Joint Symposium with Nano Korea, August, 17-20.

Ramirez-Vick, J.E., 2012. Nanostructured ZnO for electrochemical biosensors. J. Biosens. Bioelectron. 3(2), e109. doi:10.4172/2155-6210.1000e109.

Rocha-Gaso, M., March-Iborra, C., Montoya-Baides, A., Arnau-Vives, A., 2009. Surface generated acoustic wave biosensors for the detection of pathogens: A review. Sensors 9, 5740-5769.

Rodriquez, J.A., Jirsak, T., Dvorak, J., Sambasivan, S., Fischer, D., 2000. Reaction of NO_2 with Zn and ZnO: Photoemission, XANES, and density functional studies on the formation of NO_3. J. Phys. Chem. B 104, 319-328.

Rout, C.S., Govindaraj, A., Rao, C.N.R., 2006. High-sensitivity hydrocarbon sensors based on tungsten oxide nanowires. J. Mater. Chem. 16, 3936-3941.

Sadaf, J.R., Israr, M.Q., Kishwar, S., Nur, O., Willander, M., 2011. Forward- and reverse-biased electroluminescence behaviour of chemically fabricated ZnO nanotubes/GaN interface. Semicond. Sci. Technol. 26(7), 075003.

Sberveglieri, G., Groppelli, S., Nelli, P., Tintinelli, A., Giunta, G., 1995. A novel method for the preparation of NH_3 sensors based on ZnO-In thin films. Sens. Actuat. B: Chem. 25(1-3), 588-590.

Snure, M., Ashutosh, T., 2007. Synthesis, characterization, and green luminescence in ZnO nanocages. J. Nanosci. Nanotechnol. 7, 481-485.

Strehlitz, B., Nikolaus, N., Stoltenburg, R., 2008. Protein detection with aptamer biosensors. Sensors 8, 4296–4307.

Sugunan, A., Guduru, V.K., Uheida, A., Toprak, M.S., Muhammed, M., 2010. Radially oriented ZnO nanowires on flexible poly-L-lactate nanofibers for continuous-flow photocatalytic water purification. J. Am. Ceram. Soc. 93, 3740-3744.

Sun, Y., Fuge, G.M., Fox, N.A., Riley, D.J., Ashfold, M.N.R., 2005. Synthesis of aligned arrays of ultrathin ZnO nanotubes on a Si wafer coated with a thin ZnO film. Adv. Mater. 17, 2477-2481.

Talbi, A., Sarry, F., Elhakiki, M., Le Brizoual, L., Elmazria, O., Nicolay, P., Alnot, P., 2006. ZnO/quartz structure potentiality for surface acoustic wave pressure sensor. Sensor. Actuat. A: Phys. 128(1), 78-83.

Tian, Z.R., Voigt, J.A., Liu, J., Mekenzie, B., Mcdermott, M.J., 2002. Biomimetric arrays of oriented helical ZnO nanorods and columns. J. Am. Chem. Soc. 124, 12954-12955.

Wang, J.X., Sun, X.W., Huang, H., Lee, Y.C., Tan, O.K., Yu, M.B., Lo, G.Q., Kwong, D.L., 2007a. A two-step hydrothermally grown ZnO microtube array for CO gas sensing. Appl. Phys. A 88, 611-615.

Wang, W.Z., Zeng, B.Q., Yang, J., Poudel, B., Huang, J.Y., Naughton, M.J., Ren, Z.F., 2006a. Aligned ultralong ZnO nanobelts and their enhanced field emission. Adv. Mater. 18, 3275-3278.

Wang, X., Chen, Y., Gibney, K.A., Erramilli, S., Mohanty, P., 2008. Silicon-based nanochannel glucose sensor. Appl. Phys. Lett. 92, 013903-013905.

Wang, X., Song, J., Liu, J., Wang, Z.L., 2007b. Direct-current nanogenerators driven by ultrasonic waves. Science 316, 102-105.

Wang, X., Zhou, J., Song, J., Liu, J., Xu, N., Wang, Z.L., 2006b. Piezoelectric field effect transistor and nanoforce sensor based on a single ZnO nanowire. Nano. Lett. 6, 2768-2772.

Wang, Z.L., 2004. Zinc oxide nanostructures: growth, properties and applications. J. Phys.: Condens. Mater. 16, R829.

Wang, Z.L., 2007. Oxide nanobelts and nanowires-growth, properties and applications. J. Nanosci. Nanotechnol. 8, 27-55.

Wang, Z.L., 2008. Towards self-powered nanosystems: from nanogenerators to nanopiezotronics. Adv. Funct. Mater. 18, 3553-3567.

Wang, Z.L., Kong, X.Y., Ding, Y., Gao, P., Hughes, W.L., Yang, R., Zhang, Y., 2004. Semiconducting and piezoelectric oxide nanostructures induced by polar surfaces. Adv. Funct. Mater. 14, 943-956.

Wang, Z.L., Song, J.H., 2006. Piezoelectric nanogenerators based on zinc oxide nanowire arrays. Science 312, 242-246.

Wen, X., Fang, Y., Pang, Q., Yang, C., Wang, J., Ge, W., Wong, K.S., Yang, S., 2005. ZnO nanobelts arrays grown directly from and on zinc substrates: synthesis, characterization, and applications. J. Phys. Chem. B 109, 15303-15308.

Willander, M., Nur, O., Zhao, Q.X., Yang, L.L., Lorenz, M., Cao, B.Q., Pérez, J.Z., Czekalla, C., Zimmermann, G., Grundmann, M., Baklin, A., Behrends, A., Al-Suleiman, M., El-Shaer, A., Che Mofor, A., Postels, B., Waag, A., Boukos, N., Travlos, A., Kwack, H.S., Guinard, J., Le Si Dang, D., 2009. Zinc oxide nanorod based photonic devices: recent progress in growth, light emitting diodes and lasers. Nanotechnology 20(33), 332001-332040.

Xu, S., Qin, Y., Xu, C., Wei, Y., Yang, R., Wang, Z.L., 2010. Self-powered nanowire devices. Nat. Nanotechnol. 5(5), 366-373.

Yang, Y., Sun, X.W., Tay, B.K., You, G.F., Tan, S.T., Teo, K.L., 2008. A p-n homojunction ZnO nanorod light-emitting diode formed by As ion implantation. Appl. Phys. Lett. 93, 253107-253109.

Yu, R., Pan, C., Wang, Z.L., 2013. High performance of ZnO nanowire protein sensors enhanced by the piezotronic effect. Energy Environ. Sci. 6, 494-499.

Zhang, X., Wang, H., Bourgeois, L., Pan, R., Zhao, D., Webley, P.A., 2008. Direct electrodepostion of gold nanotube arrays for sensing applications. J. Mater. Chem. 18, 463-467.

Zhang, Y., Liu, Y., Wu, L., Li, H., Han, L., Wang, B., Xie, E., 2009. Effect of annealing atmosphere on the photoluminescence of ZnO nanospheres. Appl. Surf. Sci. 255(9), 4801-4805.

Zhang, Y., Ram, M.K., Stefanakos, E.K., Goswami, D.Y., 2012. Synthesis, characterization, and applications of ZnO nanowires. Journal of Nanomaterials 2012, 1-22.

Zhang, Y., Yu, K., Jiang, D., Zhu, Z., Geng, H., Luo, L., 2005. Zinc oxide nanorod and nanowire for humidity sensor. Appl. Surf. Sci. 242(1-2), 212-217.

Zhao, C., Huang, C., Zhu, R., Xu, J., Chen, L., Yu, D., 2011. 2D planar field emission devices based on individual ZnO nanowires. Solid State Commun. 151(22), 1650-1653.

Zhao, Q.X., Klason, P., Willander, M., 2007. Growth of ZnO nanostructures by vapour-liquid-solid method. Appl. Phys. A: Mater. Sci. Process. 88(1), 27-30.

Table 1. XRD pattern of synthesized ZnO nanowires on a substrate covered with a 20 nm Au (111) film layer and a ZnO seed layer film deposited the sol-gel spin coating technique.

2-theta	Hkl	Intensity (%)
31.74	100	0.025
34.43	002	100
36.25	101	0.113
47.54	102	0.036
62.87	103	0.113
72.61	004	3.153
76.95	202	0.006
81.4	104	0.046
89.63	203	0.006
104.17	105	0.056
125.23	006	0.007

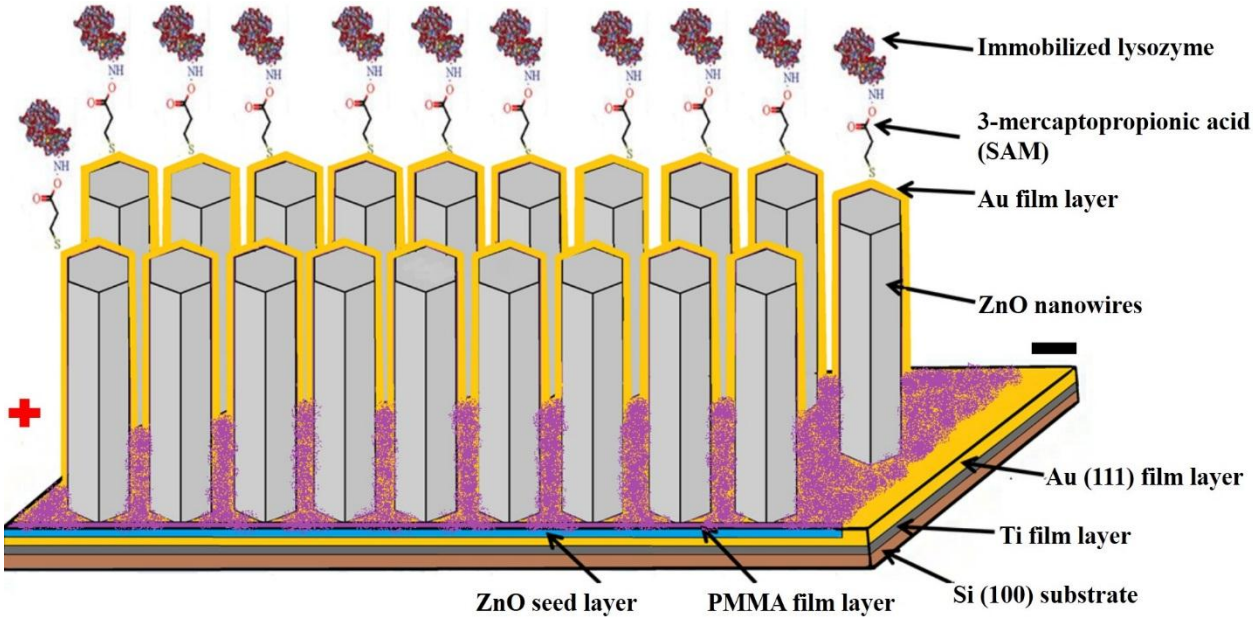

Fig. 1. Schematic diagram of the constructed nanoforce ZnO nanowire-array biosensor.

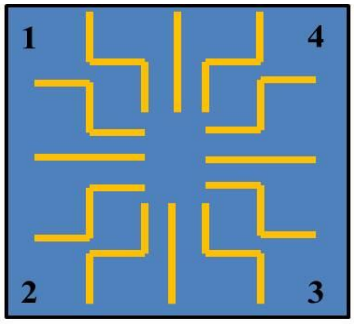

Fig. 2. Schematic diagram of the switch board onto which the ZnO nanowire-array biosensor is mounted.

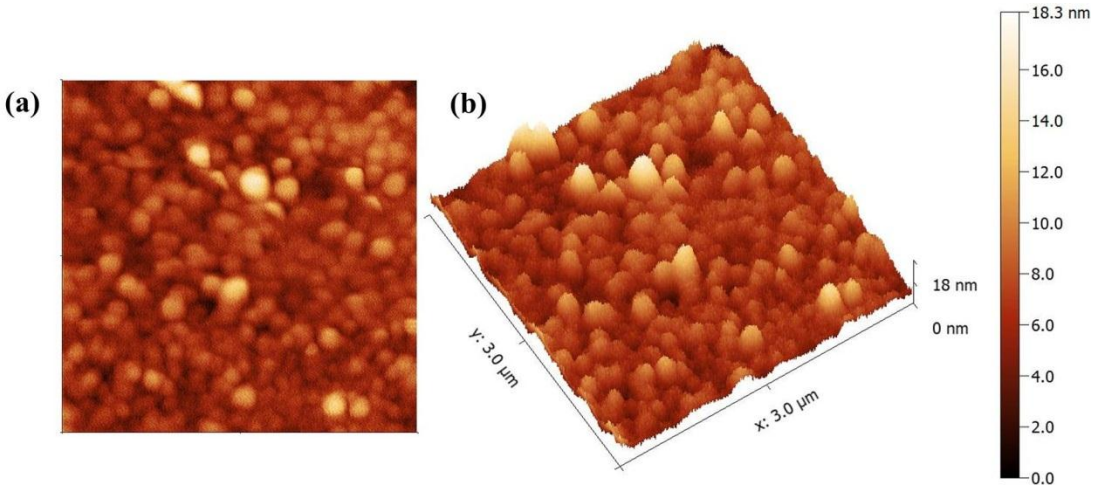

Fig. 3. Two dimensional (**a**) and three dimensional (**b**) AFM images of the surface topology of the ZnO seed layer film deposited by the sol-gel spin coating technique.

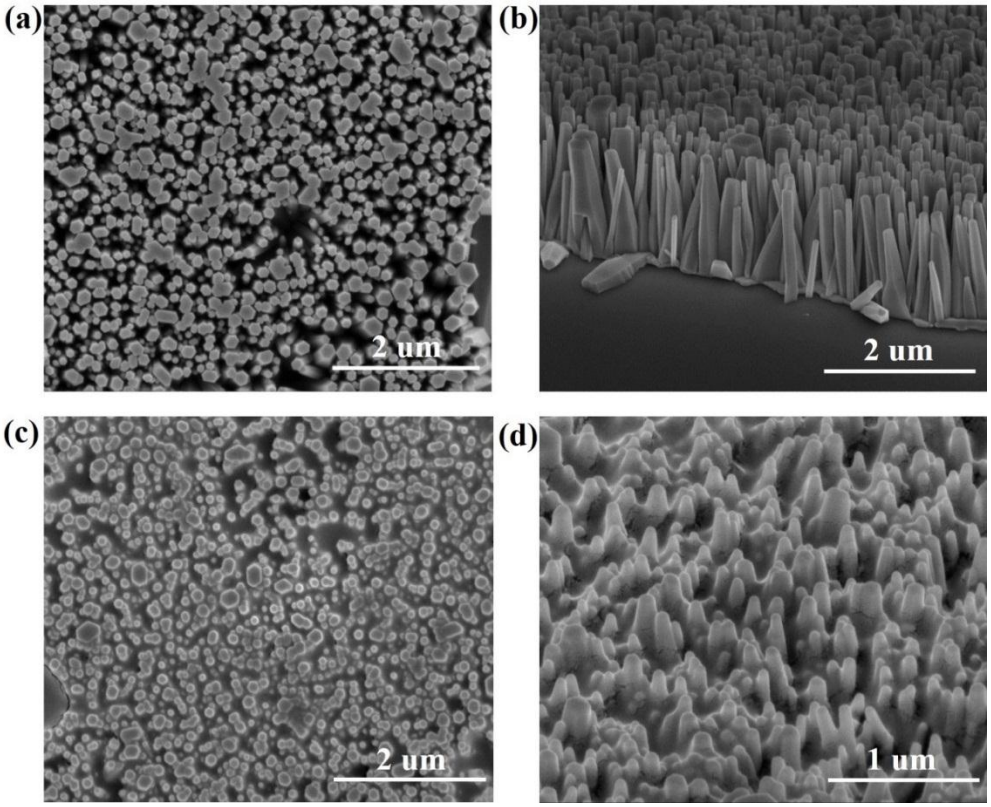

Fig. 4. High magnification top FEI-SEM images of vertically aligned ZnO nanowires grown using the hydrothermal growth method on substrates containing a 20 nm Au (111) film with a ZnO seed layer film deposited by the sol-gel spin coating technique (**a**). Low magnification tilted (50°) FEI-SEM image of ZnO nanowires (**b**). High magnification top FEI-SEM image of ZnO nanowires spin coated with PMMA and deposited with a 10 nm Au film layer (**c**). High magnification tilted (50°) FEI-SEM image of ZnO nanowires spin coated with PMMA and covered with a 10 nm Au film layer (**d**).

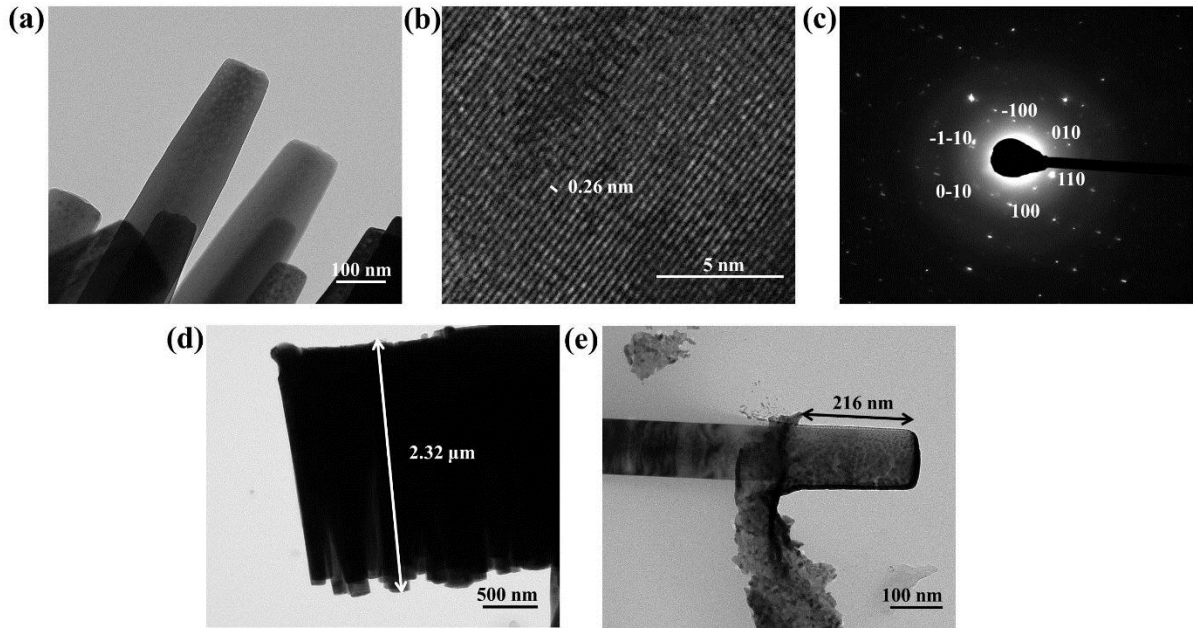

Fig. 5. TEM images of ZnO nanowires synthesized on substrates covered with a 20 nm Au (111) film which is covered by a ZnO seed layer film deposited the sol-gel spin coating technique (**a**) with its corresponding HRTEM image (**b**) and SAED pattern (**c**) are shown. The average length of the synthesized ZnO nanowires (**d**) and ZnO nanowires spin coated with PMMA and deposited with a 10 nm Au film layer (**e**) is shown.

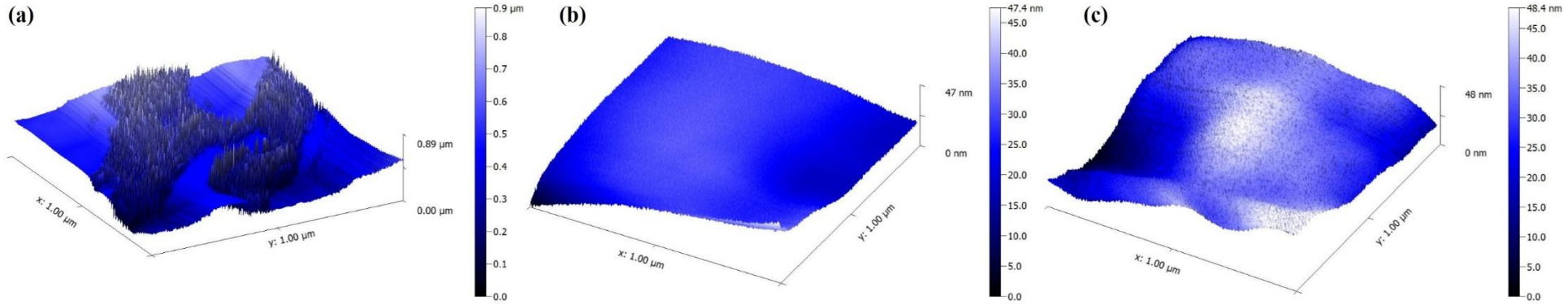

Fig. 6. Three dimensional topographic AFM images of the (**a**) constructed biosensor, (**b**) a smooth surface of the biosensor, (**c**) a smooth surface of the biosensor immobilized with lysozyme.

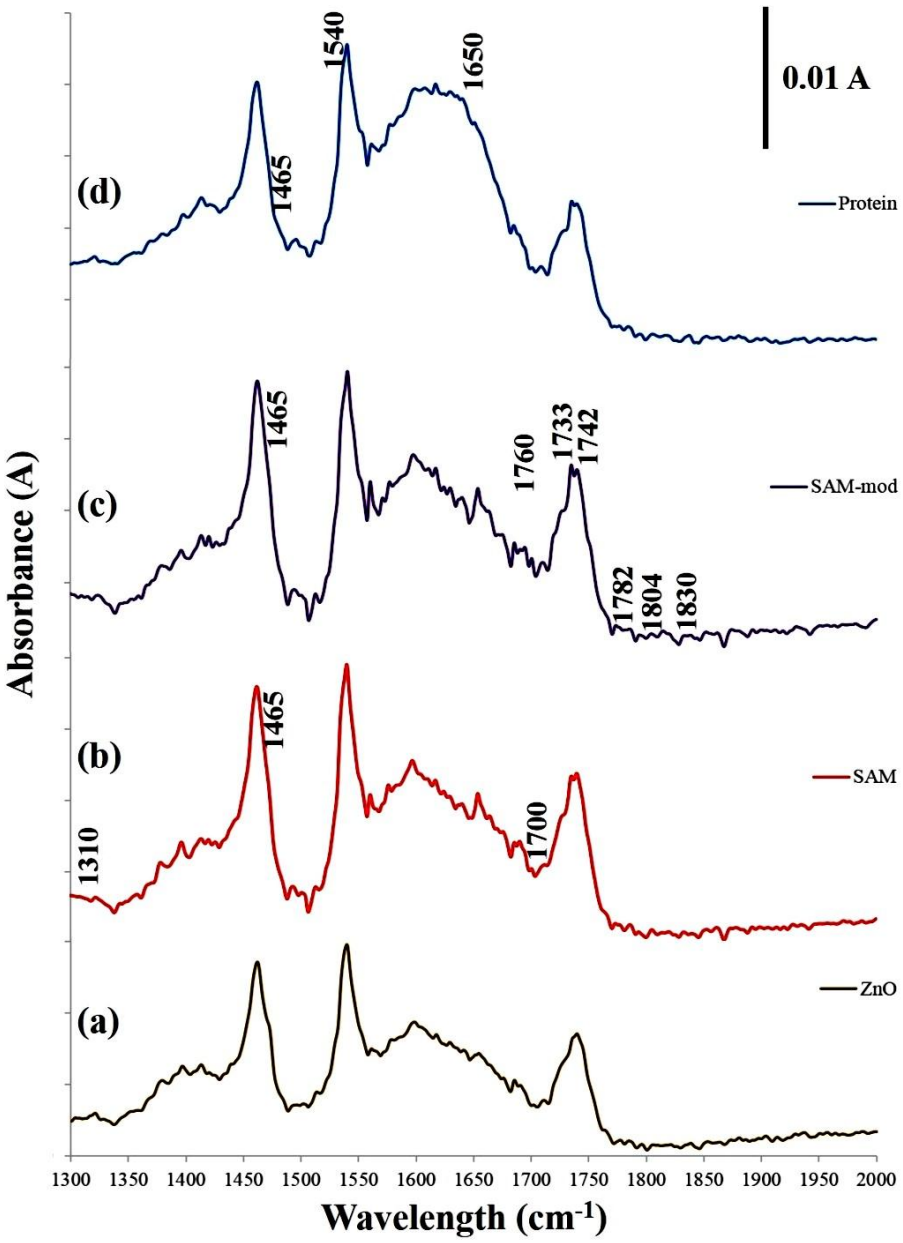

Fig. 7. FTIR spectra of the (**a**) biosensor surface, (**b**) the biosensor surface bound with the 3-mercaptopropionic acid SAM, (**c**) the SAM modified by EDC/NHS esterification and the biosensor surface (**d**) covalently immobilized with lysozyme is shown.

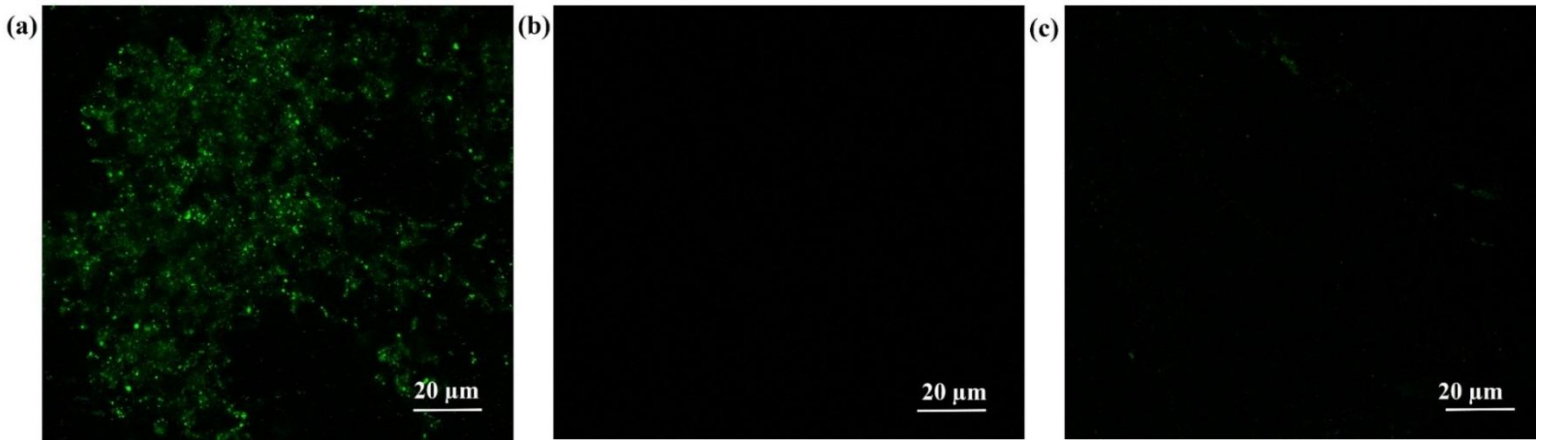

Fig. 8. Fluorescence images of the biosensor surface (**a**) immobilized with lysozyme, (**b**) non-specific binding of the secondary antibody conjugate to the biosensor surface, and (**c**) non-specific binding of lysozyme to the biosensor surface is shown.

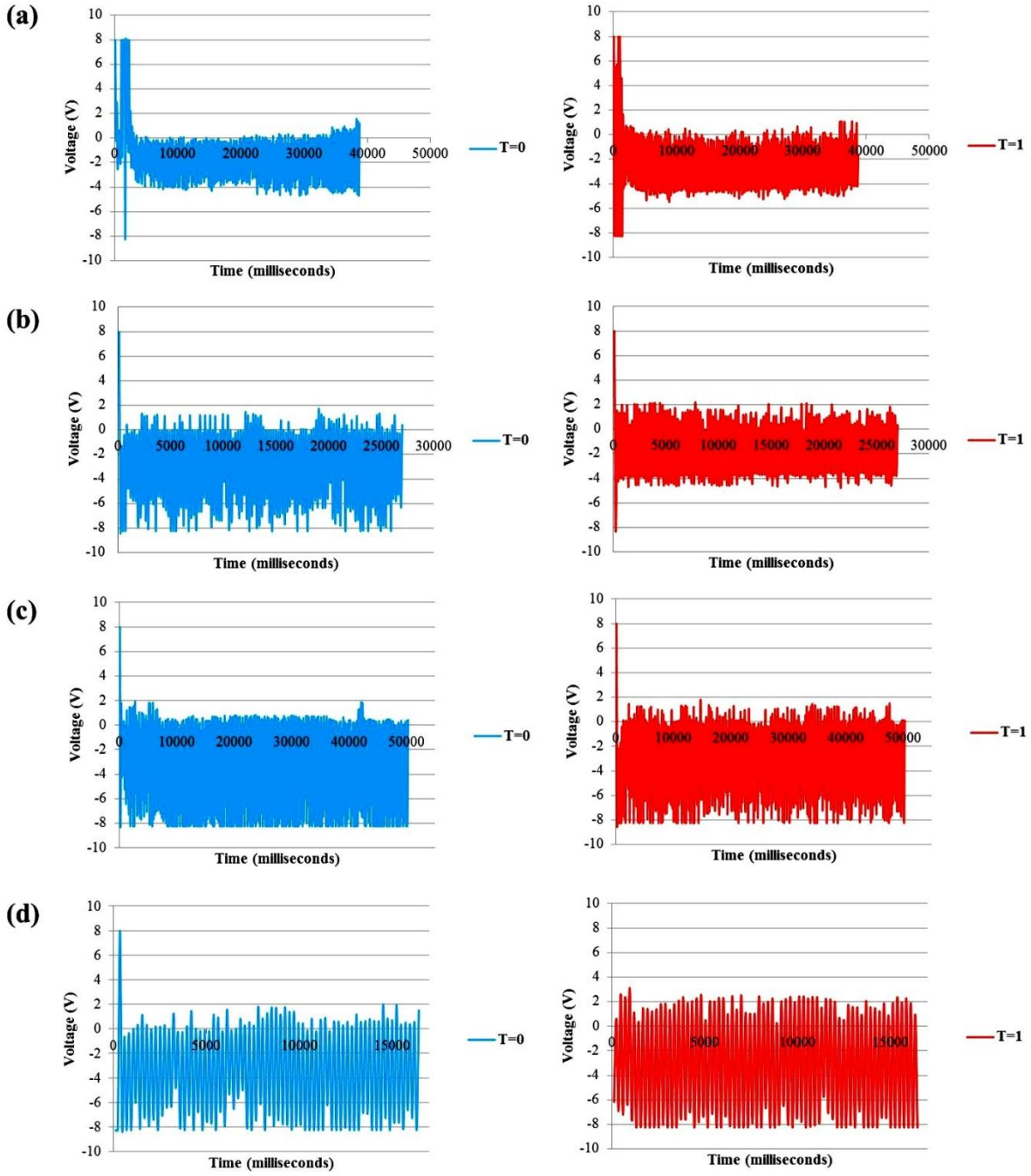

Fig. 9. Measured output voltage of the biosensors prior to analysis and after incubation with primary lysozyme antibodies at a concentration of (**a**) 10 ng/ml, (**b**) 50 ng/ml, (**c**) 500 ng/ml and (**d**) 1 µg/ml for 1 hour. The Schottky barrier rectifies the generated piezoelectric potential resulting in the observed voltage peaks.

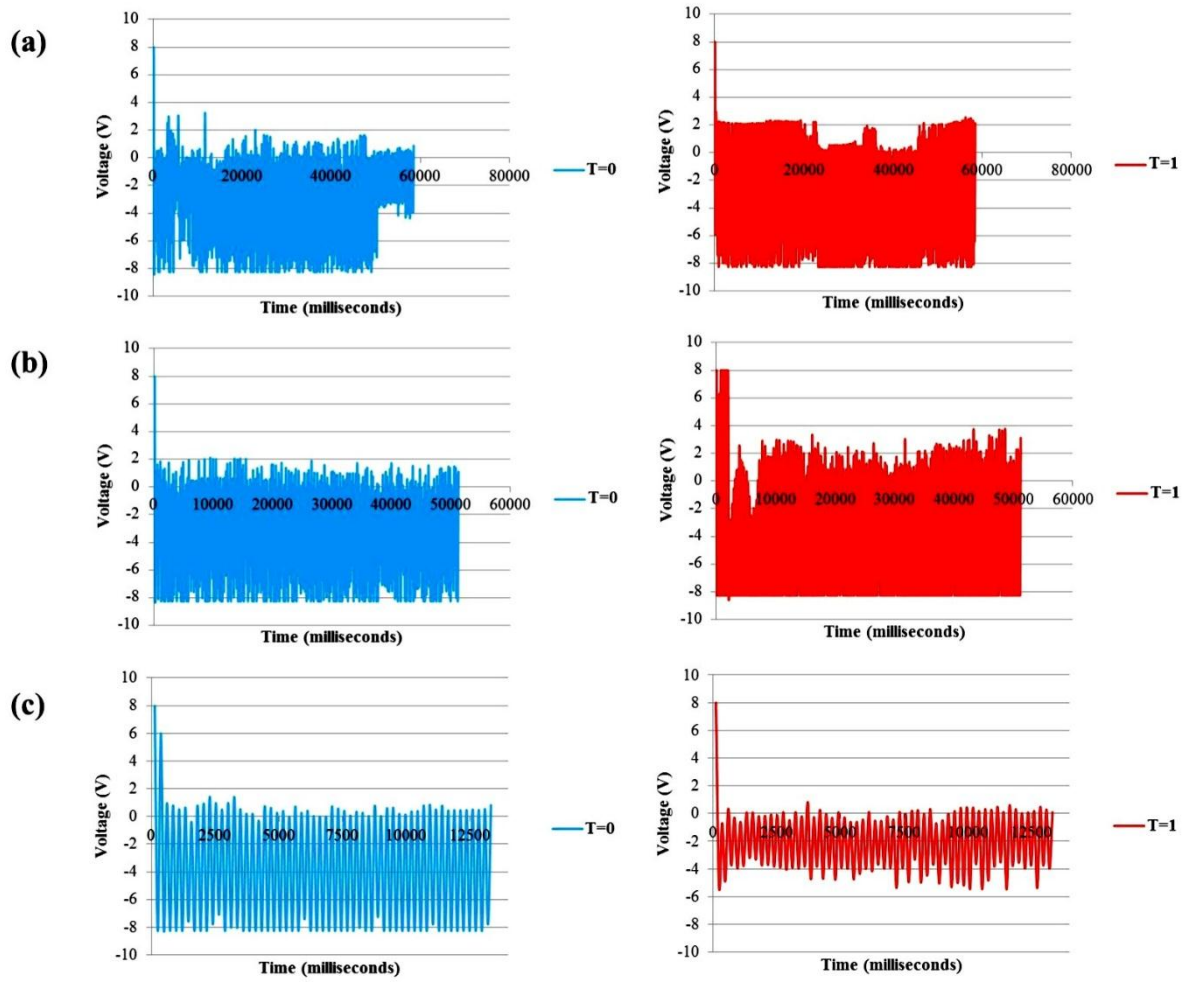

Fig. 10. Measured output voltage of the biosensors prior to analysis and after incubation with primary lysozyme antibodies at a concentration of (**a**) 10 µg/ml and (**b**) 20 µg/ml for 1 hour. A negative control (**c**) was included in which only PBS solution was incubated for 1 hour. The Schottky barrier rectifies the generated piezoelectric potential resulting in the observed voltage peaks.

CHAPTER 6

General Discussion and Conclusions

General Discussion and Conclusions

The aim of this study was to assess whether ZnO nanowires could be used as piezoelectric transducers for the detection of immunoglobulins. Growth factors which influences the synthesis of ZnO nanowires by the hydrothermal growth approach was assessed to determine the optimum growth conditions that would produce c-axis oriented ZnO nanowires with similar dimensions. The study also assessed the immobilization of lysozyme to Au film layers. The immobilization of lysozyme to different SAMs were assessed to determine which absorbate results in the highest surface loading of lysozyme, while retaining biological activity. The developed nanoforce ZnO nanowire-array biosensor was tested *in vitro* to determine whether biomolecular recognition could be sensed. In theory, binding of antibodies to the biosensor surface would induce disturbances in the ZnO nanowire structure, resulting in the generation of a piezoelectric potential, due to the Schottky barrier the piezoelectric potential is rectified and voltage is generated.

Numerous factors need to be taken into account when synthesizing ZnO nanowires by the hydrothermal growth approach. The dimensions i.e. the mean diameter, position and density of the synthesized ZnO nanowires would influence the performance of the developed biosensor (Liu et al., 2008; Song and Lim, 2007). Seed layer deposition techniques sol-gel spin coating and RF cylindrical magnetron sputtering were compared, to determine which deposition technique results in the most c-axis oriented ZnO nanowires with similar dimensions. For both deposition techniques, the increase in the ZnO seed layer deposition resulted in an increase in the mean ZnO seed grain diameter and subsequently an increase in the mean diameter of the synthesized ZnO nanowires. This is consistent with previous reports (Zhang et al., 2006). Increasing the ZnO seed layer thickness by the RF cylindrical magnetron sputtering technique resulted in the improvement of the c-axis alignment of the synthesized ZnO nanowires. When the sol-gel spin coating technique was used, an increase in the ZnO seed layer thickness resulted in the worsening of the c-axis alignment of the synthesized ZnO nanowires.

Worsening of the c-axis alignment may be attributed to the increase in the surface roughness as the ZnO seed layer thickness increases by the sol-gel spin coating technique. The rougher the surface, the more nucleation sites are created for ZnO nanowire growth resulting in the increase in disorientation (Wang et al., 2012). The RF cylindrical magnetron

sputtering technique resulted in the synthesis of ZnO nanowires with similar dimensions, as compared to the sol-gel spin coating technique which resulted in a more diverse diameters. The effects of Au film layer thickness and crystal orientation on the synthesis of ZnO nanowires were also assessed. Increasing the Au film layer thickness resulted in the decrease in the mean diameter and a worsening of the c-axis alignment of the synthesized ZnO nanowires. Polycrystalline Au film layers resulted in the increase in the mean ZnO nanowire diameter, as opposed to single-crystalline Au (111) film layers. Crystal orientation of the Au film layer had no effect on the c-axis alignment of the synthesized ZnO nanowires.

Immobilization of biomolecules to the sensor surfaces is the most demanding aspect during the development of biosensors (Fransconi et al., 2010; Gooding and Hibbert, 1999; Rusmini et al., 2007; Wong et al., 2009). Lysozyme was immobilized to Au (111) film layers using self-assembled monolayers (SAMs). Different SAMs were created and chemically modified to become reactive toward primary amino groups of lysozyme, to determine which SAM results in the highest level of protein immobilization while retaining biological activity. SAM formation successfully occurred, as well as the modification of monolayers by EDC/NHS esterification or DSP addition. Results showed that the SAM immobilization approach resulted in high levels of lysozyme immobilization. Self-assembled monolayer 3-mercaptopropionic acid resulted in the most immobilized lysozyme, whereas combined SAM 11-mercaptoundecanoic acid/1-nonanethiol resulted in the worst immobilization.

Short chain alkanethiol 3-mercaptopropanioc acid immobilized more lysozyme as appose to long chain alkanethiol 11-mercaptoundecanioc acid. Longer chain alkanethiol SAMs are more susceptible to oxidation than shorter chains, resulting in their desorption from the Au surface (Ron and Rubinstein, 1998; Wang et al., 2003). The use of combined SAMs controlled the degree of protein immobilization which corresponds with previously reported results (Gooding and Hibbert, 1999; Gooding et al., 2003; Wasserman et al., 1989). The immobilized lysozyme activity was assessed by a BacLight^{TM} bacterial viability assay and was found to be inconclusive. *Micrococcus luteus* cells died faster on clean Au film layers as opposed to the immobilized lysozyme layers. It seem as the immobilized lysozyme molecules protects the bacterial cells from direct contact with the antibacterial Au film layer surface. However, a decrease in the viability of the bacterial cells were observed which might be due to the degradation of the cell walls by lysozyme, the exposure to the antibacterial Au film layer surface or quenching of the fluorescent dye.

A nanoforce ZnO nanowire-array biosensor was developed for the detection and quantification of immunoglobulins. Lysozyme antigens and antibodies were used as a model. The performance of the biosensor was assessed by incubating different lysozyme antibody concentrations on the surface. Voltage generated prior to analysis was measured to determine the background signal. After 1 h incubation with different antibody concentrations the resulting voltage was measured. ZnO nanowires show promising results as transducers for biosensors for the detection of biomolecular recognition events.

Increased antibody concentrations resulted in increased voltage production. The increased binding of antibodies to the biosensor surface results in increased disturbances in the ZnO nanowire structures, and subsequently increased piezoelectric potential. The piezoelectric potential is rectified by a Schottky barrier which results in the generation of voltage. It should be expressed that numerous hurdles need to be overcome in order for ZnO biosensors to become more sensitive and reproducible. Site specific growth in which the dimensions are the identical or similar should be sought as variations would influence the sensitivity and reproducibility of the developed biosensor. Additionally, spin coating of PMMA to fill spaces between the ZnO nanowires creates areas that are fully covered with no ZnO nanowire protrusions which would influence the performance and reproducibility of the biosensor. ZnO nanowire possesses promising characteristics to be developed as nanoforce biosensors for the detection of biomolecular interactions. However, numerous hurdles need to be overcome to construct a ZnO nanowire biosensor which is reproducible.

References

Fransconi, M., Mazzei, F., Ferri, T., 2010. Protein immobilization at gold-thiol surfaces and potential for biosensing. Anal. Bioanal. Chem. 398(4), 1545-1564.

Gooding, J.J., Hibbert, D.B., 1999. The application of alkanethiol self-assembled monolayers to enzyme electrodes. Trends in Analytical Chem. 18(8), 525-533.

Gooding, J.J., Mearns, F., Yang, W., Liu, J., 2003. Electroanalysis 15(2), 81-96.

Liu, J., Fei, P., Zhou, J., Tummala, R., Wang, Z.L., 2008. Toward high output-power nanogenerator. Appl. Phys. Lett. 92(17), 173105.

Ron, H., Rubinstein, I., 1998. Self-assembled monolayers on oxidized metals, alkylthiol and dialkyl disulphide assembly on gold under electrochemical conditions. J. Am. Chem. Soc. 120(51), 13444-13452.

Rusmini, F., Zhong, Z., Feijen, J., 2007. Protein immobilization strategies for protein biochips. Biomacromoleucles 8(6), 1775-1789.

Song, J., Lim, S., 2007. Effect of seed layer on the growth of ZnO nanorods. J. Phys. Chem. C 111(2), 596-600.

Wang, L., Tsan, D., Stoeber, B., Walus, K., 2012. Substrate-free fabrication of self-supporting ZnO nanowire arrays. Adv. Mater. 24(29), 3999-4004.

Wang, M.C., Liao, J.D., Weng, C.C., Klauser, R., Shaporenko, A., Grunze, M., Zharnikov, M., 2003. Modification of aliphatic monomolecular films by free radical dominant plasma: the effect of the alkyl chain length and the substrate. Langmuir 19(23), 9774-9780.

Wasserman, S.R., Tao, Y.T., Whitesides, G.M., 1989. Structure and reactivity of alkylsiloxane monolayers formed by reaction of alkyltrichlorosilanes on silicon substrates. Langmuir 5(4), 1074-1087.

Wong, L.S., Khan, F., Mickfield, J., 2009. Selective covalent protein immobilization: strategies and applications. Chem. Rev. 109(9), 4025-4053.

Zhang, C., Li, X., Zhang, X., Yu, W., Zhao, J., 2006. Seed-layer induced growth of highly-quality oriented ZnO films by a sol-gel process. J. Cryst. Growth 290(1), 67-72.